12-1991

A Comparative Study of Numerical Versus Analytical Waverider Solutions

Gregory O. Stecklein

AFIT/GAE/ENY/91D-26

A COMPARATIVE STUDY OF NUMERICAL VERSUS ANALYTICAL WAVERIDER SOLUTIONS

THESIS

Gregory O. Stecklein

Captain, USAF

AFIT/GAE/ENY/91D-26

Approved for public release; distribution unlimited

AFIT/GAE/ENY/91D-26

A COMPARATIVE STUDY OF NUMERICAL VERSUS ANALYTICAL WAVERIDER SOLUTIONS

THESIS

Presented to the Faculty of the School of Engineering

of the Air Force Institute of Technology

Air University

In Partial Fulfillment of the

Requirements for the Degree of

Master of Science in Aeronautical Engineering

Gregory O. Stecklein, B.A.E.

Captain, USAF

December 1991

Acknowledgements

Through the trails and tribulations of completing this research thesis, I find myself indebted to several people for their assistance and support. I can not imagine being able to complete this research thesis without the total dedication and support of Dr. Datta Gaitonde. His efforts in developing and restructuring the solution code utilized in my research were outstanding. He was never too busy to take the time to teach me the basics of the code and help me to format and understand my results. He gave his time freely, usually at my convenience. To my advisor, LCol Gerald Hasen, I wish to express my gratitude for his understanding and patience during times when I had reached my capacity for understanding. He has the rare ability to take the most technical of topics and express them in a layman's terms. A note of thanks goes to Captain Kenneth Moran, who was a constant thorn in my side during these investigations. His in depth queries concerning the direction and application of my work was invaluable in focusing my efforts towards a concise goal.

On a personal level, I wish to dedicate this thesis to my son, Destin. He was my one true source of unquestioning, and unfailing love. He is truly a gift from God.

Gregory O. Stecklein

Table of Contents

Page

List of Figures

Figure Page

List of Tables

Table | Page

List of Symbols

c_D	Coefficient of drag
c_{Dw}	Coefficient of wave drag, Pressure Drag
c_f	Skin friction coefficient
c_L	Lift coefficient
c_p	Coefficient of pressure
c_{pmax}	Maximum surface pressure coefficient
D	Total Drag; Wave drag and friction
D_w	Wave drag, drag due to pressure
E_t	Total energy
fps	foot, pounds, seconds unit of measure
ℓ	Length of the generating cone
ℓ_w	Length of the waverider
$\ell\delta$	Waverider length scaling parameter
m	Slope of a line
M_∞	Freestream Mach number
P_b	Waverider base pressure, assumed = 0
P_∞	Freestream pressure at a standard altitude
q_∞	Freestream dynamic pressure: $1/2\gamma P_\infty M_\infty^2$
r	Radial distance from the generating cone axis to an arbitrary point in the flow
R_0	Non-dimensional offset distance from the axis of the generating cone to the waverider plane of symmetry
$R_\infty(\phi)$	Polar mapping of the waverider freestream surface
$R_{cb}(\phi)$	Polar mapping of the waverider compression

	surface
$r_s(\phi)$	Polar mapping function descibing the leading edge of the waverider
S_p	Waverider planform area
S_w	Waverider wetted-surface area
V_r	Radial velocity component
X	Non-dimensional length: $x/(\delta\ell)$
Y	Non-dimensional length: $y/(\delta\ell)$
Z	Non-dimensional length: $r_s(\phi)/\ell$
z_w	Streamwise location of the nose of the waverider: $z - (\ell - \ell_w)$

Greek

α	Angle of attack
β	Half angle from conical axis to shock wave
γ	Ratio of specific heats; assumed constant γ=1.4
δ	Half angle of generating cone
θ	Half angle measured from the axis of the generating cone to area of interest in the flow field: $\delta \le \theta \le \beta$
ρ_∞	Freestream density for a standard altitude
σ	HSDT similarity parameter measuring radial distance of the shock cone in the baseplane
σ_0	Non-dimensional radius of shock cone at the waverider nose: = R_0
σ_z	Non-dimensional radius of shock cone at an arbitrary waverider cross section
ϕ	Dihedral angle of range $-\phi_\ell \le \phi \le \phi_\ell$
ϕ_ℓ	Dihedral angle of waverider in baseplane
ϕ_z	Dihedral angle at an arbitrary cross section

ξ	Computational streamwise axis
η	Computational normal axis
ζ	Computational spanwise axis

AFIT/GAE/ENY/91D-26

ABSTRACT

The WL/FIMM explicit, Roe flux-splitting Euler algorithm is applied to the inviscid hypersonic flow over a parabolic-top waverider configuration optimized for Mach 10 at zero degrees angle of attack. An on-design grid refinement study is conducted to determine the asymptotic nature of the optimized flight parameter L/D. A parametric study of off-design conditions is conducted to determine flow perturbation effects on HSDT waverider theory. A validation of the Euler code is conducted through a comparison of the numerical data to analytical results derived by Rasmussen.

The grid refinement study shows little effect on the inviscid calculation of the optimized parameter L/D. Good agreement with HSDT waverider theory was attained for the on and off-design evaluations. Approximations involved in the numerical modeling of the waverider design produce large losses of lift as compared to the analytical results. Matching of the analytical results was possible only through a theoretical modeling process.

A COMPARATIVE STUDY OF NUMERICAL VERSUS ANALYTICAL WAVERIDER SOLUTIONS

I. Introduction

1.1 Background

A renewal of interest in hypersonic flight, brought about by projects such as hypersonic transports, missiles, the National Aerospace Plane, and planetary reentry vehicles, has focused much attention on the stringent requirements of aerodynamic technology and design. Dimensional and volume distributions of a hypersonic vehicle create strong shock waves in the flow which must be incorporated into the design process. Modern philosophies of design utilize blended wing, body and propulsive system configurations to best utilize the strong shock interactions of the flow field. The waverider is a useful design concept for maximizing the effects of the strong shock waves encountered in hypersonic flow (19:1-2; 4:1-2).

Waveriders are lifting bodies generated from known flow fields. A waverider is a supersonic or hypersonic blended wing-body vehicle designed to have an attached shock wave along its entire leading edge, while maintaining freestream conditions along its entire upper surface, as illustrated in Figure 1.1. The effect of this attached shock wave is a vehicle which appears to be riding its own shock wave and hence the name waverider. The high pressure behind the shock wave is entirely captured by the compression surface of the waverider. The upper surface design maintains freestream or slightly expanded pressure conditions. This marked difference in pressure on the upper and lower surface produces a favorable gradient resulting in a net compressive lift, while the freestream upper surface tends to minimize total drag. The effect is a vehicle designed to maximize the lift to drag ratio, L/D, for highly compressive hypersonic flight conditions (3:1-2).

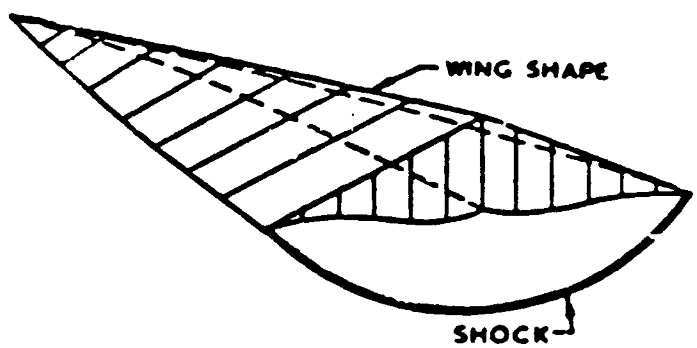

Figure 1.1. Waverider With Attached Shock Wave (3:12)

The concept of the waverider was first introduced by Nonweiler and Hilton in 1958 (18:3). This concept was later published by Nonweiler in 1959 in Aerodynamic Problems of Manned Space Vehicles. The initial designs were generated from a two-dimensional, supersonic flow field impinging on a wedge. The three-dimensional waverider body produced was coined the "caret wing" due to its caret-shaped base plane design. The caret wing was designed to ride the planar shock produced by the generating two-dimensional flow as illustrated in Figure 1.2 (18:3-4).

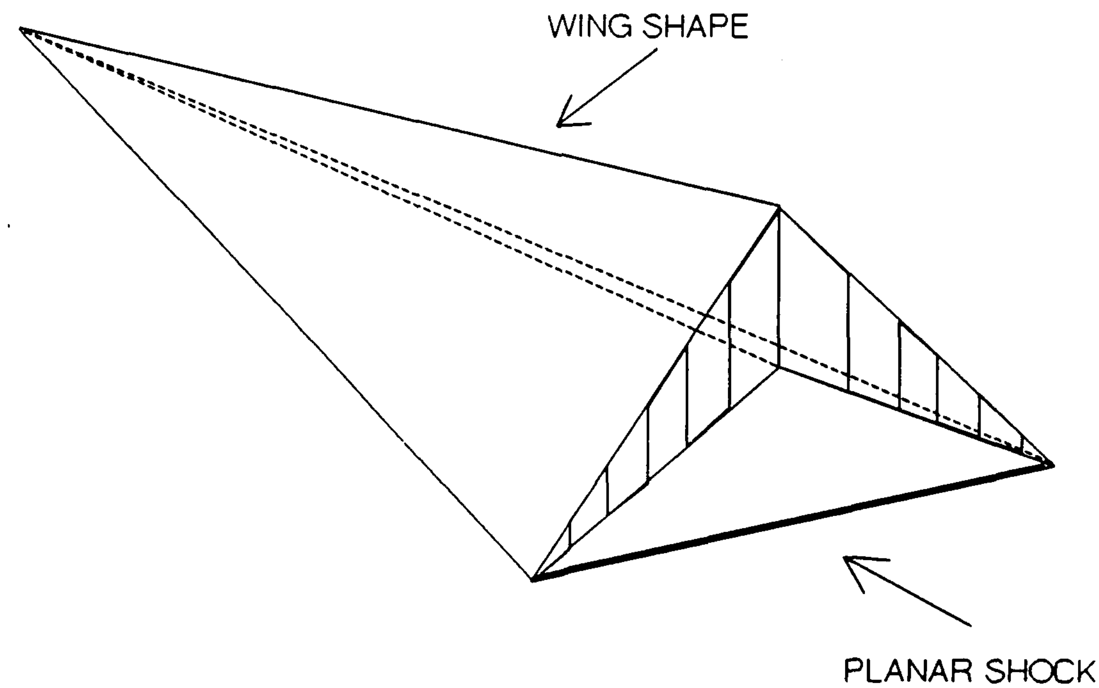

Figure 1.2. Caret Wing Planar Waverider

Nonweiler's initial work on the waverider concept was followed by others like Townend (24), who compiled an extensive survey of waverider research, and Roe (22), who developed a tutorial methodology for the basic two-dimensional design. These works aided in the encapsulation of waverider development and design knowledge to date and extended the initial concept of the waverider. Rasmussen (21:2-3) expanded the idea to axisymmetric flows of conical shape in which he utilized Hypersonic Small Disturbance Theory in the analysis. His early works, performed in the 1980s, sought to optimize waverider design for a specific Mach number and cone angle for inviscid flow conditions. Küchemann (15:341) developed an accurate approximation, based on actual flight vehicle experience, for the L/D of a slender supersonic vehicle given by:

$$L/D = 3\frac{(M_\infty+3)}{M_\infty} \tag{1.1}$$

This approximation agreed well with the analytical results of inviscidly optimized waverider designs. Viscous flow optimization was subsequently applied to axisymmetrically derived waveriders by Bowcutt and Anderson (7:8-9), who produced shapes that would optimize L/D, or a variety of other parameters, through the use of an integral boundary layer technique with a simplex optimization method . This optimization process and analysis developed waveriders with higher predicted L/D ratios than the previous inviscid designs for a given Mach number. The L/D values for the viscously-optimized designs could be approximated by:

$$L/D = 6\,\frac{(M_\infty+2)}{M_\infty} \tag{1.2}$$

1.2 Objectives

The determination of inviscid effects of hypersonic flow on a waverider by computational means has not been fully explored for the bulk of waverider designs to date. Waveriders designed from axisymmetric conical flow have been optimized for a given flight regime for both inviscid and viscous flow fields. The waverider shapes of Rasmussen were developed and analyzed analytically to determine on design flight parameters and specifically L/D ratios (19:1). Experimental investigations to date have been limited to waverider shapes with planar freestream surfaces and more complex shapes at supersonic Mach numbers in the range 3 - 4. The planar model of the freestream surface does not effectively coincide with freestream axisymmetric flow. The sharp leading edges and nose region also do not account for the severe aerothermodynamic heating the waverider would encounter at high flight velocities (13:1-2; 20:3-4).

There are two primary reasons for conducting this research thesis. The first is to contribute to the database of computational solutions for hypersonic waverider designs, validated against an analytical formulation of an identical configuration at its design condition. This will allow a direct comparison to the inversely designed analytic flow field and the numerically computed flow field as illustrated in Figure 1.3.

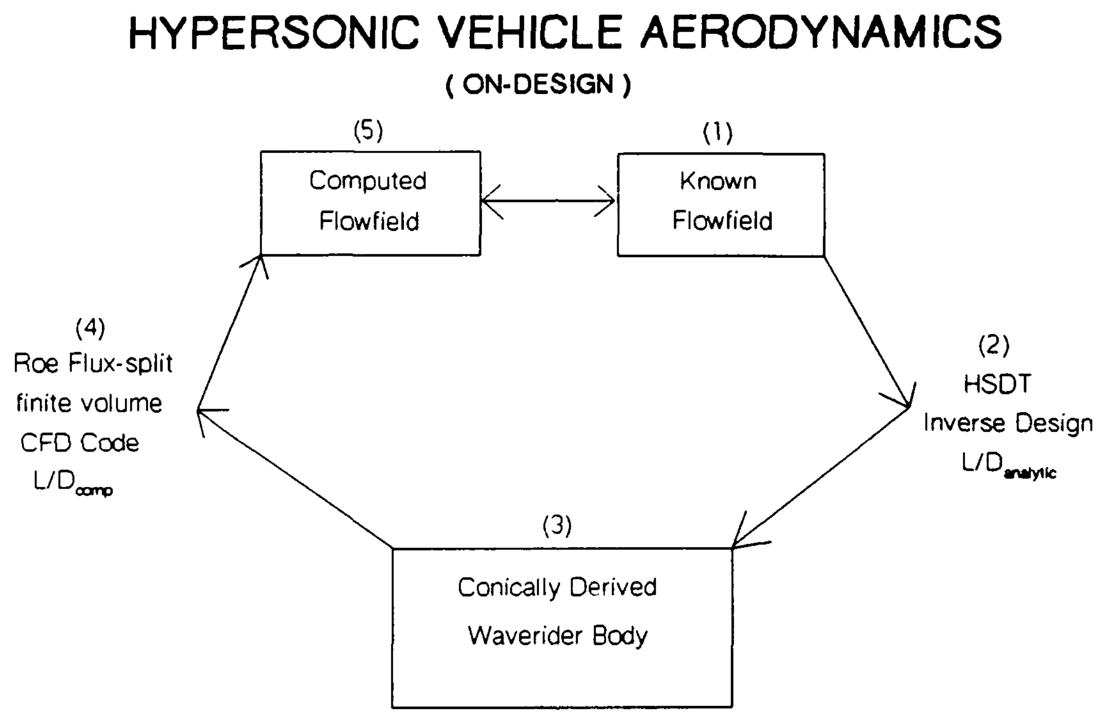

Figure 1.3. Analytical/Numerical Design Cycle

The second purpose is to provide validation results for the Wright Laboratory's high speed, explicit, finite-volume Euler code for a configuration considered favorable for the forebody design of such current research projects as the

National Aerospace Plane (NASP), X-30 Hypersonic research aircraft.

The specific objectives of this research thesis are as follows:

(1) Develop a computer code to formulate the general body coordinates of an inviscidly designed hypersonic waverider.

(2) Generate a three-dimensional grid suitable for capturing the expected on-design flow-field characteristic of a high speed waverider body.

(3) Apply the inviscid version of the Wright Laboratory's Three-dimensional explicit, Roe Flux-splitting algorithm developed by Gaitonde (10) to formulate the lift to drag ratio of the waverider in hypersonic flight. A key validation aspect is the code's capability to effectively handle high hypersonic Mach numbers.

(4) Compare the computational solutions for L/D to the analytical results developed by Rasmussen (19:24) and Martin (9:102) for an identically designed configuration.

(5) Perturb on-design flight conditions to determine basic off-design flight characteristics.

The following key assumptions are incorporated into this computational investigation of waverider performance. The baseline test configuration is a tangent parabolic-top waverider designed from a generating cone of a half angle (δ)

of 5.5° and a freestream Mach number of 10. The base pressure of the waverider is assumed equal to freestream pressure. This assumption is valid for the current research since the waverider configuration being computed is only considered as a possible forebody of a complete vehicle and hence any outflow results would skew the data from the analytical approximations. Also, the magnitude of the pressure through the shock on the lower region is so great as compared to the freestream that the difference between the base pressure and freestream is negligible for the inviscid case. Small angle approximations based on hypersonic small disturbance theory (HSDT) are incorporated into the design process due to the slenderness of the test design vehicle and the high speed hypersonic flow characteristics. From HSDT, angle approximations are of the form

$$\cos\theta = 1 \qquad \sin\theta = \theta$$

A non-dimensionalization of waverider cross sections is performed with the scaling factor ($\ell\delta$), where ℓ is the length and δ is the half angle of the generating cone. Streamwise non-dimensionalization is applied through referencing the streamwise location on the waverider with its total length of the form z_w/ℓ_w.

1.3 Methodology

The vehicle design methodology was derived and presented in detail by Rasmussen (19). The derivation of the vehicle configuration is based on the axisymmetric supersonic flow past a circular cone. To begin, a standard Cartesian (X,Y,Z) reference frame is utilized to develop the flow field. The Z-axis is the axis of symmetry of the basic cone and is pointed in the direction of the freestream flow. The X-axis is directed downward and with Z defines the symmetry plane of the waverider configuration. The Y-axis is pointed in the spanwise direction. Spherical coordinates (r,θ,ϕ) are imposed on the conical reference body as illustrated in Figure 1.4. Theta (θ) is the angle measured from the Z-axis and Phi (ϕ) is the azimuthal angle measured from the X-axis in the X-Y plane (19:2-3). The HSDT approximation of small angles is utilized to estimate the radial position (r) from $r = Z\cos\theta$ to $r = Z$. The basic cone flow geometry is designated by the cone semiangle (δ), the shock angle (β), and the ratio of shock angle to cone angle ($\beta/\delta = \sigma$).

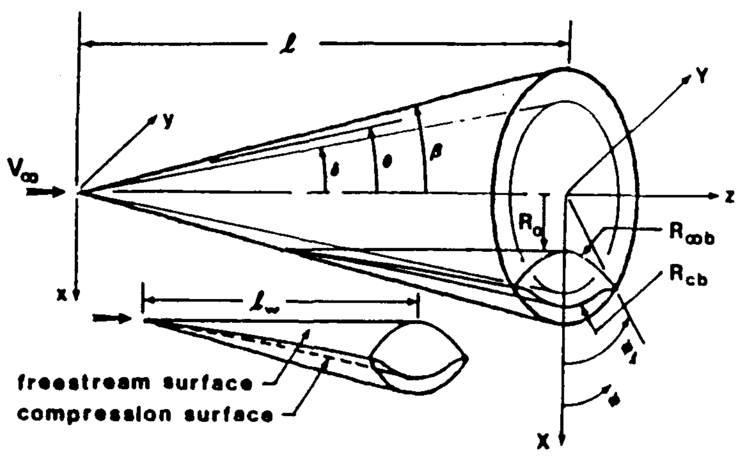

Figure 1.4. Waverider in Generating Flow Field

Once the reference flow is defined, a non-conical body can be derived which will contain the a portion of the conical shock wave on the lower surface and hence will maintain a portion of the conically developed flow field. The upper surface of the waverider is designed to maintain freestream conditions and hence optimize the body's profile drag (16:6).

A basic outline of the development scheme for the optimized waverider follows with a graphical representation shown in Figure 1.5.

(1) The trailing edge of the freestream surface is defined from a four-term, sixth-order polynomial. The polynomial is simplified considerably for the choice of a tangent parabolic top waverider; this design choice retains only the first two terms of the equation (16:12).

(2) For conical flow, The Taylor-Maccoll equation, derived in detail by Anderson (3:296-301) must be solved numerically to determine all aspects of the generating flow field. The Taylor-Maccoll equation is an ordinary differential equation with only one dependent variable V_r. This equation represents the continuity and momentum equations for an axisymmetric conical flow and is given as:

$$\frac{\gamma-1}{2}\left[1-V_r^2-\left(\frac{dV_r}{d\theta}\right)^2\right]\left[2V_r+\frac{dV_r}{d\theta}\cot\theta+\frac{d^2V_r}{d\theta^2}\right]$$

$$-\frac{dV_r}{d\theta}\left[V_r\frac{dV_r}{d\theta}+\frac{dV_r}{d\theta}\frac{d^2V_r}{d\theta^2}\right]=0 \qquad (1.3)$$

(3) Once the flow field is defined, streamlines are then traced back from the waverider's freestream trailing edge until they intersect the conical shock wave. This procedure defines the entire upper surface and leading edge of the waverider body.

(4) From the defined leading edge which intersects the conical shock wave, streamlines are traced rearward until they intersect the waverider's baseplane. These streamlines, generated by the conical flow, define the compression surface of the waverider.

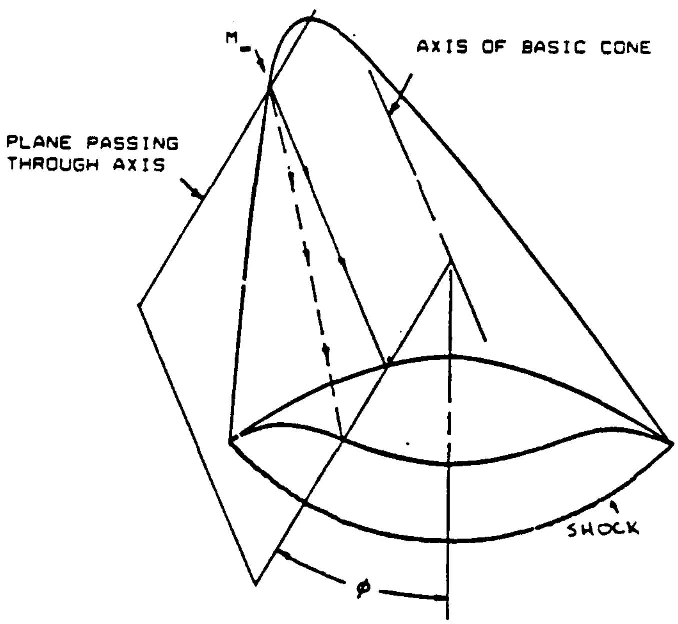

Figure 1.5. Waverider Design Methodology (16:7)

Once the waverider body is fully defined, a body fitted O-grid is generated to define the domain of interest for the numerical solution algorithm. The computational grid system was designed to scale as the cross section of the waverider so that the conical shock wave is resolved at approximately the same grid location for each planar cross section. Scaling the grid also saves computational resources which would otherwise be wasted on computing conditions remaining at freestream levels. An elliptic outer boundary was chosen since its resolution from the body to the outer domain most effectively modeled the expected shape of the generated shock wave. The Roe flux-splitting algorithm (11) is applied due to its shock capturing, and capability to model the flow field modeling high Mach numbers. The Roe flux-splitting algorithm is also desirable for hypersonic evaluations due to its accuracy in handling the unsteady behavior of the flow (14:8-9). The numerical solutions of the velocity components (u,v,w), Mach number and pressure coefficient, as well as lift, wave drag and L/D for the waverider are sought to confirm its optimized configuration for inviscid flow. The numerically generated performance data is compared to analytical data tabulated by Rasmussen (19) to provide a validation of the Euler solution algorithm.

II. WAVERIDER SURFACE AND GRID FORMULATION

The computationally generated hypersonic flow over an inviscidly optimized tangent parabolic-top waverider design, derived in works by Martin (16) and Rasmussen (19), is analyzed and compared to the analytic results. The use of inviscid optimization was chosen for the ease of design, availability of design methodology and cataloged analytical solutions. For a detailed examination of the hypersonic small disturbance derivation of the waverider surface parameters, the reader should consult Martin's Hypersonic Waverider Configurations For Trans-Atmospheric Vehicles, AFIT/CI Master's Thesis (16).

2.1 General Waverider Design

From Rasmussen (21:3), the freestream and compression surfaces are described in spherical coordinates, utilizing small angle approximations as:

$$r\theta = r_s(\phi)\,\beta \qquad (freestream) \tag{2.1}$$

$$r(\theta^2 - \delta^2)^{\frac{1}{2}} = r_s(\phi)\,(\beta^2 - \delta^2)^{\frac{1}{2}} \qquad (compression) \tag{2.2}$$

where $r = r_s(\phi)$ is the line of intersection of the freestream and compression surface leading edge, and ϕ is the included angle measured from the line of symmetry to the intersection of the freestream and compression surfaces at the conical shock, as illustrated in Figure 1.5. From HSDT, the cone half angle δ is related to the shock angle β through the similarity relationship

$$\sigma = \frac{\beta}{\delta} = \left(\frac{\gamma+1}{2} + \frac{1}{M_\infty^2 \delta^2}\right)^{\frac{1}{2}} \qquad (2.3)$$

Using the small angle assumption, σ can be shown to also be the non-dimensional radius of the conical shock wave in the waverider baseplane.

The freestream surface of the waverider is defined from a four term sixth order polynomial of the form:

$$X = R_0 + AY^2 + BY^4 + CY^6 \qquad (2.4)$$

where R_0, A, B, and C are constant coefficients that determine the surface curvature of the designated waverider configuration (21:3). This polynomial must satisfy the following two conditions:

$$\begin{aligned} &1)\quad X = R_0 && (Y=0) \\ &2)\quad X = \sigma\cos\phi_\ell && (Y = \sigma\sin\phi_\ell) \end{aligned} \qquad (2.5)$$

The second condition is necessary to ensure that the freestream and compression surfaces intersect at the shock where $\theta = \beta$. The angle ϕ_ℓ is the maximum included angle in the baseplane.

2.1.? Baseplane Design

By converting to spherical coordinates, a function can be defined which relates the trailing edge of the compression surface to the trailing edge of the freestream surface through the use of the sweep angle ϕ and the HSDT similarity parameter σ. The non-dimensional X and Y coordinates are transformed as $X = R_{\infty b}\cos\phi$ and $Y = R_{\infty b}\sin\phi$, where $R_{\infty b}$ defines the freestream trailing edge as illustrated in Figure 1.4. This conversion simplifies the function $r_s(\phi)$ in Equations (2.1) and (2.2) to $r_s(\phi) = \ell R_{\infty b}(\phi)/\sigma$. From this function and Equation (2.2), an equation for the trailing edge of the compression surface is derived as:

$$R_{cb}(\phi)^2 = 1 + \left(\frac{\sigma^2 - 1}{\sigma^2}\right) R_{\infty b}^2(\phi) \qquad (2.6)$$

This transformation reduces the entire baseplane representation as a function of ϕ and the design constant σ. The parabolic-top waverider in this study utilizes only a two-term second-order polynomial, which when simplified from Equation (2.4) and combined with the second condition from Equation (2.5) reduces to:

$$\sigma\cos\phi_1 = R_0 + A\sigma^2\sin^2\phi_1 \qquad (2.7a)$$

$$X_\sigma = R_0 + AY_\sigma^{\,2} \qquad (2.7b)$$

Solving for the one unknown coefficient, A becomes:

$$A = \frac{(X_\sigma - R_0)}{Y_\sigma^{\ 2}} \qquad (2.8)$$

Through the use of Equation (2.8) and the Pythagorean theorem

$$R_{\infty b} = (X_\sigma^{\ 2} + Y_\sigma^{\ 2})^{\frac{1}{2}} \qquad (2.9)$$

An explicit equation for the freestream surface can then be derived as a function of ϕ alone

$$R_{\infty b}(\phi) = \frac{2R_0}{\cos\phi + (\cos^2\phi - 4R_0 A\sin^2\phi)^{\frac{1}{2}}} \qquad (2.10)$$

As a design consideration, $R_{\infty b}(\phi)$ is limited to a range of

$$0 \le \phi \le \phi_\ell \qquad (2.11)$$

This stipulation forces a range of R_0 values of

$$R_0 \ge \frac{\sigma\cos\phi_\ell}{2} \qquad (2.12)$$

For the case of the tangent-parabolic top waverider, R_0 is taken as

$$R_0 = \frac{\sigma\cos\phi_\ell}{2} = \frac{X_\sigma}{2} \qquad (2.13)$$

2.1.2 Body Cross-Section Formulation

The same form of the polynomial exists for any body cross section along the streamwise plane. However, the limiting value of the included sweep angle ϕ is reduced as the outermost value of Y, or the span, is reduced. The shock relationship parameter σ scales such that at the nose, the limiting value of $\phi_0 = 0$ coincides with $\sigma_0 = R_0$ (16:14-15). The shock attachment condition is still enforced for each arbitrary spanwise cross section by:

$$X = \sigma_z \cos\phi_z \qquad Y = \sigma_z \sin\phi_z$$
$$\sigma_z \cos\phi_z = R_0 + A\sigma_z^2 \sin^2\phi_z \tag{2.14}$$

An expression for σ_z can then be obtained, since its known values range from $\sigma_0 = R_0$ to $\sigma_\ell = \sigma$.

$$\sigma_z = R_0 + \frac{z_w}{\ell_w}(\sigma - R_0) \tag{2.15}$$

Where z_w/ℓ_w is the non-dimensional length of the waverider, and σ_z reduces to the design parameter σ in the baseplane as illustrated in Figure 2.1. The waverider length and streamwise scale length are then:

$$\ell_w = \ell - \frac{R_0 \ell}{\sigma}$$
$$z_w = z - \frac{R_0 \ell}{\sigma} = z - (\ell - \ell_w) \tag{2.16}$$

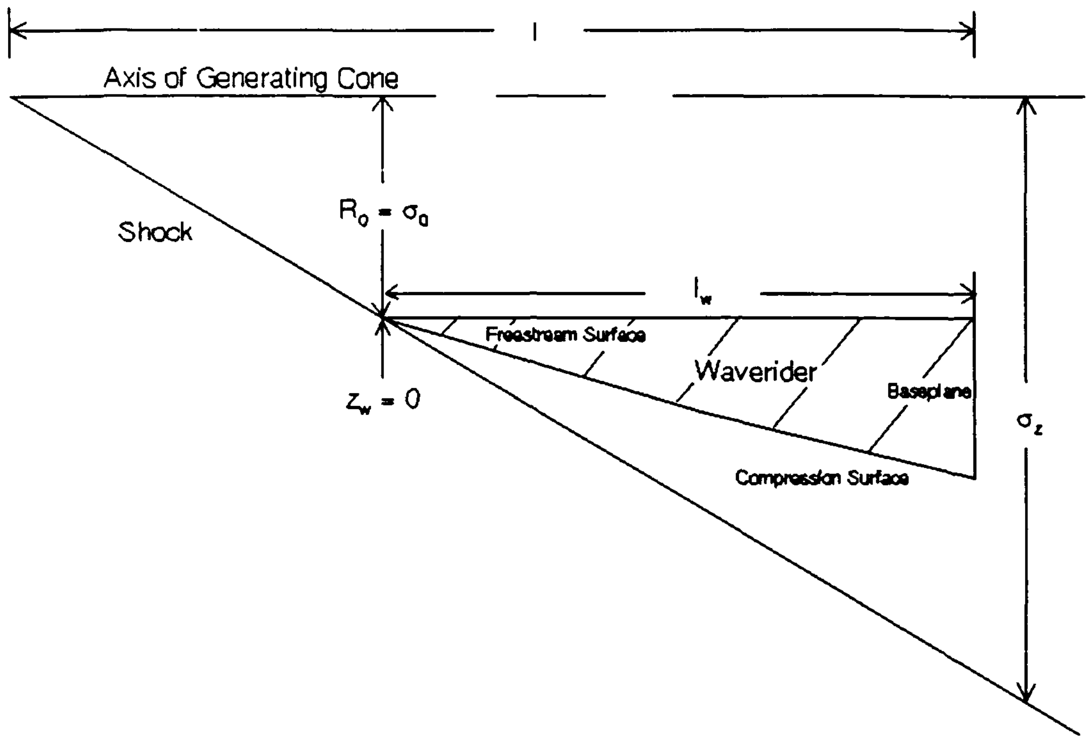

Figure 2.1. Waverider Profile with Attached Shock

The scaling of the freestream surface reduces with the value of ϕ at the leading edge. The compression surface utilizes a dependence on ϕ, but also incorporates the percentage length scale of the waverider from the modified equation (16:17-18):

$$(R_{cb}(\phi)^2)_{arb} = \left(\frac{z_w}{\ell_w}(1-\frac{R_0}{\sigma}) + \frac{R_0}{\sigma}\right)^2 + \left(\frac{\sigma^2-1}{\sigma^2}\right)R_{\infty b}(\phi)^2 \qquad (2.17)$$

At the limit value $z_w/\ell_w = 1$, Equation (2.17) reduces to the baseplane compression surface Equation (2.6). The included angle, ϕ, dependence of the planar cross-sections is illustrated in Figure 2.2.

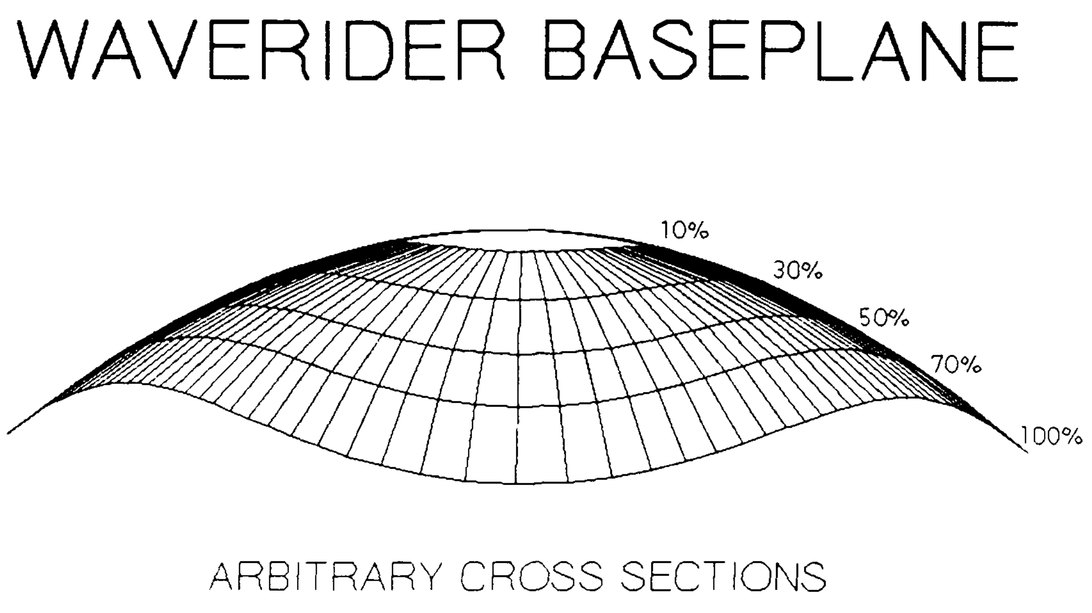

Figure 2.2. Baseplane Cross Section Perspective

2.2 Grid Generation

A major portion of the actual work for this research thesis focused on the determination of a grid type and structure to be implemented on the waverider surface. The practice of three-dimensional grid generation is fairly new. A review of current literature (17), (12) illustrates the idea of the methodology as more of an art than a proven science. The endeavor to determine an optimal grid type and structure for the research at hand has been, and is, a task worthy of an entirely separate research effort. With this in mind, a grid system was sought that would effectively and efficiently capture the expected on design effects of a waverider body in an inviscid flow field.

2.2.1 O-Grid versus H-Grid

Two major grid options presented themselves at the onset of this research effort. The two grid types, illustrated in Figure 2.3, were the O-grid, which wraps completely around the body surface and the H-grid, which is characterized by a branch cut placed in an area of high curvature or cusp. The O-grid was selected for this study.

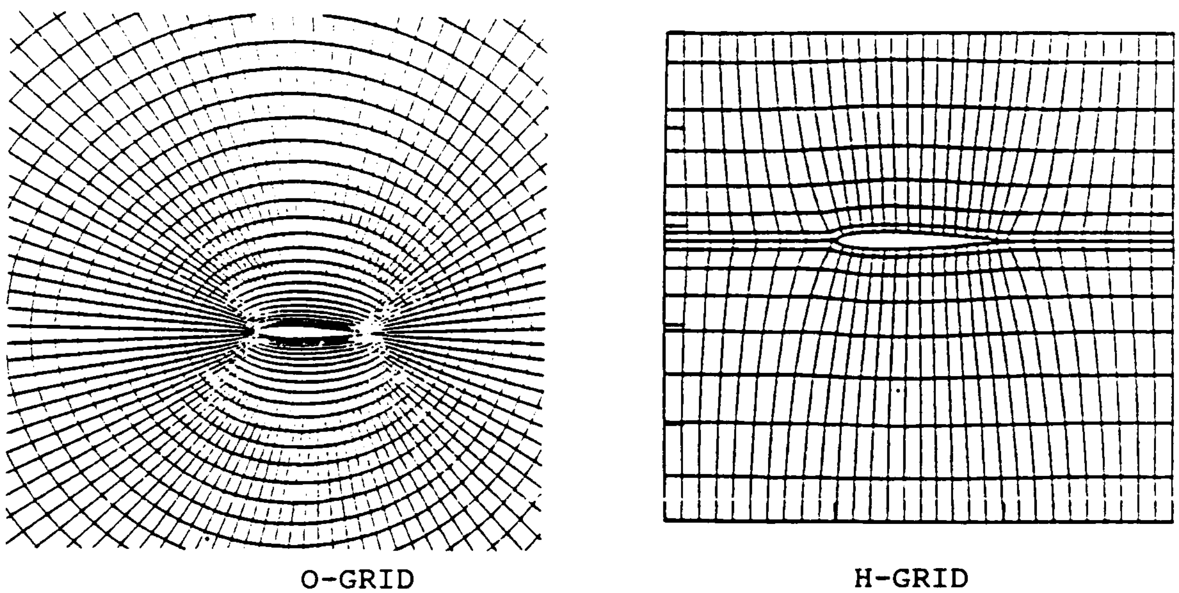

Figure 2.3. O-grid and H-grid Implementation

The O-grid design provides a means of evaluating the flow field interaction over the entire body, especially any flow interaction at the leading edge. This type of grid enhances the ability of physical flow phenomena to communicate between the surface planes without complex a boundary condition structure. The O-grid would also provide a baseline for follow-on research efforts in which realistic bodies are analyzed. The rounded leading edges, required to reduce peak heat transfer, are much easier to model using an O-grid. Finally, another key consideration was the structure of the explicit Euler algorithm. Its basic design was implemented for an O-grid system. Applying an alternate grid formulation would entail a modification to an already working, debugged algorithm.

The H-grid provides a means of applying a more theoretical approach to the inviscid application with very sharp leading edges proposed for this research thesis. However, this implementation would also require significant restructuring to handle any future application of realistic geometries and viscous effects. Although the H-grid formulation would reduce cell skewness at the leading edge, making surface orthoganility easier to maintain, it was discarded in favor of the an O-grid formulation.

2.2.2 Grid Structure

The O-grid system implemented for this research, illustrated in Figure 2.4, was based on an algebraic system to define the domain shape and cell distribution. The farfield domain was designed as an elliptic arc scaled to the cross-section of the waverider. The elliptic outer domain provided a means of modeling the expected shock wave shape near the plane of symmetry, while maintaining a constant shock wave development location for any specified cross-section. In the symmetry plane, the scaling of the outer domain forced lines of constant η to follow conical rays emanating from the nose of the waverider. For the baseline investigation of inviscid flow effects, an evenly spaced cell distribution was sought and enforced through the use of a geometric progression routine in areas of high curvature.

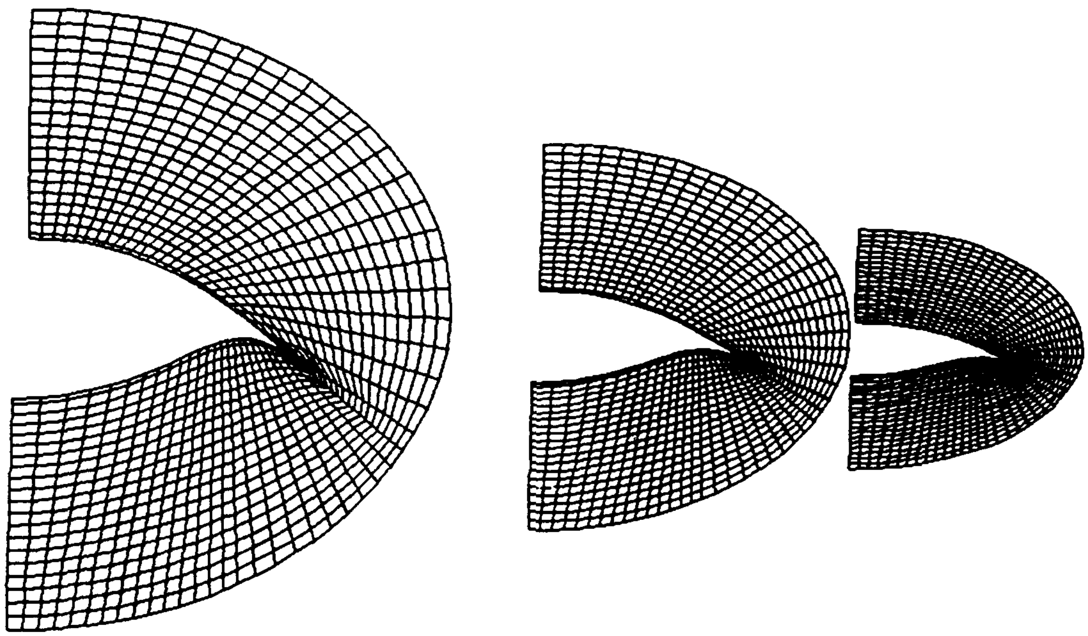

$z_w/l_w = 1.0$ $z_w/l_w = 0.75$ $z_w/l_w = 0.5$

Figure 2.4. Scaled Elliptic Grid System

2.3 Program WVRIDR

The Fortran-77 algorithm WVRIDR utilizes the analysis of Section 2.1 to define the surface of a parabolic-top waverider and develops a three-dimensional grid to capture the expected flow field for a specified supersonic/hypersonic design point. The code formulates a half body representation about the (X-Z) plane of symmetry, since no additional information is to be gained for the inviscid case from a full body representation at zero yaw angle. The three-dimensional grid is developed as a series of two-dimensional planar cross sections in the streamwise direction. The documented source code for program WVRIDR can be found in Appendix A.

2.3.1 PROGRAM MAIN

The main program specifies the design constants for a selected parabolic waverider configuration based upon the freestream Mach number, generating cone half angle and length, maximum spanwise sweep, and type of parabolic freestream surface. The default design parameters are specified in Table 2.1. The generating cone length ℓ was specified in order to generate a length scaling factor, $(\ell\delta)$, of 1.00. The specification of a tangent parabolic-top waverider defines the default $R_0 = X_\sigma/2$, which in turn defines the curvature coefficient $A = X_\sigma/Y_\sigma^2$. The grid dimensions are determined by a set of integer constants described in Table 2.2.

TABLE 2.1
Baseline Design Parameters

PARAMETER	VARIABLE	DEFAULT
Mach Number	M_∞	10.00
Cone Angle	δ	5.5°
Sweep Angle	ϕ_ℓ	50.0°
Cone Length	ℓ	10.4174
Surface Type	R_0	$X_\sigma/2 = 1/2$

Table 2.2
Grid Dimension Parameters

INTEGER	GRID NUMBERING DEFINITION
MCAP	# pts on freestream surface
INCR	# pts on entire planar surface
NCAP	# of planar cross sections
BNDS	# of shells to outer domain

2.3.2 Subroutine WAVEBODY

Subroutine WAVEBODY takes the design methodology of Section 2.1 and the design parameters of Section 2.3.1 to generate a freestream and matching compression surface for each planar cross section. The surface generation is computed in spherical coordinates utilizing Equations (2.6) and (2.10). The spherical coordinates are then converted into standard cartesian X,Y,Z non-dimensional coordinates through the transformation:

$$
\begin{aligned}
X &= R(\phi)\cos\phi \ \ (*\ell\delta) \\
Y &= R(\phi)\sin\phi \ \ (*\ell\delta) \\
Z &= r_s(\phi) \ \ (\div\ell)
\end{aligned}
\tag{2.18}
$$

The initial streamwise plane is truncated at $\phi_0 = 7^\circ$, as opposed to the theoretical limit of 0°. This truncation is necessary to generate an initial grid plane with a resolvable thickness. The default value of 7° is selected to begin the computational model at a z_w/ℓ_w location of no larger than a half percent of the waverider total length. This is the first deviation from the theoretical formulation. The planar progression parameter, PHI, representing the progression of the function $r_s(\phi)$; and the freestream surface sweep parameter, PHIZ, representing the sweep range per planar increment ϕ_z is defined using a geometric progression distribution function based on Newton's method in subroutine GEOM. This subroutine, as implemented by Beran (5), is utilized for all progression steps necessary in the formulation of the initial algebraic grid system. The progression factor for planar cross sections is chosen such that a constant z_w/ℓ_w step is realized with a slight bias at the nose of the waverider configuration where the conical shock formation occurs. The surface point progression factor is selected to maximize cell locations at the sharp leading edge of the waverider. This packing distribution is sought to capture information where shock attachment and/or spillage is expected. The output of this subroutine is the cartesian coordinates in physical space of the designated waverider configuration, illustrated in Figure 2.5.

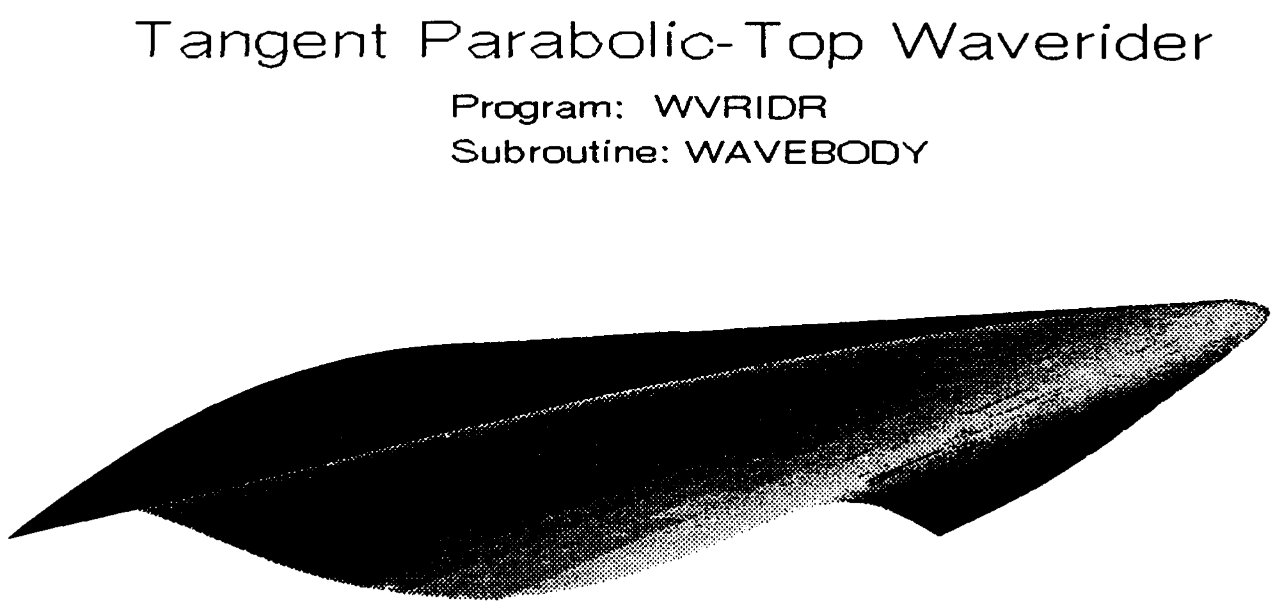

Figure 2.5. 3-D Waverider Perspective

2.3.3 Subroutine LEADEDG

Subroutine LEADEDG reads the three-dimensional surface generated in Subroutine WAVEBODY and truncates the analytically designed leading edge value with a slope intersection approximation to eliminate any cusp behavior of the original configuration illustrated in Figure 2.6.

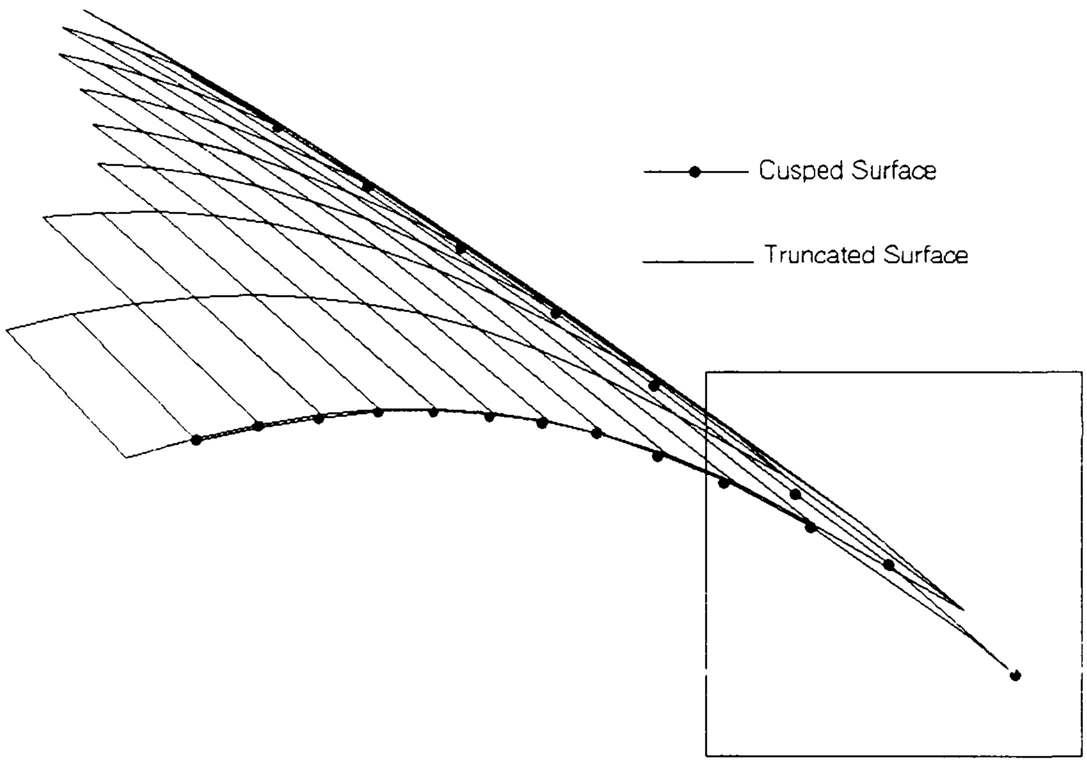

Figure 2.6. Cusped and Truncated Leading Edge Design

The motivation behind such a truncation is two-fold. The selection of an O-grid as a type of grid design calls for smooth curvature of physical thickness to avoid unacceptable cell skewness. High cell skewness is a threat to the stability as well as accuracy of the solution algorithm. Physical realism in the application of hypersonic flow also calls for a resolvable thickness to minimize the expected high values of aerothermodynamic heating. This later motivation, however, is not an issue for the inviscid, non-heat conducting flow model utilized in this research thesis, but does address an unattainable model design. It will be shown that the use of the finite volume algorithm will compensate for the cusped nature of the inviscid analytical design.

The truncation methodology is based on approximating a new leading edge location by determining the intersection of the freestream and compression surface slopes. The application of this methodology is shown in Figure 2.5. The slope of each respective surface is determined from the two surface points preceding (freestream surface) or following (compression surface) the cusped leading edge location. The new leading edge location is determined by the intersection of the freestream and compression surface slopes based on the linear point slope relationship:

$$Y = mX + b \tag{2.19}$$

2.3.4 Subroutine GRIDBNDS

Subroutine GRDBNDS defines the outer boundary domain for the computational model. The boundary selected is an elliptic arc scaled to the dimensions of each planar cross section. The major axis, B, is based on the spanwise distance to the leading edge is given by the formula

$$B = 1.5 * Y_{le} \tag{2.20}$$

The minor axis, A, is scaled to the distance from the center of the body at the line of symmetry, Xctr, and the distance to the conical shock σ_z as:

$$A = 1.5 * (\sigma_z - X_{ctr}) \tag{2.21}$$

The scaling of the outer boundary provides a means of utilizing the maximum number of grid cells for the solution of the on-design flow condition while minimizing excess solution points expected to remain at freestream conditions. The elliptic outer boundary was also found to have the same basic curvature of the expected conical shock wave near the axis of symmetry.

The point on the outer boundary corresponding to the leading edge location was mapped determined through the use of the freestream and compression surface slopes at the leading edge and the equation of the outer boundary ellipse. The solution to the planar coordinates to the outer boundary involved solving two equations for two unknowns:

$$1.)\quad \frac{(X-X_{ctr})^2}{(1.5*(\sigma_z-X_{ctr}))^2}+\frac{Y^2}{(1.5*Y_{le})^2}=1.0 \qquad (2.22)$$

$$2.)\quad Y = mX + b$$

Once the initial outer boundary grid location was determined, the distribution of outer boundary grid points could be applied. An initial investigation was conducted to determine the outer boundary distribution from a linear mapping in ϕ of both the freestream and compression surface to the outer elliptic boundary in θ. This mapping routine resulted in a highly non-orthogonal packing about the major axis. It was determined that the cell skewness was too great and this technique was discarded. The final solution relied on decoupling the distribution of grid point from the surface to the outer boundary. Grid points on the outer boundary required a relatively coarse packing at or near the major axis to account for the high curvature of the surface. A more refined packing scheme was applied in the areas of relatively parallel curvature of the surface compared to the outer boundary. An illustration of the grid development methodology is shown in Figure 2.7.

Each corresponding surface and outer boundary point was connected by a ray which was divided into nearly equal segments to form the crossplane based grid system. The evenly spaced grid cell distribution in each crossplane was determined to be a good baseline from which to initiate a solution since for inviscid flow, no resolution of a viscous boundary layer at or near the surface was required.

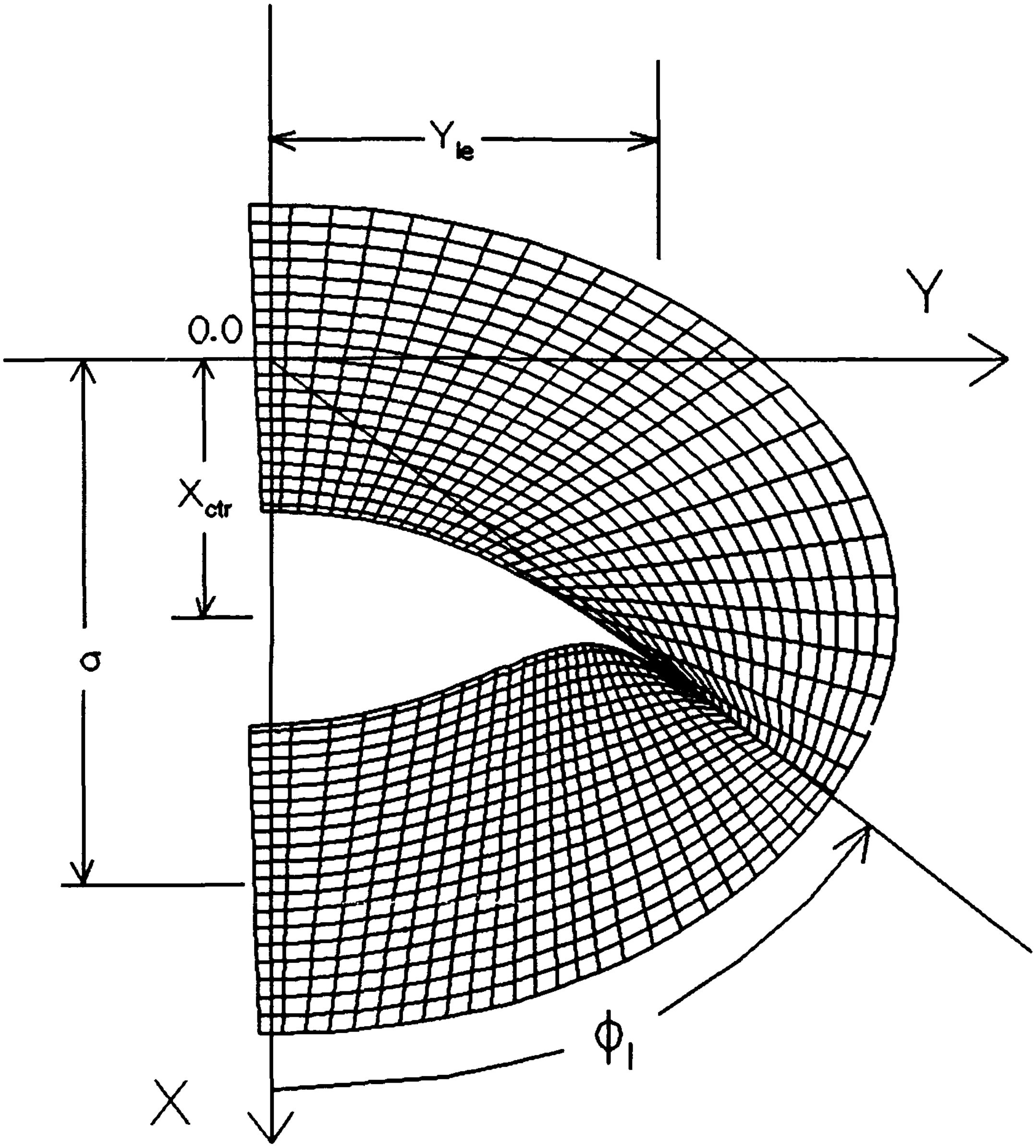

Figure 2.7. Elliptic Grid System Development: Baseplane

III. EULER EXPLICIT FLUX SPLITTING ALGORITHM

3.1 Code Description

The Wright Laboratory's new three-dimensional explicit Roe flux-splitting Euler code, developed by D. Gaitonde (11) was used to solve the hypersonic, inviscid flow over a waverider configuration. An updated version of the code was formulated to specifically handle waverider flow conditions. This version was debugged on the ASD Cray X-MP supercomputer utilizing a Silicon Graphics Iris workstation. The source code was then transferred to a UNIX based SPARCs station located in the AFIT computer Laboratory. This workstation was used as a front end device for code manipulation. All solution runs for this research thesis were completed on a Cray Y-MP/864, located at the Ohio State University's Super-Computer Center. Access to the Cray Y-MP was accomplished through a grant for research on, " Numerical Solutions of the Euler Equations for Hypersonic Flow around a Conically-Derived Waverider Body." Connections were made via telnet from the AFIT SPARCs workstation.

A single version of the Euler explicit source code was maintained on the Cray Y-MP, with binary executable files stored in each of the on and off-design case directories. The Euler source code required two initial start files; a binary grid file; and an input file. The grid file, CN1GRD.BIN, was generated from source code WVRIDR and converted to a cell centered coordinate system by WVRGRD provided by D. Gaitonde for the right handed system defined by:

ξ - *X* - *streamwise axis*

η - *Y* - *surface normal axis*

ζ - *Z* - *spanwise axis*

For which the Z and X coordinates were switched to align the coordinate directions in an X directed streamwise plane.

The input file, 100K1DAT, provides the necessary input parameters to completely specify the flow field conditions for a generic blunt-body model solved utilizing the Euler equations. The information utilized in the input file, 100K1DAT, for this research thesis can be subdivided into four basic categories. These categories describe the solution integration parameters; the flow field conditions; the body geometry specifications; and the output format parameters. The following is a listing by catagory of the key input parameters utilized in the Euler code.

1) Solution Integration Parameters

INS	Governing Equation (0: Euler)
ICASE	Boundary Conditions (8: Waverider)
ILCTST	Local/Global Time Step(1: Local)
ICFL	CFL Doubling Criteria
CFLEXP	Iteration Cycle for CFL Doubling
CFLMAX	Maximum Value of CFL Number
CFL	Initial Value of CFL Number
IMPLT	Solver (0: Explicit)
ISWVL	Solution Scheme (4: Roe)
ILMTR	Limiter Selection (2: MINMOD)

2) Flow Field Parameters

ALPHA	Angle of Attack (radians)
PHI	Yaw Angle
RM	Freestream Mach Number
REL	Reynolds Number
TINF	Freestream Temperature
PINF	Freestream Pressure
IADBWL	Adiabatic Wall Condition
TWALL	Wall Temperature (N/A for Adiabatic)

3) Geometry Parameters

IL	Number of Streamwise Planes
JL	Number of Surface Normal Planes
KL	Number of Spanwise Planes
IMETRC	Unit of Measure (0: fps)
RL	Body Reference Length

4) Output Parameters

NEND	Iteration Limit
IREAD	Restart Condition
IGRID	Format For Input Grid
IP3DOP	Format For PLOT3D Output Files
MODPR	Interactive Iteraction Cycle

This listing contains only the parameters specifically affecting the code for the research case at hand. The actual format of the input file, 100K1DAT, can be found in Appendix B. Tables showing the values of the listed key parameters are also detailed in Appendix B for each specific investigation. Modification of the input file was minimized once the case specifications were identified. For the initial start, the parameter IREAD was set to zero to indicate a no restart status. For restarts, only the parameters IREAD, and NEND were affected. Final runs required a format choice of either

ASCII or binary through IP3DOP for the choice of output flow parameters.

The interactive nature of the source code required that an iteration limit be imposed to ensure effective use of limited Cray central processor unit (CPU) time. Runs were completed in sets of 100 iterations per restart. Run times ranged from 60 CPU seconds per 100 iterations for the baseline, 21 x 21 x 52, grid to a high of 140 CPU seconds per 100 iterations for the most refined case of 31 x 31 x 62 grid. Restarts were initiated by transferring the binary output file, CN100OT, which contained flow field data, to the continuation, read file, CN100IN. The iteration limit and restart flag were then revised in the input file, 100K1DAT.

A value of 10^{-6} was specified as the baseline limit of the residual norm specifying sufficient flow field convergence. The residual norm was based on an L_2 formulation based on a root mean square of the entire set of conservative flow variables, normalized to the initial solution of the form:

$$\frac{1}{IL*JL*KL}\sqrt{\sum_{i=1}^{IL}\sum_{j=1}^{JL}\sum_{k=1}^{KL}\sum_{L=1}^{5}\left(\frac{R_L}{[U]_\infty}\right)^2}$$

$$L:\ component\,of\,the\,conservative\,flow\,variable \tag{3.1}$$

$$\frac{R_1}{[U]_\infty} = \frac{\Delta\rho}{\rho_\infty}\quad ...\ etc$$

Convergence was attained in a range from 800 to 1000 iterations for the baseline and refined cases, respectively. A typical convergence profile is illustrated for the on-design cases investigations in Figure 3.1.

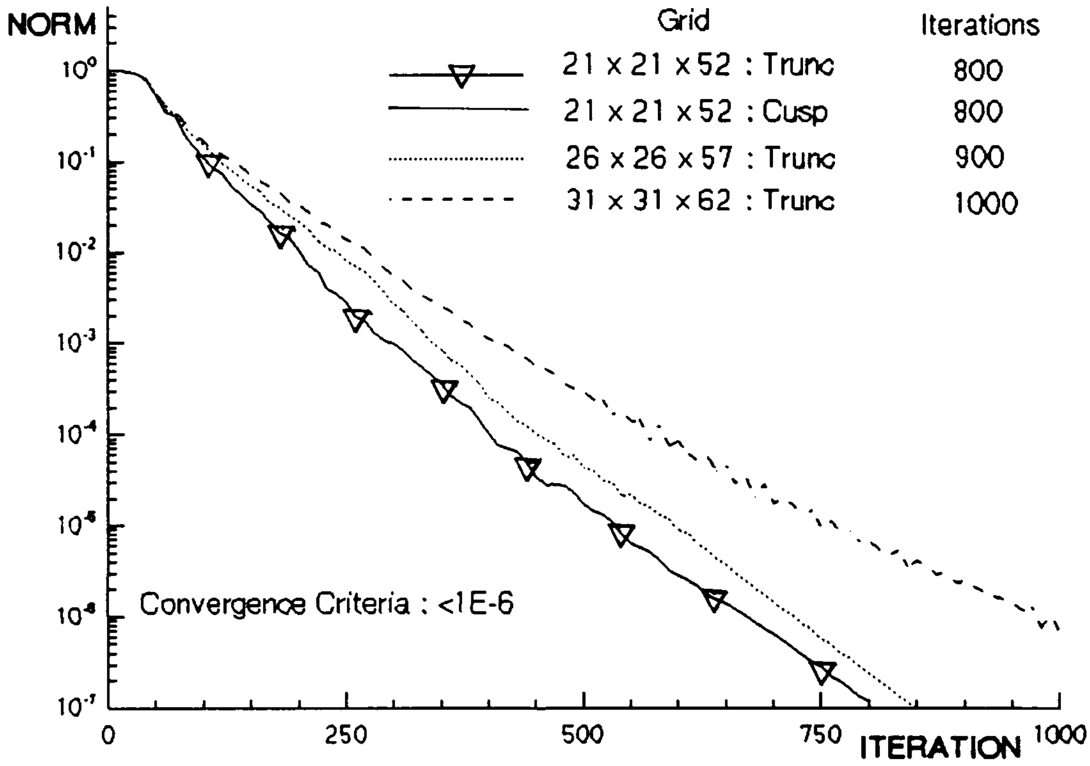

Figure 3.1. Euler Code Convergence Histories

3.2 Euler Code Output

The source code utilized a standard McCormack explicit time integration methodology to solve the inviscid governing equations for the conservative flow variables, $(\rho, \rho u, \rho v, \rho w, \rho e)^T$. These variables were converted for output purposes to the primitive form of the velocity vectors (u,v,w), the Mach number, and pressure coefficient. The final output files, PRIM100.G, and PRIM100.Q, representing the primitive variables, $(u, v, w, M, c_p)^T$, in PLOT3D format, where the .G file contains the grid specifications and the .Q file contains the values of the primitive variable. An ASCII format was selected to alleviate any translation anomalies associated with Cray binary format being read by a SPARCs based UNIX station.

Additional flow field information was derived to determine the lift to drag ratio (L/D) of the waverider. Cell pressure values were numerically integrated over the body surface to obtain values for the body normal and tangential forces. The lift and drag forces were then calculated from the body normal and tangential forces by the relation (2:14):

$$\begin{aligned} L &= N\cos\alpha - T\sin\alpha \\ D &= N\sin\alpha + T\cos\alpha \end{aligned} \tag{3.2}$$

Where N is the normal force, T is the tangential force, and α is the angle of attack. For the baseline case where α is zero, Equation (3.2) reduces to L = N, and D = T.

Analysis of the flow field data focused on three main areas. The first concern centered on how well the code modeled the theoretical waverider solutions. Key investigations included the shock attachment at the leading edge and non-divergence of the compression surface streamlines. A comparison with the analytical results of

Rasmussen was then conducted, centering on the lift to drag ratio. A final investigation was performed, comparing the trend of the maximum pressure coefficient value on the waverider surface to the HSDT approximation of the pressure coefficient on the generating cone for a variety of Mach numbers. Chapter IV covers the results of the computational investigations for on and off design cases as compared to HSDT waverider theory. Chapter V develops the framework of the analytical solutions and compares the numerical results from Chapter IV to the analytical evaluations.

3.3 Governing Equations

The governing equations utilized in this research effort were derived from the inviscid, adiabatic, homentropic form of the Navier Stokes Equations. This form of the Navier-Stokes equations is known as the Euler equations. These equations were further specialized for the implemented case of negligible body forces. In three-dimensional Cartesian generalized coordinates, the Euler equations are formulated as:

Continuity:

$$\frac{\partial \rho}{\partial t} + \frac{\partial (\rho u)}{\partial x} + \frac{\partial (\rho v)}{\partial y} + \frac{\partial (\rho w)}{\partial z} = 0 \tag{3.3}$$

X Momentum:

$$\rho \frac{\partial u}{\partial t} + \rho u \frac{\partial u}{\partial x} + \rho v \frac{\partial u}{\partial y} + \rho w \frac{\partial u}{\partial z} = -\frac{\partial P}{\partial x} \tag{3.4}$$

Y Momentum:

$$\rho \frac{\partial v}{\partial t} + \rho u \frac{\partial v}{\partial x} + \rho v \frac{\partial v}{\partial y} + \rho w \frac{\partial v}{\partial z} = -\frac{\partial P}{\partial y} \tag{3.5}$$

Z Momentum:

$$\rho \frac{\partial w}{\partial t} + \rho u \frac{\partial w}{\partial x} + \rho v \frac{\partial w}{\partial y} + \rho w \frac{\partial w}{\partial z} = -\frac{\partial P}{\partial z} \tag{3.6}$$

Energy:

$$\frac{\partial E_t}{\partial t} + u \frac{\partial E_t}{\partial x} + v \frac{\partial E_t}{\partial y} + w \frac{\partial E_t}{\partial z} = -\left(u \frac{\partial P}{\partial x} + v \frac{\partial P}{\partial y} + w \frac{\partial P}{\partial z} \right) \tag{3.7}$$

In vector notation these equations can be combined into a single partial differential equation (PDE) of the form

$$\frac{\partial \boldsymbol{U}}{\partial t} + \frac{\partial \boldsymbol{E}}{\partial x} + \frac{\partial \boldsymbol{F}}{\partial y} + \frac{\partial \boldsymbol{G}}{\partial z} = 0 \tag{3.8}$$

Where **U** is the conservative flow vector

$$\boldsymbol{U} = \begin{bmatrix} \rho \\ \rho u \\ \rho v \\ \rho w \\ E_t \end{bmatrix} \tag{3.9}$$

AND **E**, **F**, and **G** are the flux vectors (1:242-243).

$$\boldsymbol{E} = \begin{bmatrix} \rho u \\ \rho u^2 + P \\ \rho uv \\ \rho uw \\ (Et + P)\, u \end{bmatrix} \quad \boldsymbol{F} = \begin{bmatrix} \rho v \\ \rho uv \\ \rho v^2 + P \\ \rho vw \\ (Et + P)\, v \end{bmatrix} \quad \boldsymbol{G} = \begin{bmatrix} \rho w \\ \rho uw \\ \rho vw \\ \rho w^2 + P \\ (Et + P)\, w \end{bmatrix} \tag{3.10}$$

It is necessary to solve Equation (3.8) to obtain the converged conservative flow vectors at each cell centered flow point in the computational domain. The solution of these equations is accomplished by applying a Roe flux-splitting scheme to the three-dimensional problem. A brief description follows on a simple one-dimensional application of the scheme.

3.4 Flux-Splitting

A flux-splitting algorithm is applied to Equation (3.8) in a manner such that the positive and negative eigenvectors are resolved into separate, differenced flux jacobians representing flow conditions on either side of a grid cell. This methodology, first presented in detail by Steger and Warming (23) can be found in numerous other references including the following synopsis from Anderson, Tannehill and Pletcher (1:281-283).

To model the application, a one-dimensional inviscid, hyperbolic PDE is considered

$$\frac{\partial \boldsymbol{U}}{\partial t} + \frac{\partial \boldsymbol{E'}}{\partial x} = 0 \tag{3.11}$$

in linearized form (3.11) becomes

$$\frac{\partial \boldsymbol{U}}{\partial t} + [\boldsymbol{A}] \frac{\partial \boldsymbol{U}}{\partial x} = 0 \tag{3.12}$$

where [**A**] is the flux jacobian matrix $\partial \mathbf{E}/\partial \mathbf{U}$.

A similarity transformation is applied to [**A**] to generate the eigenvalue matrix

$$[\boldsymbol{T}]^{-1}[\boldsymbol{A}][\boldsymbol{T}] = [\Lambda] \tag{3.13}$$

where [**T**] is the right eigenvector matrix and $[\Lambda]$ is the diagonal matrix of eigenvalues. The split vector, for a homogeneous equation of degree one, can be written as

$$\boldsymbol{E} = [\boldsymbol{A}]\boldsymbol{U} = [\boldsymbol{T}][\Lambda][\boldsymbol{T}]^{-1}\boldsymbol{U} \tag{3.14}$$

The matrix of eigenvalues is then separated into positive and negative elements such that

$$[\boldsymbol{A}] = [\boldsymbol{A}]^{+} + [\boldsymbol{A}]^{-} = [\boldsymbol{T}][\Lambda^{+}][\boldsymbol{T}]^{-1} + [\boldsymbol{T}][\Lambda^{-}][\boldsymbol{T}]^{-1} \tag{3.15}$$

After some manipulation, the one-dimensional form of equation (3.8) can be written as

$$\frac{\partial \boldsymbol{U}}{\partial t} + \frac{\partial \boldsymbol{E}^{+}}{\partial x} + \frac{\partial \boldsymbol{E}^{-}}{\partial x} = 0 \tag{3.16}$$

3.5 Roe Scheme

The flux split approach was then applied to the Roe scheme by defining the positive and negative flux jacobians as

$$[\mathbf{A}]^{+} = \frac{1}{2}(\mathbf{A}+\tilde{\mathbf{A}})$$
$$[\mathbf{A}]^{-} = \frac{1}{2}(\mathbf{A}-\tilde{\mathbf{A}}) \qquad (3.17)$$

where $\tilde{\mathbf{A}}$ is defined as

$$\tilde{\mathbf{A}} = [\mathbf{T}]\,|\Lambda|\,[\mathbf{T}]^{-1} \qquad (3.18)$$

where $|\Lambda|$ consists of the magnitude of the elements found in $[\Lambda]$ (5:114).

Casting Equation (3.8) as an explicit first order accurate, upwind scheme

$$U_i^{n+1} = U_i^n - [\mathbf{A}]\,\lambda\Phi$$
$$\lambda = \frac{\Delta t}{\Delta x}$$
$$\Phi = U_{i+1}^n - U_i^n \qquad (\mathbf{A}^-) \qquad (3.19)$$
$$\Phi = U_i^n - U_{i-1}^n \qquad (\mathbf{A}^+)$$

In finite-difference form, Equation (3.19) can be recast as

$$U_i^{n+1} = U_i^n - \frac{\lambda}{2}\mathbf{A}(U_{i+1}^n - U_{i-1}^n) + \frac{\lambda}{2}\tilde{\mathbf{A}}(U_{i+1}^n - 2U_i^n + U_{i-1}^n) \qquad (3.20)$$

The order of accuracy remains first order; however, the approximation of the term $\mathbf{A}U_x$ is improved to second-order while stability is achieved through the dissipative nature of the added first order approximation of the term, $\Delta x/2\tilde{\mathbf{A}}U_{xx}$. This can be seen by dividing Equation (3.19) by Δt and regrouping the terms in short hand notation

$$U_t = -\mathbf{A}U_x + \frac{\Delta x}{2}\tilde{\mathbf{A}}U_{xx} \qquad (3.21)$$

The source code applies this approach through the definition of the numerical flux function

$$U_i^{n+1} = U_i^n - \lambda(H^n_{i+\frac{1}{2}} - H^n_{i-\frac{1}{2}}) \qquad (3.22)$$

where the nonlinear form of the flux function is applied

$$H^n_{i+\frac{1}{2}} = \frac{1}{2}(E_i^n + E_{i+1}^n - \frac{1}{\lambda}Q(U_{i+1}^n - U_{i-1}^n)) \qquad (3.23)$$

for the coefficient of numerical viscosity, Q, in the form

$$Q = \lambda\tilde{\mathbf{A}} = \frac{\Delta t}{\Delta x}\tilde{\mathbf{A}} \qquad (3.24)$$

(5:113-119).

The same approach can be applied to non-linear systems through the use of the mean valued jacobian $\hat{\mathbf{A}}$ applied at the cell interfaces such that

$$\hat{\mathbf{A}}_{i+\frac{1}{2}} = \mathbf{A}(\frac{U_i + U_{i+1}}{2}) \qquad (3.25)$$

This averaging technique is known as Roe averaging. The numerical flux function for the Roe averaged approach is cast as

$$H^n_{i+\frac{1}{2}} = \frac{1}{2}(E_{i+1}^n + E_i^n - (\hat{T}_{i+\frac{1}{2}}|\hat{\Lambda}_{i+\frac{1}{2}}|\hat{T}^{-1}{}_{i+\frac{1}{2}})^n(U_{i+1}^n - U_i^n)) \qquad (3.26)$$

(5:124-126).

A standard McCormack explicit time integration solver is applied to the above methodology based on alternating sweeps through the domain. Local time stepping is utilized based on a reference length equivalent to the length of the waverider model. The CFL condition is initialized at a value of .01 and doubled every ten iterations to a maximum value of .09.

3.6 Boundary Conditions

The boundary conditions imposed on the computational domain are derived from a flow field with supersonic inflow and outflow and a freestream farfield condition. An illustration of the transfer of the boundary conditions from the physical to the computational domain is provided in Figure 3.2.

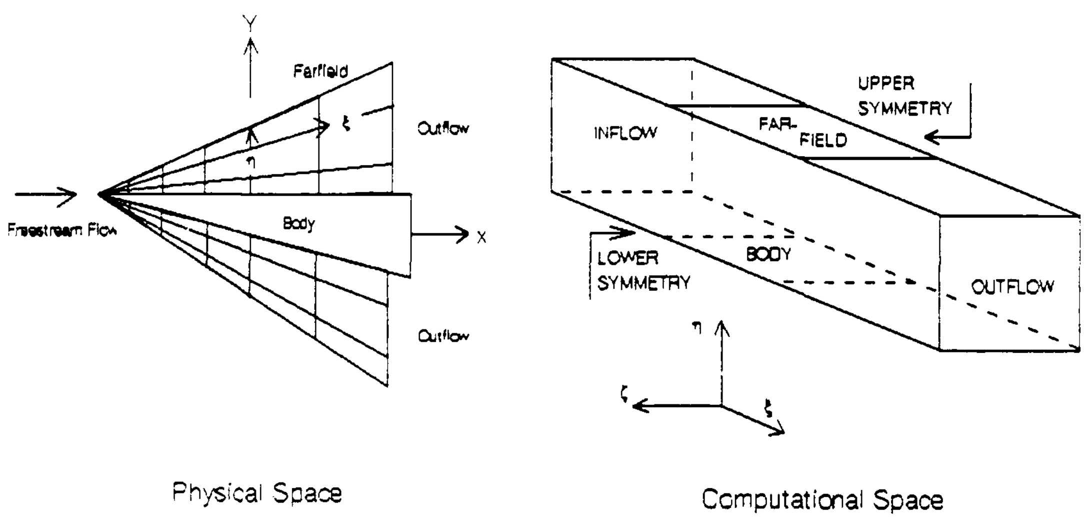

Figure 3.2. Application of Waverider Boundary Conditions

The inflow condition is modeled by a fictitious plane at i=1, upstream of the leading edge of the waverider. Freestream conditions are imposed in this plane as:

$$(\rho, \rho u, \rho v, \rho w, \rho e)^T_{1,J,K} = (\rho, \rho u, \rho v, \rho w, \rho e)^T_{\infty} \qquad (3.27)$$

The outflow condition is modeled as a zero gradient extrapolation:

$$(\rho, \rho u, \rho v, \rho w, \rho e)^T_{IL,J,K} = (\rho, \rho u, \rho v, \rho w, \rho e)^T_{IL-1,J,K} \qquad (3.28)$$

The bilateral symmetry conditions are imposed in such a way as to ensure the correct gradient of the crossflow as:

$$\begin{aligned} (\rho, \rho u, \rho v, \rho w, \rho e)^T_{I,J,1} &= (\rho, \rho u, \rho v, -\rho w, \rho e)^T_{I,J,2} \\ (\rho, \rho u, \rho v, \rho w, \rho e)^T_{I,J,KL} &= (\rho, \rho u, \rho v, -\rho w, \rho e)^T_{I,J,KL-1} \end{aligned} \qquad (3.29)$$

The farfield condition at J=JL is forced to freestream conditions as modeled in Equation (3.27). The surface condition at J=1/2 is enforced by the flux conditions of the Roe averaged variables from the cell centered planes J=1 and J=2.

IV. COMPUTATIONAL RESULTS

Numerical solutions were attained for four on-design cases: a baseline case, a leading edge truncation investigation, and a grid refinement study involving two levels of refinement from the baseline. The baseline case was conducted on a parabolic-top waverider with the specifications listed in Table 4.1.

TABLE 4.1
Baseline Specifications

Parameter	Specification
L.E. Truncation	Surface Slope
Nose Truncation	$\phi_0 = 7°$
Grid Dimension	21 x 21 x 52
Half Angle: δ	5.5°
Mach Number	10.0
Altitude	100,000 ft
Reynolds Number	10^7

The investigation of the effects of leading edge truncation involved computing the fully cusped waverider model applied to the baseline case. The grid refinement study involved a grid refinement of approximately 20% in the streamwise, body normal, and spanwise directions for each investigation. The refinement levels investigated were:

Baseline	:	21 x 21 x 52
Case 1r	:	26 x 26 x 56
Case 2r	:	31 x 31 x 62

Two off-design investigations were conducted to determine the performance characteristics of the waverider in a slightly perturb flow field. The first off-design investigation involved a study of the conical shock wave development and flight characteristics for a range of Mach numbers from eight to twenty. The second off-design study examined performance for a range of angle of attack values from -5° to 5°.

4.1 On-Design Investigation

The purpose of the initial on-design evaluations was to validate the numerical solutions against basic waverider theory. Waverider theory predicts an attached conical shock wave along the body's entire leading edge. A major characteristic of this phenomena is parallel streamlines through the shock wave and along the entire surface of the body. This phenomena provides the benefit of a high pressure field maintained along the compression surface due to the avoidance of cross flow from the streamwise symmetry line. According to Emanuel (9:399-400), the flat bottom delta wing designs like the Space Shuttle do not produce optimum lift values due to cross flow phenomena. Waverider designs account for this loss through the inverse design methodology which seeks parallel streamlines as shown in Figure 4.1.

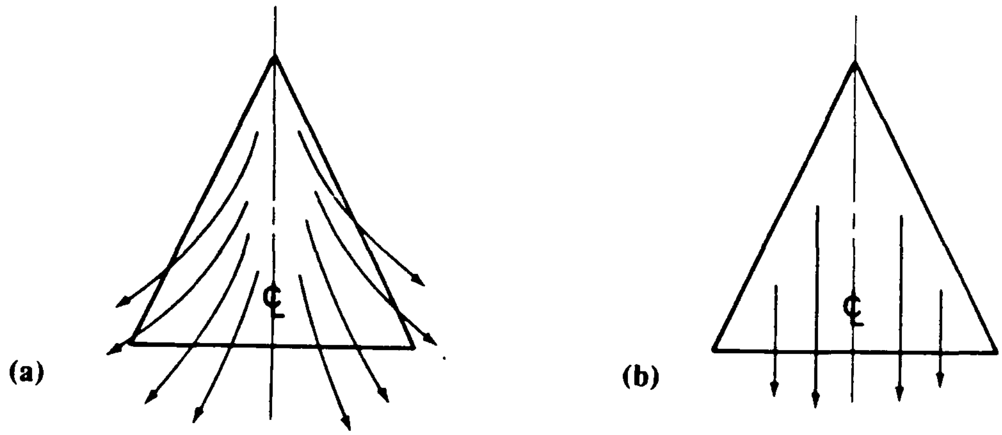

Figure 4.1. Flat Bottom, Delta Wing Configuration (b) versus Waverider Streamlines (a) (9:400)

4.1.1 Baseline Investigation

The baseline case showed good agreement with waverider theory for a fairly coarse grid structure. This grid structure is illustrated in Figure 4.2.

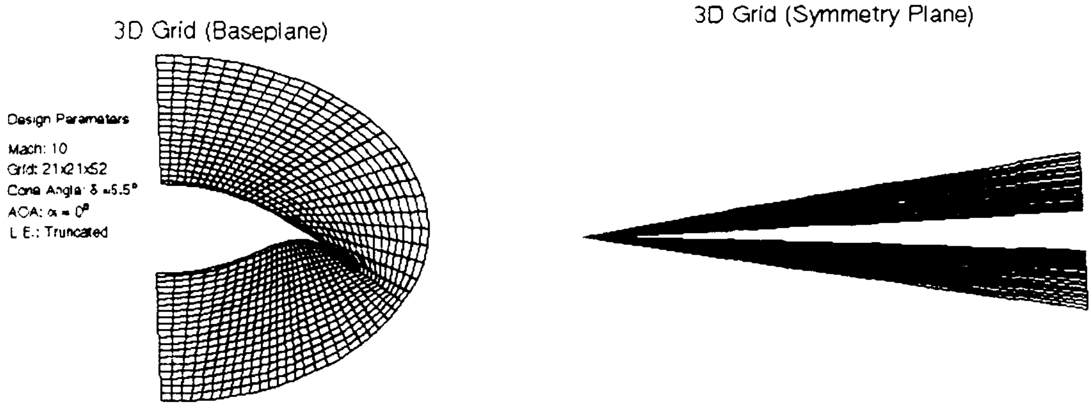

Figure 4.2. Grid Structure: Baseline (21 x 21 x 52)

The baseline case required run times of approximately 60 CPU seconds per 100 iterations, with a normalized residual L_2 norm of 1.158E-7, based on Equation (3.1), after 800 total iterations. Flow field convergence files for each on design case can be found in Appendix C. The numerical results for the on-design investigations is listed in Table 4.2.

Table 4.2
On-Design Results

STUDY	GRID	L_2 NORM	ITER	L/D	CPmax
Baseline	21x21x52	1.158E-7	800	8.078	.0217
Cusped	21x21x52	1.158E-7	800	8.089	.0217
Case1r	26x26x56	4.439E-8	900	8.090	.0217
Case2r	31x31x62	6.089E-8	1000	8.108	.0218

Figure 4.3 illustrates the attachment of the captured portion of the conical shock wave in the baseplane.

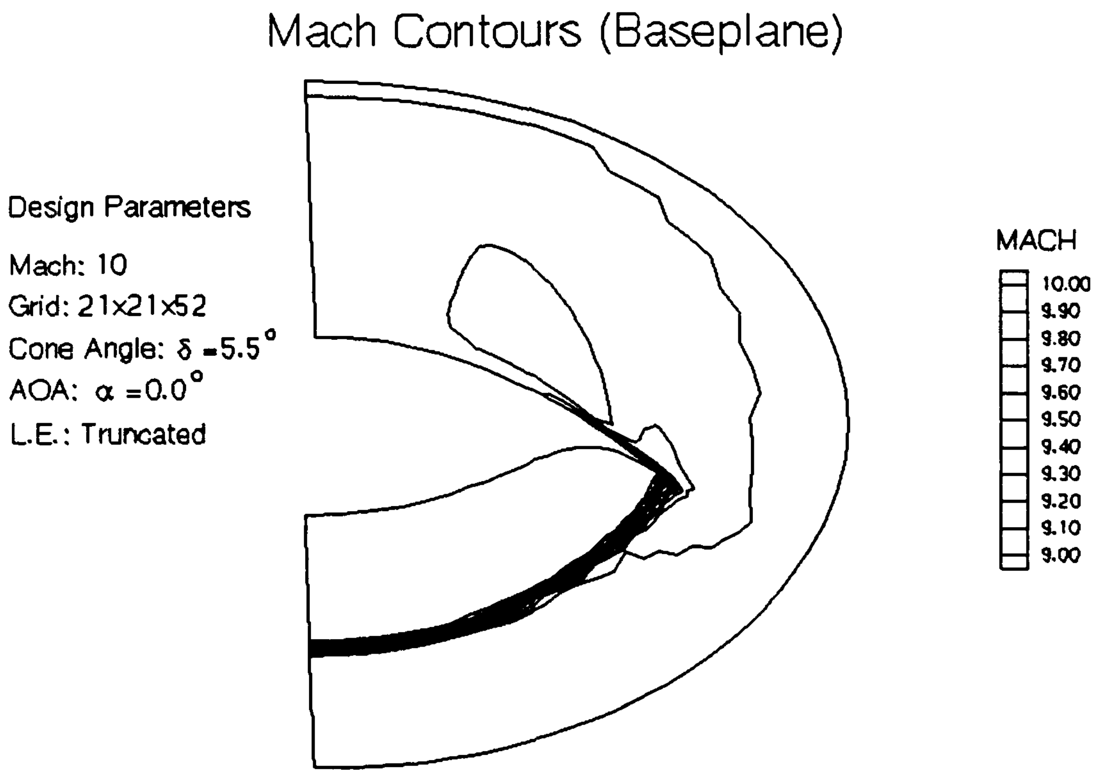

Figure 4.3. Conical Shock Wave Formation: Baseline

The effect of the leading edge truncation can been seen in the slight expansion of the flow from the compression surface to the freestream surface. An expanded view of this effect can be seen in Figure 4.4.

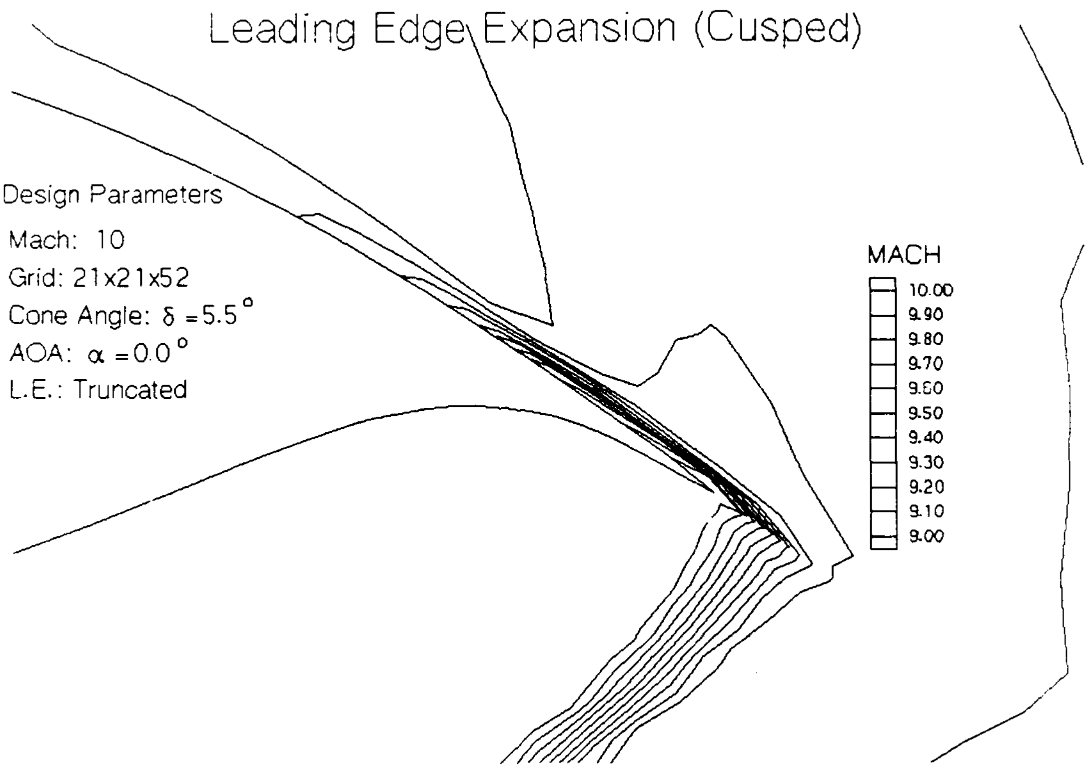

Figure 4.4. Leading Edge Flow Expansion: Baseline

A weak bow shock over the freestream surface is also produced due to the truncation of the leading edge nose region of the model. Figure 4.5 illustrates the development of this weak bow shock from a symmetry plane perspective.

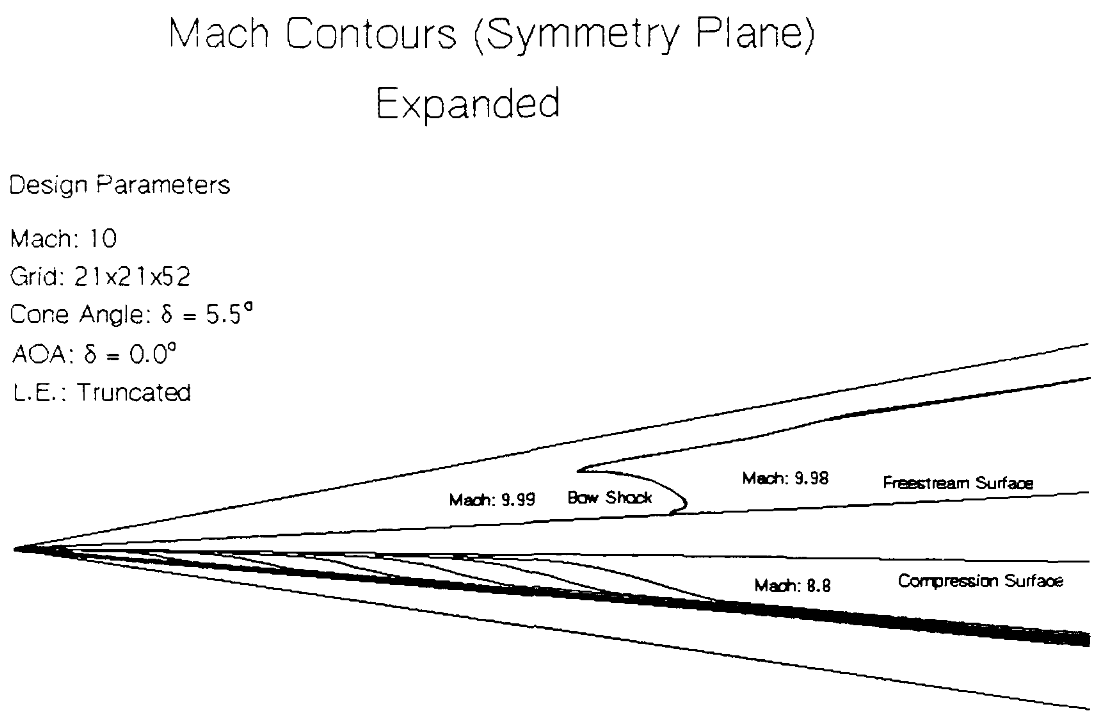

Figure 4.5. Bow Shock Development: Baseline

The effect of the flow expansion over the leading edge and through the bow shock is a resultant loss in both the lift and lift to drag ratio, L/D. The resultant loss is due to the non-freestream conditions present on the freestream designed surface. These effects will be examined versus the theoretical solutions in Chapter V.

The conical shock wave was captured within one grid cell at the line of symmetry, located at 60% of the grid for each planar cross section as per design. The shock wave's radial location, according to the HSDT parameter σ, was resolved in the baseplane at values between $1.487 \le \sigma \le 1.525$ as compared to the theoretical design value of 1.512.

The streamlines remained parallel through the conical shock wave along the entire compression surface of the waverider with a resultant steady increase in the surface pressure coefficient as illustrated in Figure 4.6.

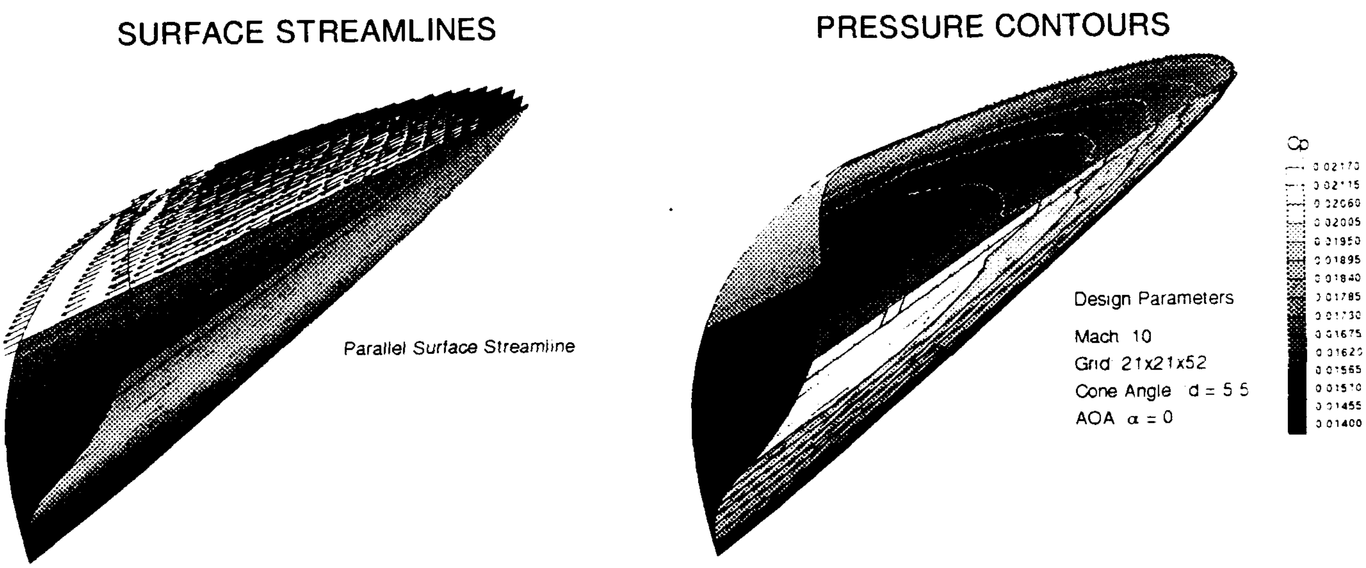

Figure 4.6. Theoretical Flow Evaluation: Baseline

Coefficient of pressure (c_p) values on the compression surface ranged from 0.018 to 0.217 along the midline symmetry plane with the peak c_p value located at 86.25% of the length of the waverider as illustrated in Figure 4.7.

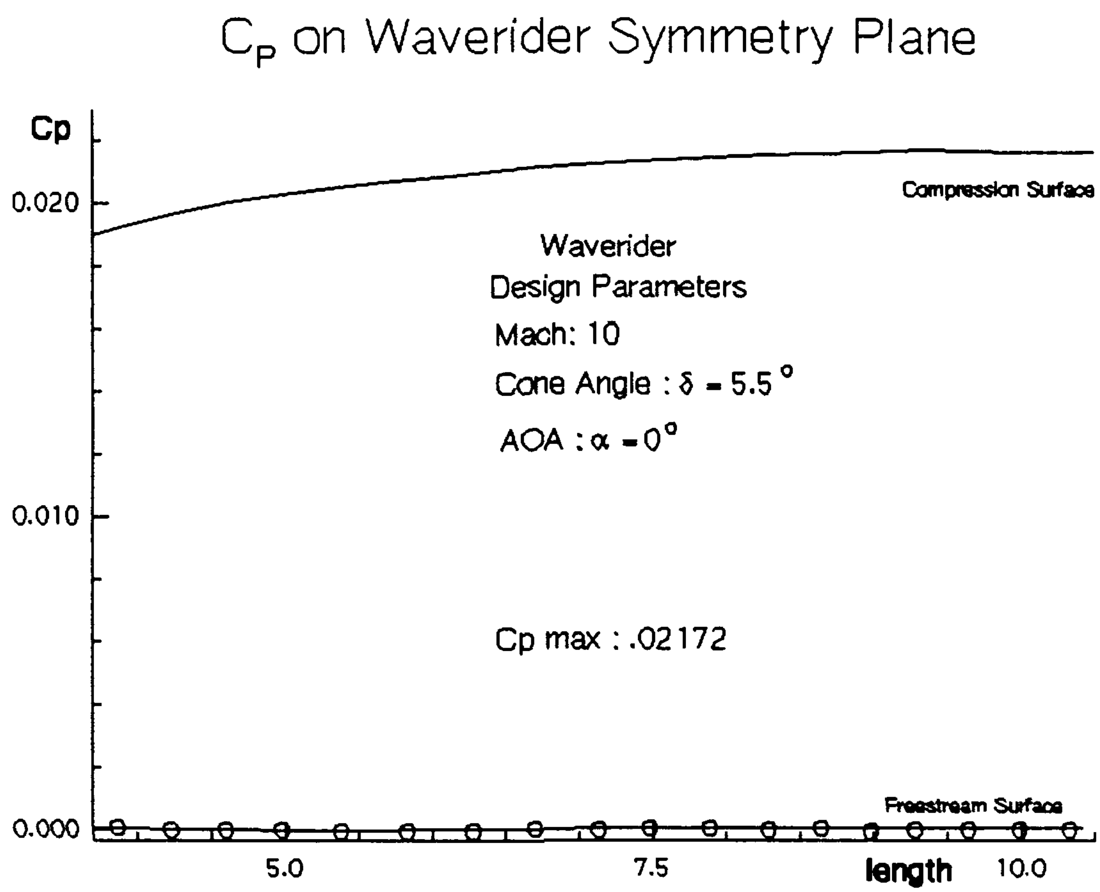

Figure 4.7. Symmetry Plane C_P Values: Baseline

4.1.2 Cusped Waverider Model

An identical baseline grid distribution was applied to a waverider model with no leading edge truncation. This solution was designed to test the Euler code for stability in areas of high cell skewness. The cusped model grid structure is shown in Figure 4.8.

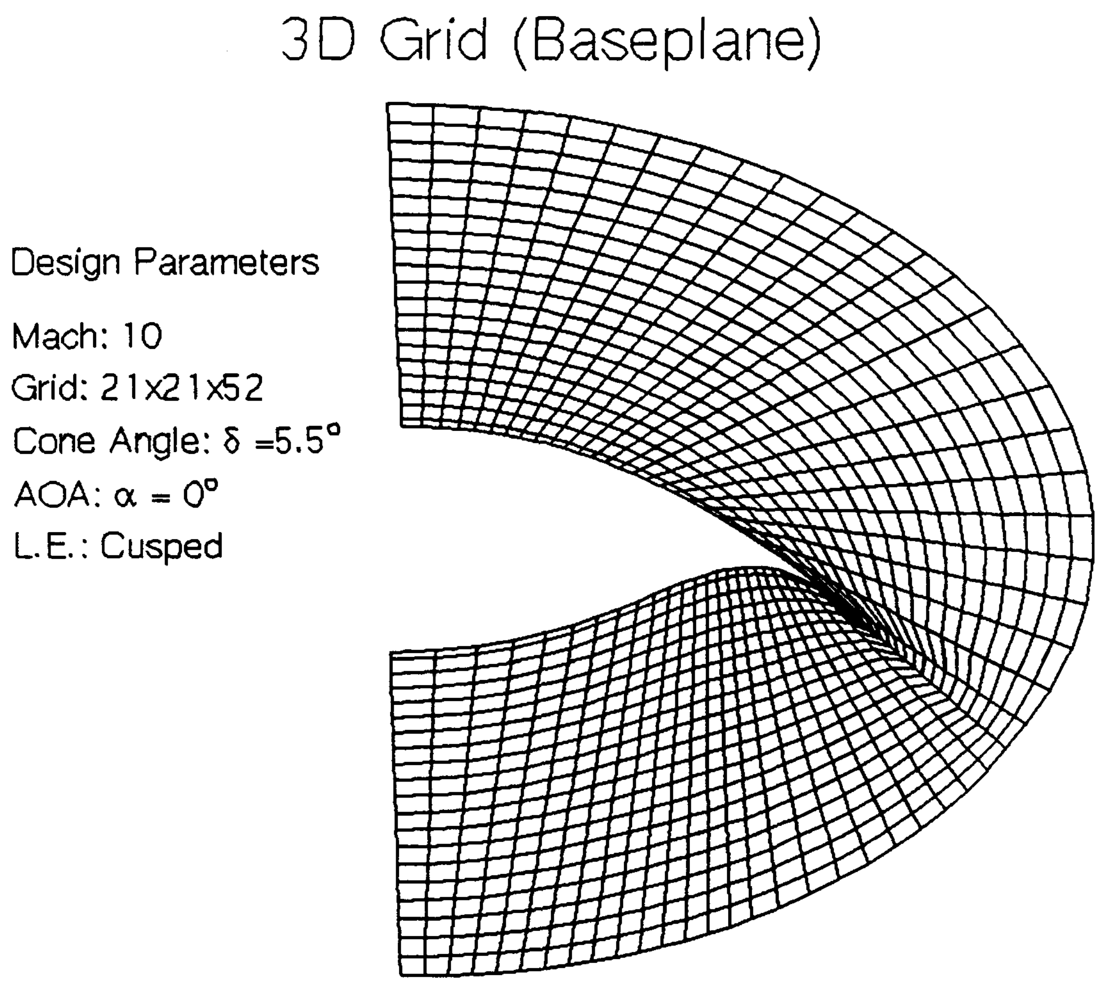

Figure 4.8. Grid Structure: Cusped (21 x 21 x 52)

The cusped model produced a near identical convergence history when compared to the baseline case. A slight improvement in the lift was noted due in part to a reduction of leading edge truncation.

The shock attachment at the leading edge was more noticeably refined. However, flow expansion around the leading edge was still present as illustrated in Figure 4.9.

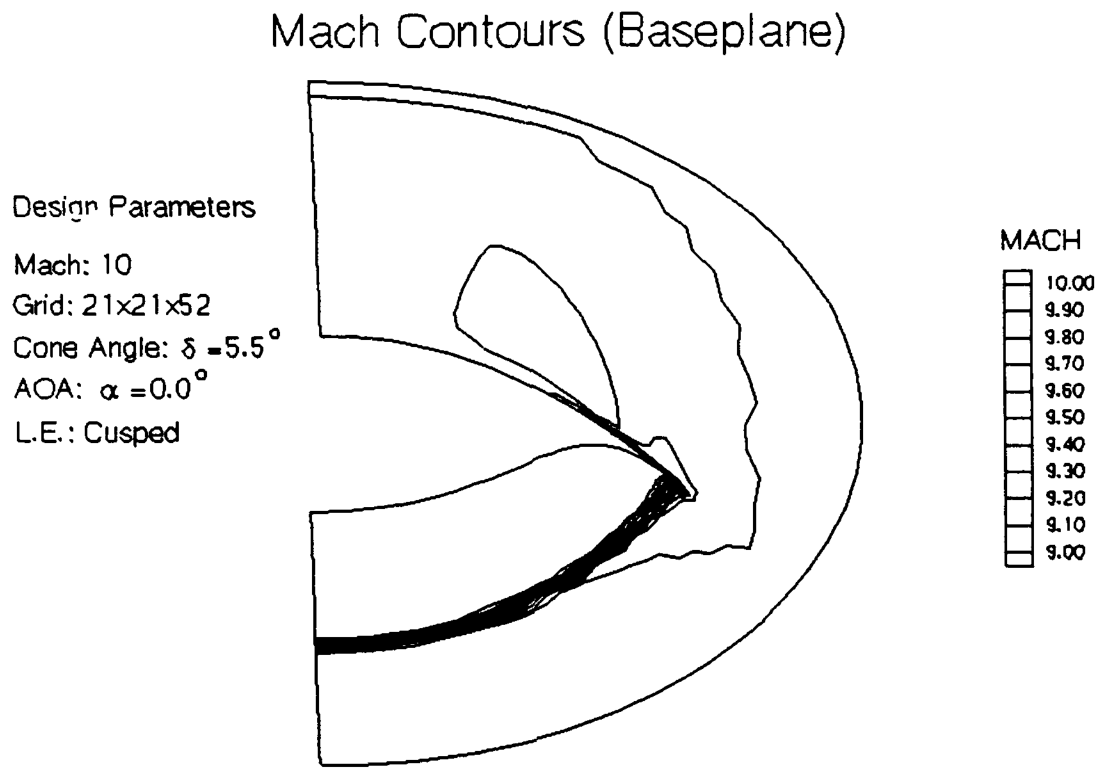

Figure 4.9. Conical Shock Wave Development: Cusped

A further investigation of the computational, cell-centered modeling methodology showed numerical truncation present, most noticeably in the nose region of the model where the leading edge was blunted. This can be seen in a comparison of the initial cross sectional surface to the cell centered resultant surface at a z_w/ℓ_w location of approximately 30% shown in Figure 4.10.

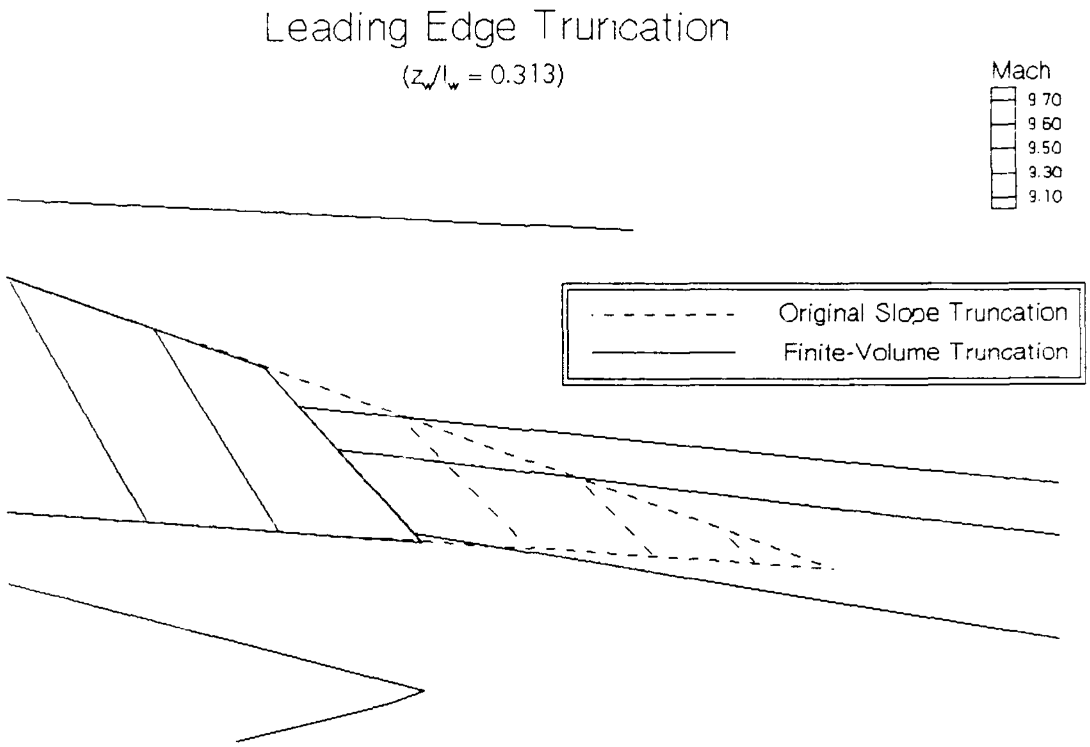

Figure 4.10. Numerical Truncation: Cell-Centered Approximation

This truncation was due to the cell-centered finite volume methodology of the explicit Euler algorithm. The solution model's surface location was an approximation from the first and second surface normal, cell centered planes resolved to the J = 1/2 plane. This computational truncation provides further rationalization for the flow's expansion about the leading edge.

The cusped model maintained the theoretical waverider results for the captured portion of the conical shock wave characterized by the parallel streamlines and increasing surface pressure field.

4.1.3 Grid Refinement

Grid study, Case1r, implemented a similarly spaced grid structure with an increase of approximately 20% in the number of grid cells, as illustrated in Figure 4.11.

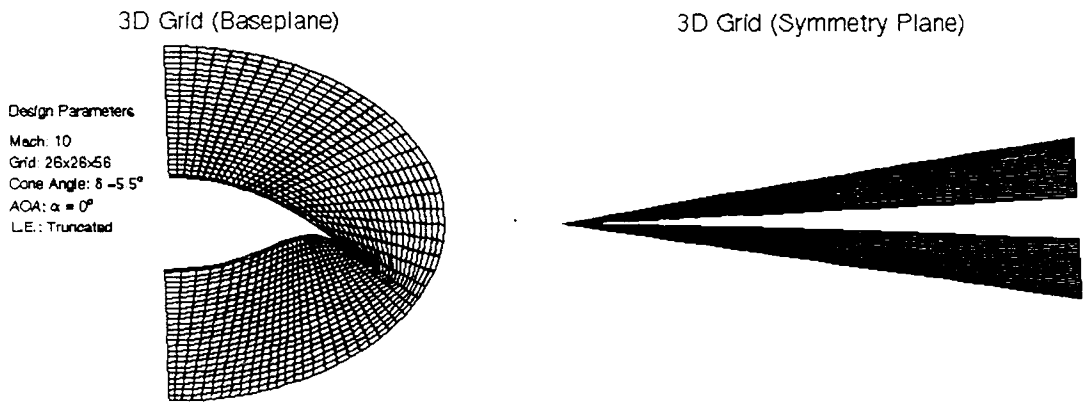

Figure 4.11. Grid Structure: Case1r (26 x 26 x 56)

Convergence of the L_2 norm was attained within 900 iterations, with run times of approximately 90 CPU seconds per 100 iterations. An increase of 50% in CPU time. This increase in computer resources resulted in only a slight increase in L/D as well as c_p.

The conical shock wave was captured at the same scaled grid location for the same range of σ as compared to the baseline case. Refinement in the shock was due to refinement in the grid system as illustrated in Figure 4.12.

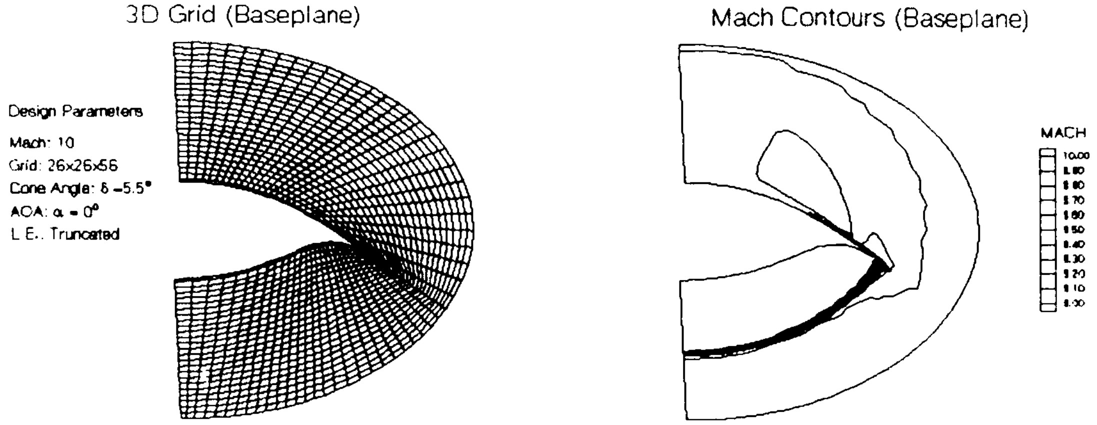

Figure 4.12. Conical Shock Wave Refinement: Case1r

The final grid refinement study, Case2r, involved a 20% increase in refinement of Case1r, while maintaining the evenly spaced grid distribution. The grid structure for Case2r is shown in Figure 4.13.

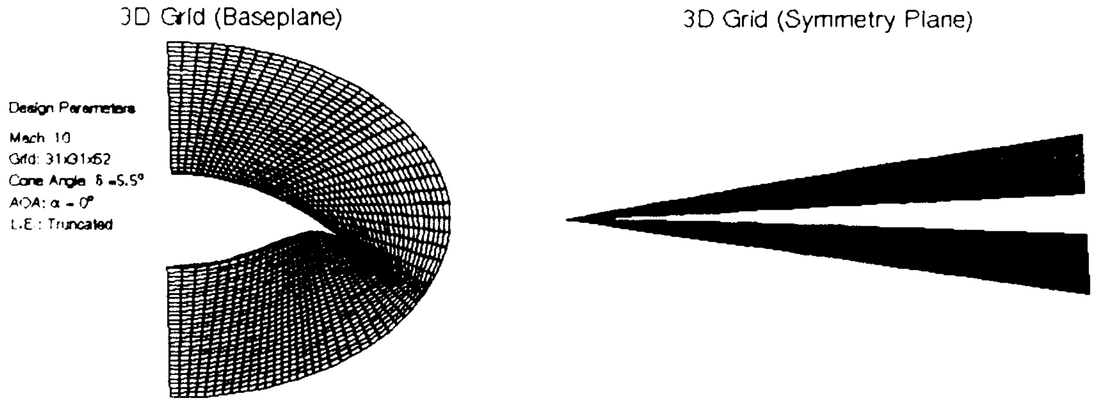

Figure 4.13. Grid Structure: Case2r (31 x 31 x 62)

convergence was attained in 1000 iterations, while expending 140 CPU seconds per 100 iterations, an increase of 130% from the baseline case with less than a 1% refinement in L/D ratio. The convergence history to an L/D value is illustrated in Figure 4.14 for each of the grid refinement cases.

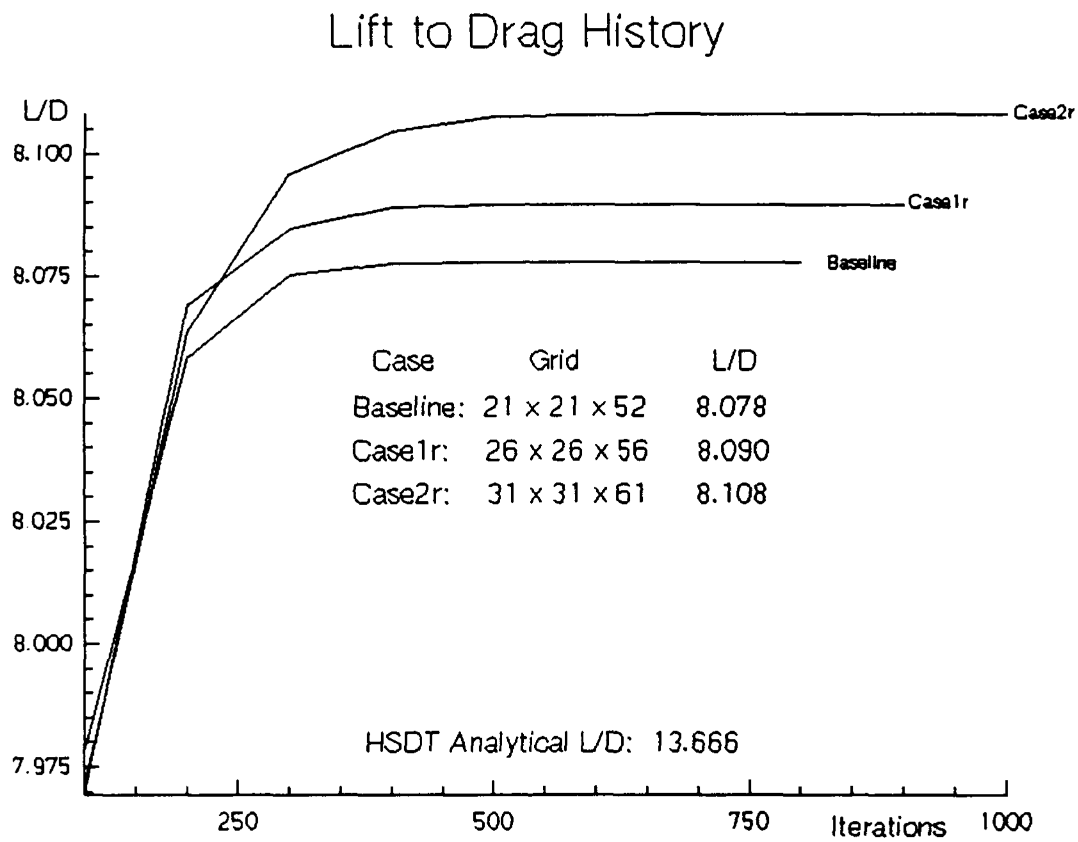

Figure 4.14. L/D History versus Grid Refinement

The same trends in shock wave resolution were noted. The refinement in shock wave development remained proportional to the refinement of the grid as illustrated in Figure 4.15.

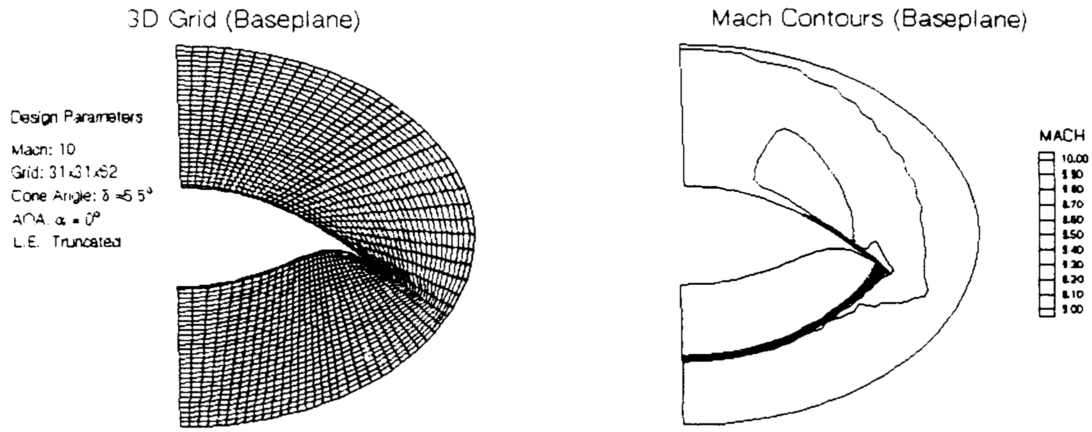

Figure 4.15. Conical Shock Wave Refinement: Case1r

4.2 Off-Design Parametric Studies

An off-design analysis was conducted on two key flight parameters, the freestream Mach number and angle of attack. Investigations in the perturbation of these flight parameters was of interest to verify Rasmussen's statement that (21:1):

> ...experiment has shown that the cone-derived waverider performance is not drastically altered when the on-design conditions are perturbed, and the quality of the flow is not significantly debilitated by interference effects.

Table 4.3 lists the specifications for the flight perturbation studies performed.

Table 4.3
Off-Design Investigations

MACH	α	Grid / Domain
8.0	0^{o}	21x21x52 / baseline
9.0	0^{o}	21x21x52 / baseline
11.0	0^{o}	21x21x52 / baseline
15.0	0^{o}	21x21x52 / baseline
20.0	0^{o}	21x21x52 / baseline
8.0	0^{o}	31x31x62 / expanded
10.0	-5^{o}	31x31x62 / expanded
10.0	-2^{o}	31x31x62 / expanded
10.0	1^{o}	31x31x62 / expanded
10.0	2^{o}	31x31x62 / expanded
10.0	5^{o}	31x31x62 / expanded

The expanded domain referred to for the angle of attack investigation was implemented due to a loss of flow field information when using the baseline elliptic domain. Flow perturbations of below-design Mach numbers and all pitch variations caused a detached shock wave which was artificially forced to freestream values at the outer domain. The expanded domain was first investigated on the low Mach number case and then implemented for all angle of attack cases. The expanded grid employed for the of-design cases is illustrated in Figure 4.16. This grid was produced by expanding the major and minor axes of the outer boundary from the original scaling of 1.5 to 5.0.

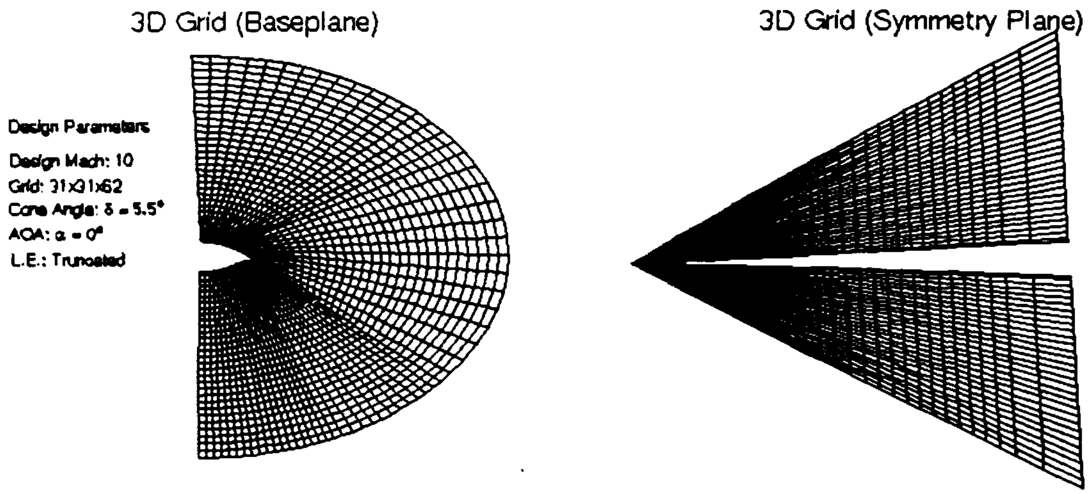

Figure 4.16. Grid Structure: Expanded Domain (31 x 31 x 62)

4.2.1 Off-Design Mach Number

The effects of off-design Mach number yielded no dev ations from the expected results. As Mach number was low·red, the leading edge shock wave detached from the leading edge and a more noticeable bow shock developed. The baseline domain lessened the effects of the low Mach results due to the imposition of freestream boundary conditions at the outer domain. A comparison of the results from the baseline and expanded domain for a Mach number of 8.0 can be seen in Figure 4.17.

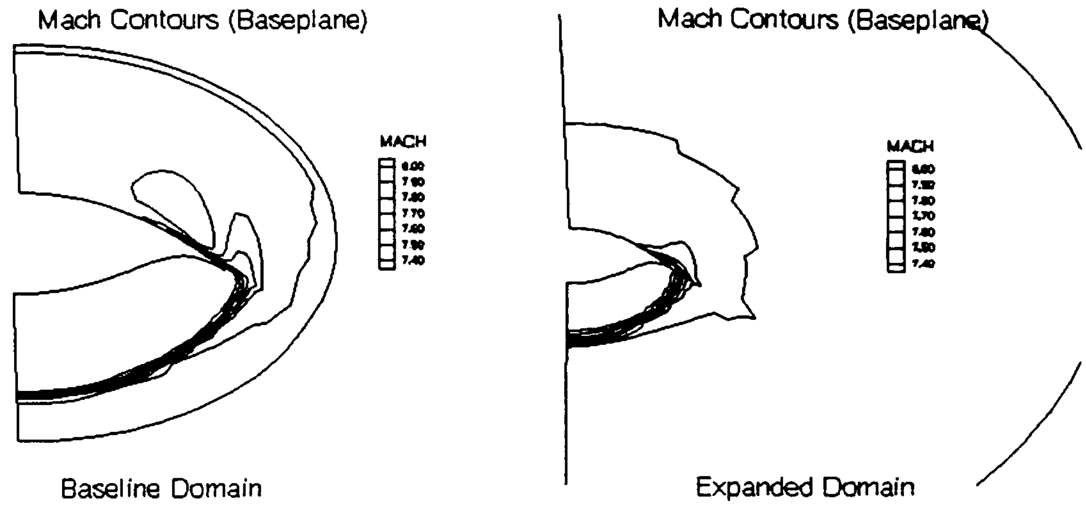

Figure 4.17. Conical Shock Wave Development: Mach 8.0

Investigations on higher than design Mach numbers were not effected by the restrictions of the baseline domain since the higher speed flows were more compressive than the on-design case. The captured shock wave developed on the compression surface, traveling inward as Mach number was increased. This compressive trend is illustrated for the Mach 20.0 case in Figure 4.18.

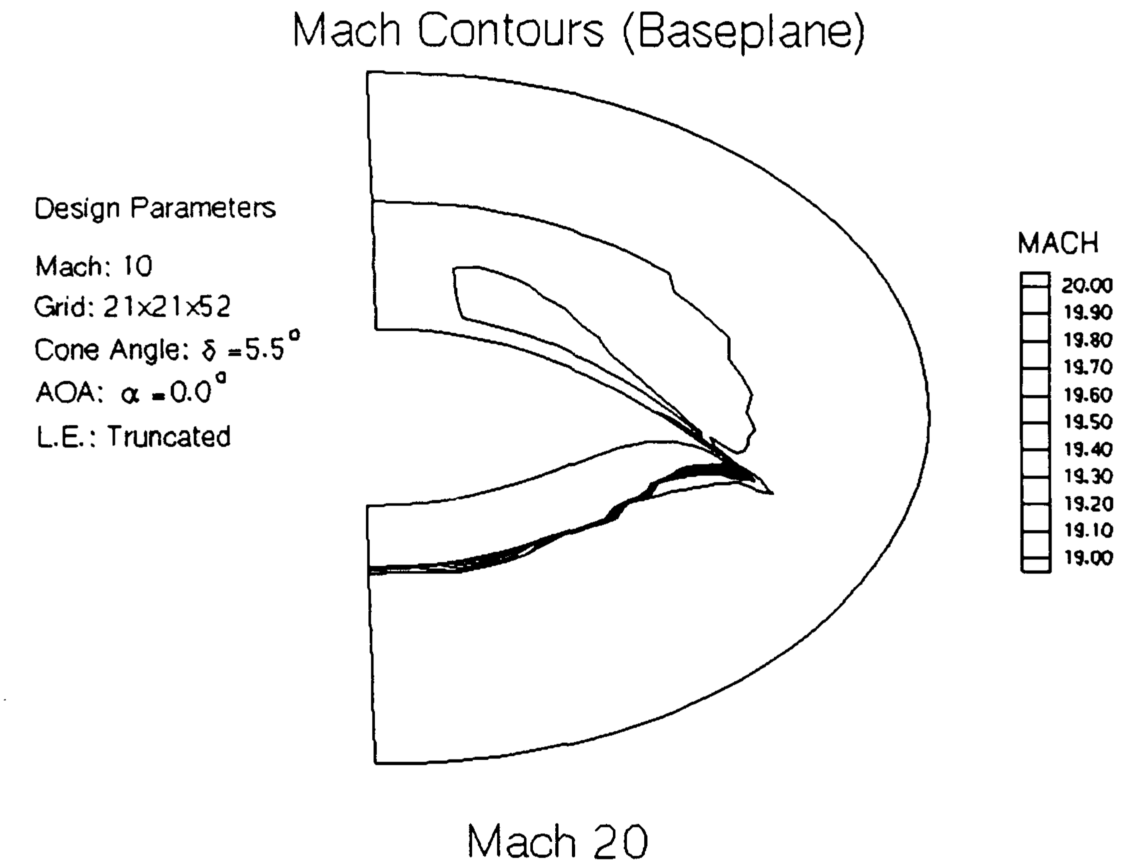

Figure 4.18. Shock Wave Development: Mach 20

The flow pattern characterized by parallel surface streamlines was maintained for all the off-design Mach number investigations validating Rasmussen's earlier statement that the flow field did not suffer debilitating interference effects. This result is illustrated for the Mach 8.0 and 20.0 cases in Figure 4.19, and 4.20 respectively.

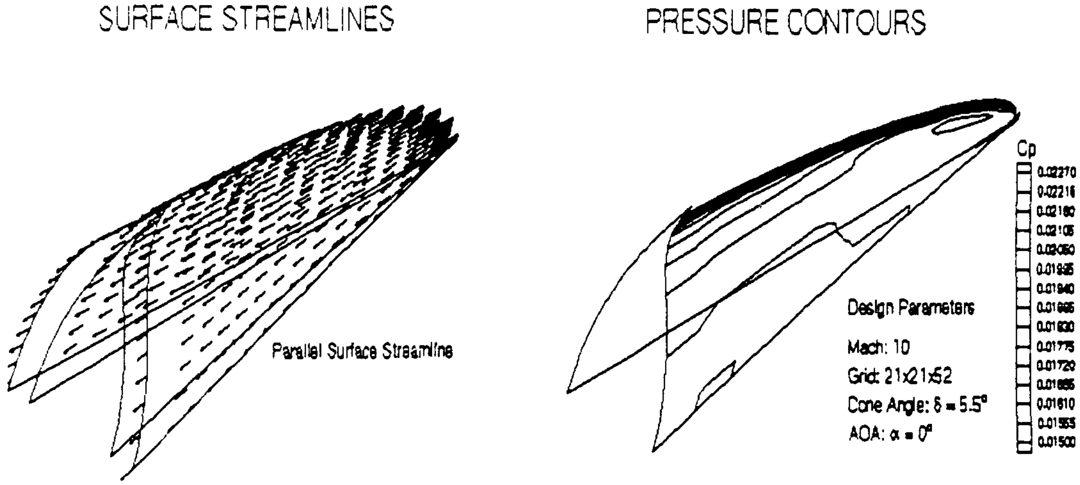

Figure 4.19. Waverider Theoretical Predictions: Mach 8

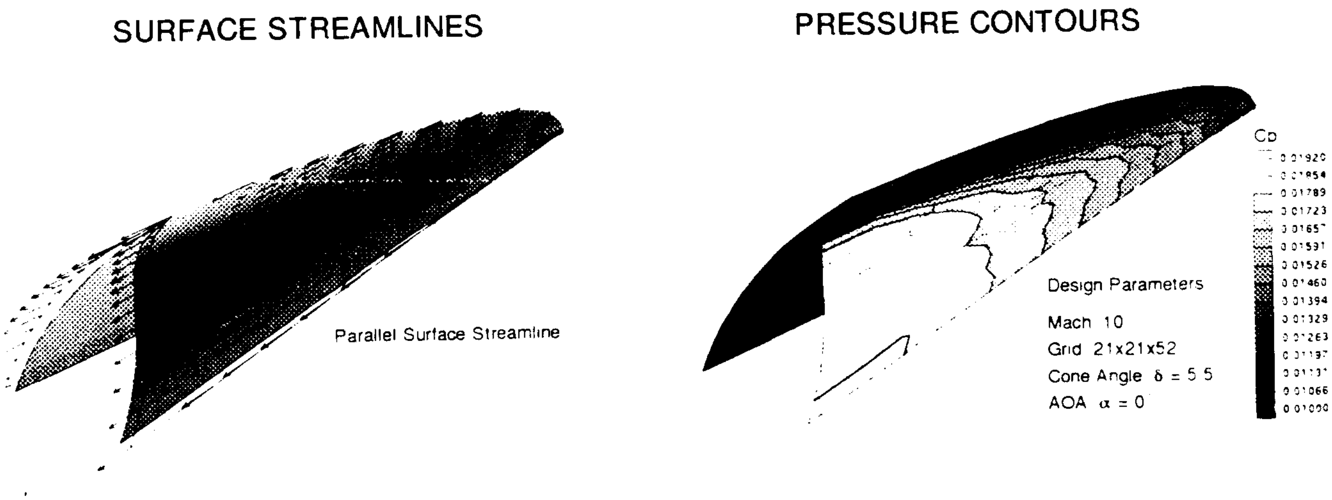

Figure 4.20. Waverider Theoretical Predictions: Mach 20

As illustrated in Figure 4.21, L/D monotomically increased with increased Mach number for the inviscid case.

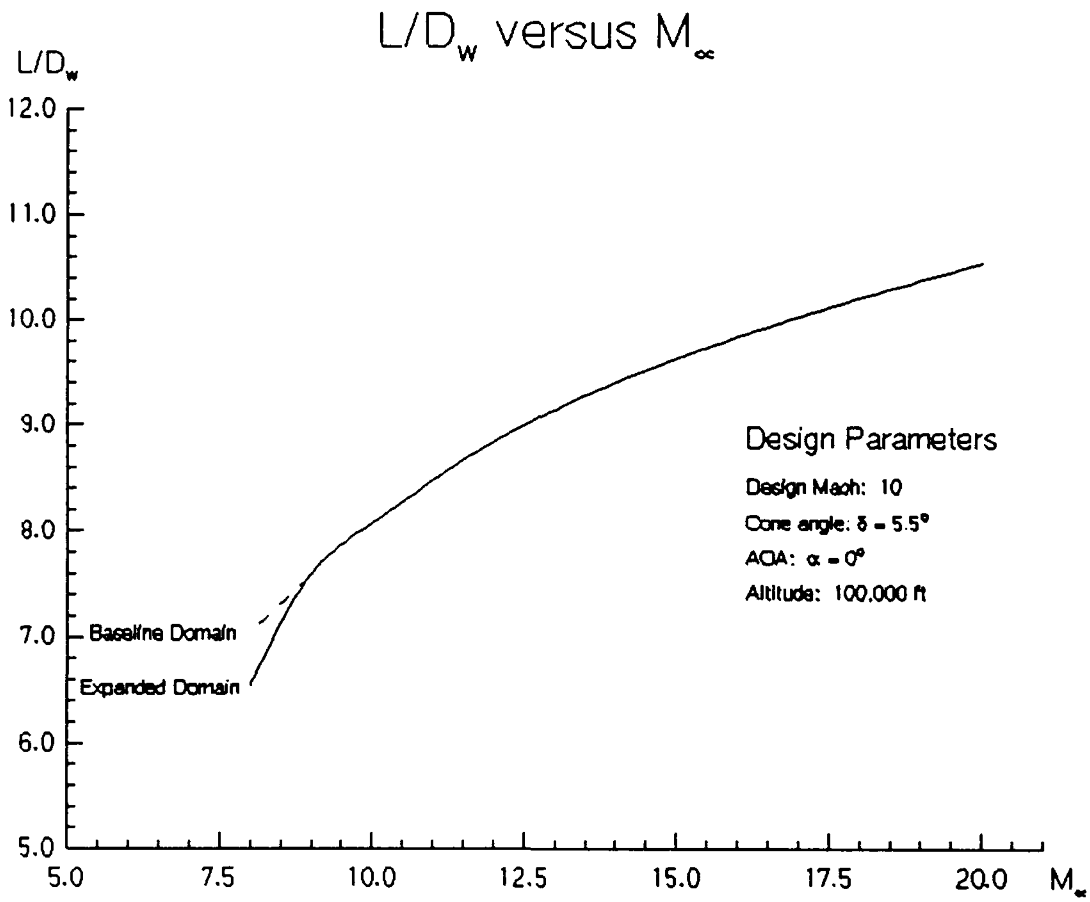

Figure 4.21. L/D versus Mach Number

Table 4.4 lists the numerical results for L/D and maximum surface pressure coefficient for each Mach number case analyzed.

Table 4.4
Off-Design Mach Number Results

MACH	8.00	9.00	11.00	15.00	20.00
L/D	7.023	7.593	8.482	9.639	10.55
C_{Pmax}	.02425	.02225	.02120	.01993	.01925

4.2.2 Off-Design Angle of Attack

An investigation of flow field response to a perturbation in pitch angle, α returned expected results. Streamlines remained parallel on the compression surface with no cross flow mixing present for the range of angles of attack investigated. Figure 4.22 illustrates verification of Rasmussen's claim for an angle of attack of 5^o.

Large losses in inviscid L/D ratios were realized as pitch angle was perturb from the design point. This trend is well illustrated in Figure 4.23. At a pitch angle of + 5^o, the L/D ratio was reduced by approximately 45% from the on-design results.

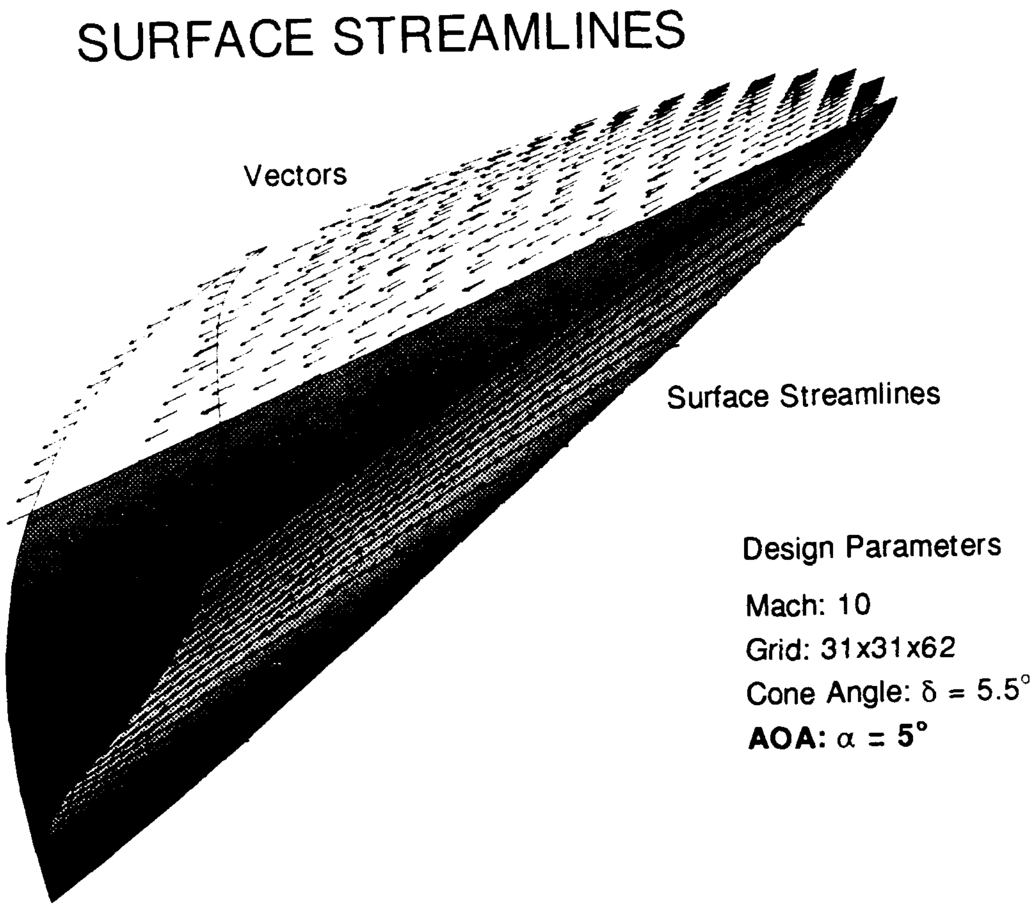

Figure 4.22. Compression Surface Streamlines: $\alpha = 5^{o}$

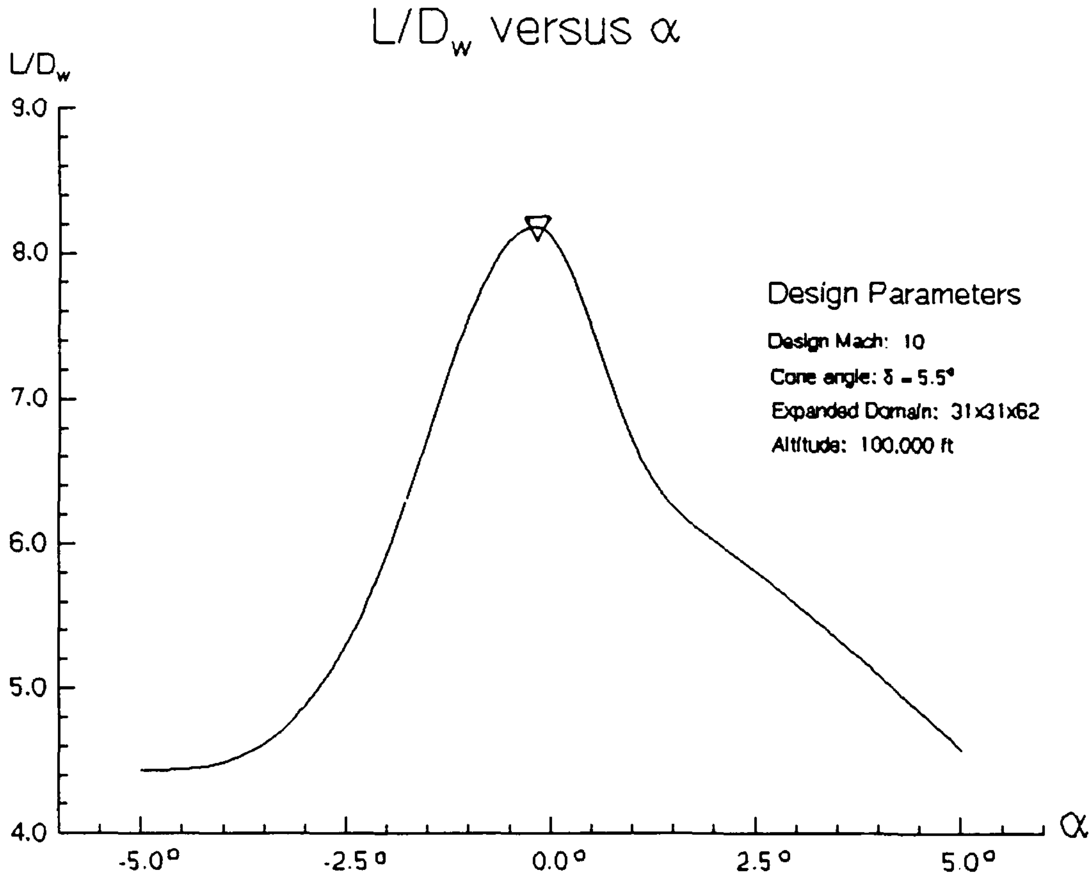

Figure 4.23. L/D versus Angle of Attack

The waverider's optimization at zero angle of attack for maximum L/D is made evident in Figure 4.22. The scaling of the elliptic domain is suspect for a lack of a stronger detached shock wave for the higher values of pitch angle. This is illustrated for the $\alpha = 5^{\circ}$ case in Figure 4.24.

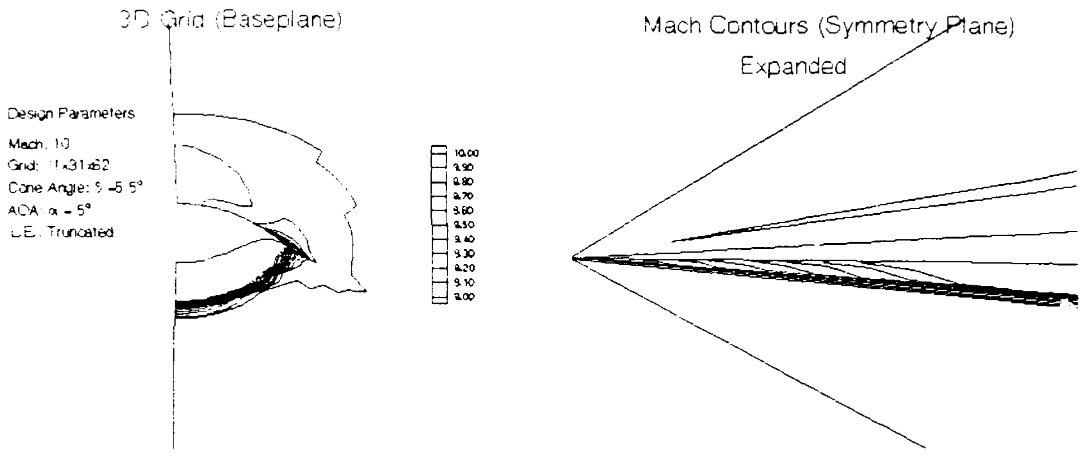

Figure 4.24. Conical Shock Wave Development: $\alpha = 5^{\circ}$

A fully developed bow shock is never realized for the off-design investigations due to the scaling criteria applied to the model. The scaled grid is reduced to a sharp conical section at the nose which enforces a freestream condition in region where shock detachment would be expected for a blunt hypersonic body.

V. Theoretical Analysis

Analysis of the numerical data for the on-design investigations was based on the lift and drag quadratures developed by Rasmussen (19:6-7), as applied to the analytical solution for an on-design waverider configuration described in Table 5.1.

Table 5.1
On-Design Numerical Results

MACH	α	δ	ϕ_t	L/D_w	C_L	C_{Dw}
10.0	0°	5.5°	50°	8.078	.0127	.00157

A synopsis of the development of the lift and drag quadratures is provided in Section 5.1, followed by a comparison of computed data with inviscid analytical results in Section 5.2.

5.1 Lift and Drag Quadratures

The analytical formulation of the lift and drag force components of the waverider was determined by integrating the pressure field over the shock layer on the compression surface by means of the momentum integral theorem (19:21-22). Contributions from the freestream surface, and the freestream portion of the bow shock were assumed to be zero by design. Pressure contributions on the baseplane are ignored from the assumption that $P_b = P_\infty$. The remaining components of lift and wave drag are computed through the use of HSDT by (19:6-7):

$$L = q_\infty \ell^2 \frac{4\delta^3\sigma^3}{\sigma^2 - 1} \int_0^{\phi_l} \left[1 - \frac{R_{cb}}{\sigma^2}\right] \cos\phi \, d\phi$$

$$D_w = q_\infty \ell^2 \frac{\delta^4\sigma^2}{\sigma^2 - 1} \int_0^{\phi_l} \left[1 - \frac{R_{cb}}{\sigma^2} - \ln\left(\frac{R_{cb}}{\sigma^2}\right)\right] d\phi \qquad (5.1)$$

The theoretical analysis is based on the compression surface only. Rasmussen's lift to drag ratio was determined from the equation:

$$L/D = \frac{L}{D_w + D_f}$$

$$L = q_\infty c_L S_p \qquad (5.2)$$

$$D_w = q_\infty c_D S_p$$

The skin friction drag was approximated from an average friction coefficient c_f where:

$$D_f = q_\infty c_f S_w \qquad (5.3)$$

Where S_P is the waverider planform area and S_W is the waverider wetted surface area. The analytic on-design results are listed in Table 5.2.

Table 5.2
On-Design Analytical Results

MACH	α	δ	ϕ_ℓ	L/D_w	C_L	C_{Dw}
10.0	0°	5.5°	50°	13.666	.0214	.00156

The lift to wave drag ratio, L/D_w, was calculated for comparison to the inviscid computed results. Wave drag was removed from the total drag coefficient (21:9):

$$C_{D_w} = C_D - \left(\frac{S_w}{S_p}\right) C_f \qquad \left(\frac{S_w}{S_p}\right)_{design} = 0.487 \tag{5.4}$$

5.2 Analysis of Numerical Data

Initial results for the on-design investigations showed that L/D_w asymptotically approached a value of 8.11, far below the theoretical value of 13.666. This deviation in L/D_W results prompted another numerical investigation based on the theoretical methodology. For this analysis, the Euler code was run on the standard baseline model with calculation of lift and wave drag restricted to the compression surface only. This was equivalent to assuming a perfectly designed freestream surface. Computed results were very favorable, with less the 0.25% error between the numerical solution and theory. Table 5.3 shows the improvement in theoretical agreement due to a perfectly modeled freestream surface.

Table 5.3
Analytical versus Numerical
Results

CASE	MACH	L/D_w	ERROR
ANALYTIC	10.0	13.666	
NUMERICAL Compression	10.0	13.633	0.245%
NUMERICAL Baseline	10.0	8.078	40.89%

These results illustrate that the freestream surface contributions to lift neglects a major phenomena of the physical flow field. Losses in lift due to the bluntness of the leading edge accounts for nearly 40% of the loss when compared to theory. The losses can be pinpointed to the two areas alluded to in Section 4.1.2: truncation approximations at the nose and leading edge. The bluntness applied to the nose region of the model is a physical approximation not considered in theory. This region experiences a small but finite detached normal shock which produces high pressure gradients. The flow attempts to expand around the nose to freestream, but this value is never attained except in the Newtonian limit. This expansion region, with its associated pressure losses, is illustrated in Figure 5.1.

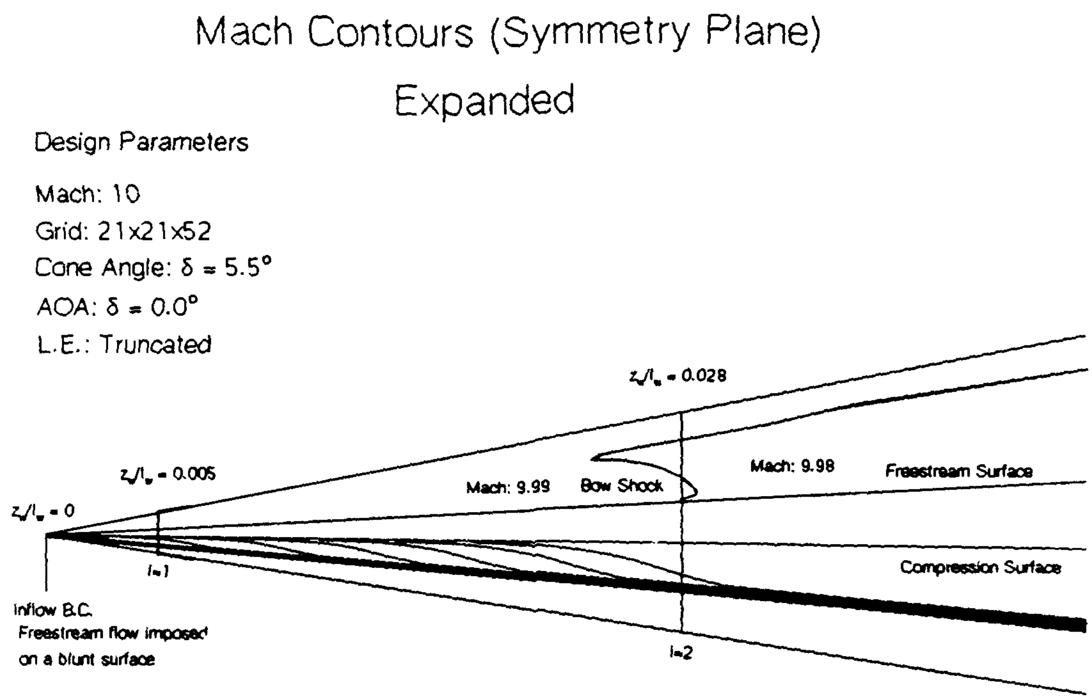

Figure 5.1. Flow Expansion about a Blunt Nose Region

The truncation of the leading edge is also not covered in the analytical evaluations, but has computational as well as physical significance. The truncation allows for flow expansion from the compression surface to the freestream surface, decreasing the pure compressive lift effects of the theoretical design as illustrated in Figure 5.2.

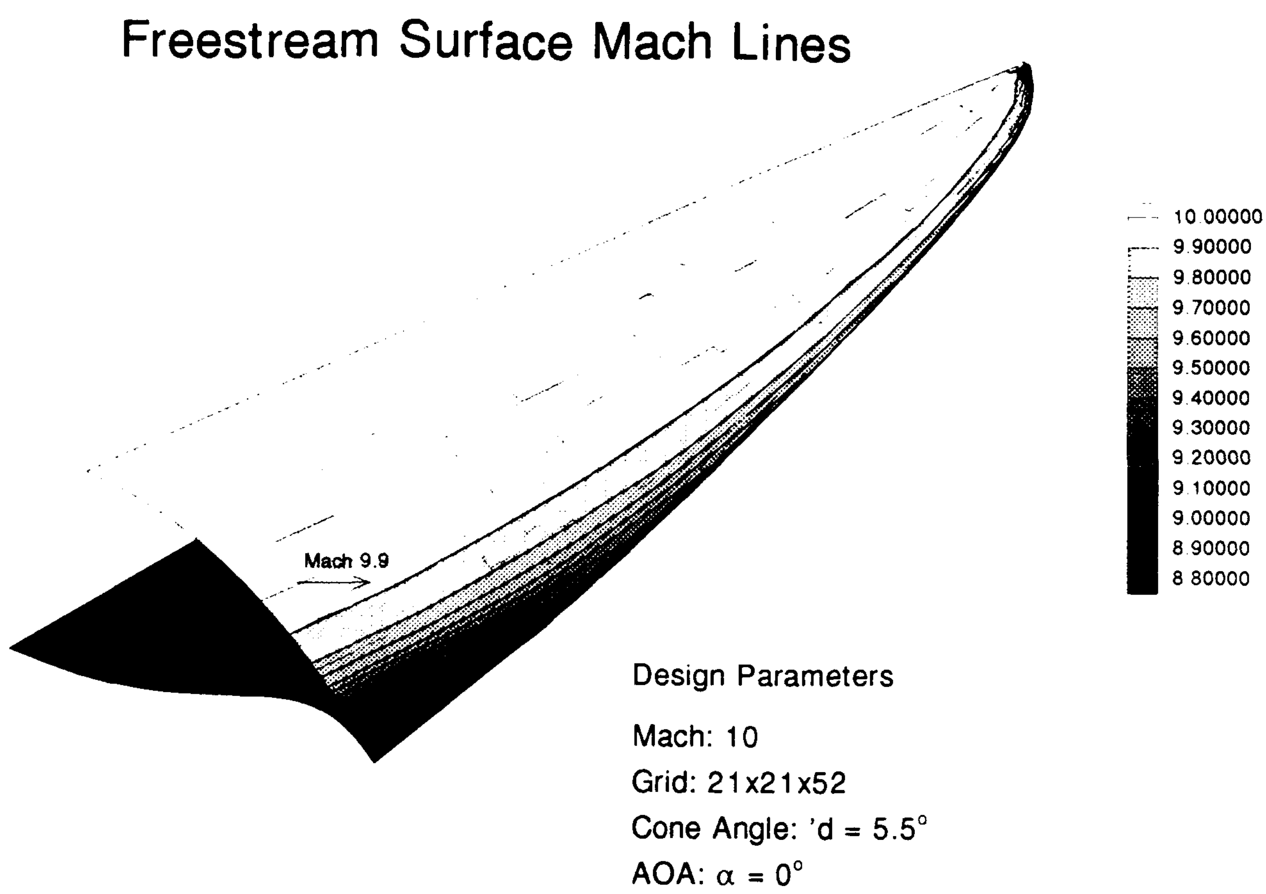

Figure 5.2. Flow Expansion to the Freestream Surface

The problem of flow expansion about the nose of the waverider was alleviated in a similar study conducted by Müller et al (17). The freestream inflow boundary condition was replaced by imposing conical shock conditions at the initial numerical plane. This application of the inflow boundary condition proved very useful, providing baseline L/D results within 15% of analytic inviscid design. This formulation of the boundary condition would not prove very useful for the unified Euler or Navier Stokes solvers.

VI. CONCLUSIONS and RECOMMENDATIONS

6.1 Conclusions

The inviscid, hypersonic flow over a conically derived waverider body at zero angle of attack was studied using Ohio State's SuperComputer Center's Cray YMP/864 supercomputer. Four on-design flight profiles were numerically modeled to determine the explicit Euler algorithm's ability to capture expected HSDT theoretical waverider results. After satisfactory Euler solutions were achieved, comparisons were made to Rasmussen's analytical results for the lift and drag quadratures of the waverider (19). Initial discrepancies prompted another on-design investigation which more exactly modeled the analytic methodology. Near perfect alignment with the analytical results illustrated the effects of the truncated computational model compared to the theoretical results. Two parametric investigations were conducted on the off-design flight characteristics of the waverider. Freestream perturbations were analyzed for off-design Mach number and angle of attack. Results agreed well with HSDT waverider theory as stated by Rasmussen (21:1).

Overall results showed that a waverider body could be modeled utilizing an algebraic O-grid for solution with an explicit, Roe flux-splitting algorithm (6). The use of a finite volume methodology enhanced stability yet deviated from theory due to waverider leading edge truncation. The baseline model returned expected results of parallel streamlines through the conical shock wave, with fair shock attachment at the leading edge. The flow expansion about the waverider leading edge illustrated possible physical penalties to theoretical waverider performance. The following conclusions were determined in light of the objectives listed in Chapter I.

(1) The generation of the baseline parabolic waverider body coordinates followed the analytical derivations of Rasmussen (19) and Martin (16) well with few approximations.

(2) The development of a suitable three-dimensional grid evolved into a significant research effort. The use of an algebraic model provided a robust, generic baseline from which future optimization investigation can be initiated. The use of an O-grid allowed for the capture of flow expansion from the compression surface over the leading edge. The implementation of freestream condition on a small, but finite initial plane illustrated the effects of flow stagnation and expansion over a blunt body, resulting in significant losses in the lift capability of the optimized design.

(3) The three-dimensional explicit Euler algorithm performed well, with all the credit attributed to the independent efforts of Gaitonde (6) in code development and restructuring for waverider applications. The code's finite volume approach resulted in code stability and robustness in regions of high cell skewness. The code produced expected results in conjunction with waverider theory, with deviations attributable to numerical modeling procedures.

(4) Numerical validation of the analytical results was realized through the application of the theoretical methodology. Near exact correlation to analytical results was only obtained by investigating compression surface effects only, otherwise assuming a perfectly designed freestream surface. Implementation of the full body to numerical analysis illustrated losses in lift due to a numerical modeling of the theoretical limit of a cusped leading edge.

(5) The off-design parametric evaluations validated the stability of the waverider's compressive, smooth streamline design for the range of off-design points investigated. The benefits of the waverider's optimization for L/D is strained due to losses incurred at off-design points expected in any normal flight profile.

6.2 Recommendations

The present research thesis provided an excellent baseline from which further waverider research could be initiated. The following recommendations are listed according to the objectives stated in Chapter I.

(1) Expansion of the baseline parabolic waverider code should be performed to cover the general case of the full four term, sixth order polynomial devised by Rasmussen (19). An investigation into leading edge rounding from the basic slope truncation is desired for implementing viscous and real gas investigations of the waverider design. Freestream surfaces with slight expansion angles should be investigated to determine their effects in recovering the pressure losses associated with numerical truncated body shapes in the present research.

(2) A grid optimization study applied to the present model in the areas of surface orthoganility, cell clustering, and outer domain refinement would be of interest in improving the flow field capturing cabability of the present design. A key area in outer domain refinement would be to develop a rounded inflow plane as a replacement of the conical apex applied in the present research.

(3) Alternate inflow boundary conditions should be

applied to the explicit algorithm's current design to more effectively model the expected freestream surface results. One such method would be to impose conical conditions at the initial apex plane.

(4) The Navier Stokes equations should be applied. Initial investigations should be conducted on the baseline model. The purpose would be to determine further flow field interaction phenomena with the introduction of viscous terms.

BIBLIOGRAPHY

1. Anderson, Dale A., et al. Computational Fluid Mechanics and Heat Transfer. New York: Hemisphere Publishing Corporation, 1984.

2. Anderson, John D. Fundamentals of Aerodynamics. New York: McGraw-Hill Publishing Company, 1984.

3. Anderson, J.D., et al. "Hypersonic Waveriders for High Altitude Applications," AIAA Paper 91-0530, AIAA 29th Aerospace Sciences Meeting, Reno, NV, January 1991.

4. Anderson, John D. Modern Compressible Flow With Historical Perspective (Second Edition). New York: McGraw-Hil Publishing Company, 1990.

5. Beran, P. Class handout distributed in Aero 752, Computational Fluid Dynamics. School of Engineering, Air Force Institute of Technology (AU), Wright-Patterson AFB OH, May 1991.

6. Beran, P. Class handout distributed in Aero 753, Advanced Computational Fluid Dynamics. School of Engineering, Air Force Institute of Technology (AU), Wright-Patterson AFB OH, September 1991.

7. Bowcutt, Kevin G. et al. "Viscous Optimized Hypersonic Waveriders," AIAA Paper 87-0272, AIAA 25th Aerospace Sciences Meeting, Reno, NV, January 1987.

8. Eggers, Alfred J., et al. "Hypersonic Waverider Configurations From the 1950's to the 1990's," Proceedings of the 1st International Hypersonic Waverider Symposium. 1-82. University of Maryland, College Park, MD. October, 1990.

9. Emanuel, George. Gasdynamics: Theory and Applications. edited by J. S. Przemieniecki. American Institute of Aeronautics and Astronautics, Inc., New York, 1986.

10. Gaitonde, Datta. "Computation of Viscous Shock/Shock Hypersonic Interactions with an Implicit Flux Split Scheme," 7 September 1989-7 September 1990. Contract F-33615-88-C-2908. Wright-Patterson AFB OH: Flight Dynamics Laboratory, WL/FIMM, December 1990.

11. Gaitonde, Datta. "The Computation of High Speed Flows Past Blunt Bodies and Compression Corners with Flux-Split Methods." To be published as a Wright Laboratory TR.

12. Hoffman, Klause A. Computational Fluid Dynamics For Engineers. Engineering Education System, Austin Texas, 1989.

13. Jischke, M.C., et al. "Experimental Results fo Forces and Moments on Cone-Derived Waveriders in Mach-Number Range 3-5," AIAA Paper 81-0149, AIAA 19th Aerospace Sciences Meeting, St. Louis, January 1981.

14. Kroll, N., et al. "A Systematic Comparative Study of Several High Resolution Schemes for Complex Problems in High Speed Flows," AIAA Paper 91-0636, AIAA 29th Aerospace Sciences Meeting, Reno, NV, January 1991.

15. Küchemann, Dietrich. The Aerodynamic Design Of Aircraft. New York: Pergamon Press, 1978.

16. Martin, William P. Hypersonic Waverider Configurations For Trans-Atmospheric Vehicles. MS Thesis, AFIT/CI/CIA/89-105. School of Aerospace and Mechanical Engineering, University of Oklahoma, Norman OK, 1989 (AD-A217925).

17. Müller, B. et al. "Simulation of Hypersonic Waverider Flow," Proceeding of the 1st International Hypersonic Waverider Symposium. 1-15. University of Maryland, College Park, MD, October 1990.

18. Nonweiler, Terence R.F. "The Waverider wing in Retrospect and Prospect - A Personalised View," Proceedings of the 1st International Hypersonic Waverider Symposium. 1-20. University of Maryland, College Park, MD, October 1990.

19. Rasmussen, Maurice L. "Analysis of Cone-Derived Waveriders By Hypersonic Small-Disturbance Theory," Proceeding of the 1st International Hypersonic Waverider Symposium. 1-46. University of Maryland, College Park, MD, October 1990.

20. Rasmussen, Maurice L. "Experiments on a Slender Waverider Configuration with and without an Inlet," 1 October 1982-10 September 1983. Contract F08635-80-K-0304. Eglin AFB, FL: Air Force Armament Laboratory, April 1986 (AD-B102543).

21. Rasmussen, Maurice L. "On Waverider Shapes Applied To Aero-Space Plane Forebody Configurations," AIAA Paper 87-2550, AIAA 25th Aerospace Sciences Meeting, Reno NV, January 1987.

22. Roe, P.L., "Theory of Waveriders," in Aerodynamic Problems of Hypersonic Vehicles, edited by K. Enkenhus, J.F. Wendt, and R.C. Pankhurst, AGARD LS-42,1972.

23. Steger, J.L. and R.F. Warming. "Flux Vector Splitting Gasdynamics Equations with Application to Finite-Difference Methods," Journal of Computational Physics, 40: 263-293 (April 1980).

24. Towend, L.H., "Research and Design for Lifting Reentry," Progress in Aerospace Sciences, 18: 1-80 (1979).

Appendix A: Program WVRIDR.F Source Code

General Information

The purpose of this appendix is to provide the baseline source code for the developement of a parabolic-top waverider surface formulation adapted to a scaled elliptic outer domain three-dimensional O-grid system. This code is provided as a baseline for further research in the area of hypersonic waverider applications.

Key Terms

The following list of key variables are used in the input subroutine INDAT

1.	DATA	Name of output file
2.	MACH	Freestream design Mach Number
3.	D	Design cone half angle
4.	l	Generating cone length
5.	MCAP	# of radial increments per surface
6.	NCAP	# of planar cross sections
7.	BNDS	# of planes from surface to domain
8.	A0,A1,A2	Geometric packing parameters

Basic output file are provided for each of the specific grid refinements analyzed following the code listing.

```fortran
      PROGRAM WVRIDR

C     PRODUCES MULTIPLE 2-D CROSSPLANE SURFACES OF A
C     PARABOLIC HYPERSONIC WAVERIDER

      IMPLICIT REAL*8 (A-H,O-Z)
      INTEGER MCAP,NCAP,INCR,BNDS
      REAL*8   MACH,G,D,PHIL,l,SIGMA,Ro,Ao,XSIG,YSIG,PI,
     *        lw,rz,Rin(950),Rcb(950),RAD,ZovL(35),A(35),
     *        X(35,35,65),Y(35,35,65),Z(35,35,65),
     *        Xo(35,35,65),Yo(35,35,65),A0,A1,A2

      CHARACTER DATA*15
      COMMON MCAP,NCAP,PI,INCR,BNDS,PHIL

C     SET CONSTANTS

      PI = 4.d0*DATAN(1.d0)
      RAD = PI/180.

C     CONSTANTS WHICH EFFECT THE GEOMETRY OF THE WAVERIDER
      MACH = 10.0
      D = 5.5 * RAD
      PHIL = 50.0 * RAD
      l = 10.41741446
      TYPE = 0

C     BASIC CALCULATIONS NEEDED FOR WAVERIDER CROSSPLANE
C     DEVELOPMENT

      MCAP = 25
      NCAP = 20
      BNDS = 20

      A0 = .002
      A1 = .005
      A2 = .045

      G = 1.4

      DATA = 'basepl'

C     GET INPUT DATA
C     CALL INDAT(DATA,MACH,D,l,A0,A1,A2)

C     write(*,*) mach,d,phil,type,l,mcap,ncap,bnds,a0,a1,a2

C     d = d *rad
C     phil =phil*rad
```

```
      INCR = (2*MCAP) + 1

C     OUTPUT = 'baseplane'

      SIGMA = ((G+1.0)/2.0 +1.0/((MACH*D)**2))**0.5

      XSIG = SIGMA*COS(PHIL)
      YSIG = SIGMA*SIN(PHIL)

C     VALUE OF TYPE DEFINES TYPE OF PARABOLIC WAVERIDER.
C     DEFAULT IS SET TO TANGENT PARABOLIC

      IF (TYPE.EQ.0) THEN
        Ro = XSIG/2.0
        Ao = Ro/(YSIG)**2
       ELSE
        Ro = 0.75*XSIG
        Ao = 0.25*XSIG/(YSIG)**2
      END IF

      lw = l*(1.0 - Ro/SIGMA)
      rz = l*(Ro/SIGMA)


C     COMPUTE WAVERIDER GEOMETRY
      CALL WAVEBODY(Ro,Ao,l,D,SIGMA,rz,Rin,Rcb,ZovL,
     *              X,Y,Z,A0,A1)

      CALL LEADEDG(X,Y)

      CALL GRIDBNDS(X,Y,Rin,Xo,Yo,A,ZovL)

      CALL GRIDLINE(Xo,Yo,A,X,Y,Z,A2)

C     CALL OUTDAT TO WRITE TO A DATA FILE
      CALL OUTDAT(Rin,Rcb,lw,l,MACH,D,ZovL,
     *            X,Y,Z,DATA)

      END
C     END OF MAIN PROGRAM

      SUBROUTINE WAVEBODY(Ro,A,l,D,SIGMA,rz,Rin,Rcb,
     *                    ZovL,X,Y,Z,A0,A1)

C     WAVEBODY DEFINES THE X,Y,& Z COORDINATES OF
C     CROSSPLANES OF THE WAVERIDER CONFIGURATION

      IMPLICIT REAL*8 (A-H,O-Z)
      INTEGER I,J,K,INCR,M,N,BNDS
      REAL*8  PHI(35),PHIZ(35,35),Rin(950),rz,rs(35),
```

```
     *        ZovL(35),Rcb(950),Xin(35,35),Yin(35,35),
     *        Zin(35,35),Xcb(35,35),Ycb(35,35),Zcb(35,35),A,
     *        SIGMA,test,X(NCAP,BNDS,INCR),Y(NCAP,BNDS,INCR),
     *        Z(NCAP,BNDS,INCR),D,DELTA(35),A1,PLANE(35),A0,
     *        Ro,l,PROG

      COMMON MCAP,NCAP,PI,INCR,BNDS,PHIL

C     SET INITIAL VALUE OF PHI TO COINCIDE WITH THE
C     NUMBER OF CROSSPLANES: (PHIL/RAD)/NCAP

      PHI(1) = 7.0*PI/180.
      PROG = PHIL-PHI(1)
       CALL GEOM(PROG,A0,NCAP-1,PLANE)
        DO N = 2,NCAP
         PHI(N) = PHI(N-1) + PLANE(NCAP+1-N)
        END DO
      PHI(NCAP) = PHIL

        scale = l*D

      DO 10 I = 1,NCAP

C     CORRECT FOR ERRORS IN MACHINE ZERO

      test = ((COS(PHI(I)))**2-4.0*Ro
     *             *A*(SIN(PHI(I)))**2)

      IF(test.LE.0.0)THEN
        test = 0.0
      END IF

      rs(I) = (l/SIGMA)*(2.*Ro)/(COS(PHI(I))+(test)**0.5)

      ZovL(I) = (rs(I)-rz)/(l*(1.0-Ro/SIGMA))

C     A1 DETERMINES THE INITIAL PACKING INCREMENT OF BODY
C     POINTS FROM THE LEADING EDGE OUTWARD.

C     COMPUTE THE PHI INCREMENTS FOR BODY POINT GENERATION
        STEP = PHI(I)
      CALL GEOM (STEP,A1,MCAP,DELTA)

         PHIZ(I,1) = 0.0
      DO 15 J = 2,MCAP+1

   15    PHIZ(I,J) = PHIZ(I,J-1) + DELTA(MCAP+2-J)
         PHIZ(I,MCAP+1) = PHI(I)

       DO 20 J = 1,MCAP+1
```

```
          K = (I-1)*(MCAP+1)+J

      Rin(K) = ((2.* Ro)/(COS(PHIZ(I,J))+
     *          ((COS(PHIZ(I,J)))**2
     *          - 4.*Ro*A*(SIN(PHIZ(I,J)))**2)**0.5))

      Rcb(K) = (((ZovL(I)*(1.0-Ro/SIGMA)+Ro/SIGMA)**2 +
     *          (SIGMA**2 - 1.0)*Rin(K)**2/SIGMA**2)**0.5)

C     CALCULATE THE X,Y,& Z VALUES FOR EACH CROSSPLANE.
C      Z IS A CONSTANT FOR EACH CROSSPLANE

      Xin(I,J) = Rin(K)*COS(PHIZ(I,J))
      Yin(I,J) = Rin(K)*SIN(PHIZ(I,J))
      Zin(I,J) = rs(I)

      Xcb(I,J) = Rcb(K)*COS(PHIZ(I,J))
      Ycb(I,J) = Rcb(K)*SIN(PHIZ(I,J))
      Zcb(I,J) = rs(I)

  20  CONTINUE


  10  CONTINUE

C     COMBINE THE X, Y, & Z VALUES OF THE FREESTREAM AND
C     COMPRESSION SURFACES INTO ONE ARRAY

      DO 30 I = 1, NCAP
        DO 40 J = 1,MCAP

         X(I,1,J) = Xin(I,J)*scale
         Y(I,1,J) = Yin(I,J)*scale
         Z(I,1,J) = Zin(I,J)

   40   CONTINUE
   30 CONTINUE

      DO 50 M = 1,NCAP
       DO 60 N = MCAP+1,INCR

         X(M,1,N) = Xcb(M,(INCR+1)-N)*scale
         Y(M,1,N) = Ycb(M,(INCR+1)-N)*scale
         Z(M,1,N) = Zcb(M,(INCR+1)-N)
   60   CONTINUE

   50 CONTINUE

      RETURN
```

```
      END

      SUBROUTINE LEADEDG(X,Y)

C     DEFINES THE LEADING EDGE OF THE WAVERIDER BY FINDING
C     THE INTERSECTION OF THE FREESTREAM AND COMPRESSION
C     SURFACE SLOPES.

      IMPLICIT REAL*8 (A-H,O-Z)
      INTEGER I,BNDS
      REAL*8 Mfre,Mcom,Bfre,Bcom,X(NCAP,BNDS,INCR),
     *       Y(NCAP,BNDS,INCR),Xle,Yle

      COMMON MCAP,NCAP,PI,INCR,BNDS,PHIL

      DO I = 1,NCAP

      Mfre = (Y(I,1,MCAP)-Y(I,1,MCAP-1))/(X(I,1,MCAP)-
     *        X(I,1,MCAP-1))

      Mcom = (Y(I,1,MCAP+2)-Y(I,1,MCAP+3))/(X(I,1,MCAP+2)-
     *        X(I,1,MCAP+3))

      Bfre = Y(I,1,MCAP) - Mfre*X(I,1,MCAP)

      Bcom = Y(I,1,MCAP+2) - Mcom*X(I,1,MCAP+2)

      Xle = (Bcom - Bfre)/(Mfre - Mcom)

      Yle = Mfre*Xle + Bfre

      X(I,1,MCAP+1) = Xle
      Y(I,1,MCAP+1) = Yle

      END DO
      RETURN
      END


      SUBROUTINE GRIDBNDS(X,Y,Rin,Xo,Yo,A,ZovL)

C     GRIDBNDS DEFINES THE OUTER BOUNDARY ELLIPSE SCALED TO
C     EACH CROSS-SECTION

      IMPLICIT REAL*8 (A-H,O-Z)
      INTEGER I,K,BNDS
      REAL*8 Rin(950),Xctr,Yle,SLOPE,B,R,S,T,
     *       SIGZ,X(NCAP,BNDS,INCR),Y(NCAP,BNDS,INCR),
     *       A(NCAP),THETAtan,THETA(65),chgyt,chgxt,chgyb,
     *       chgxb,Xo(NCAP,BNDS,INCR),Yo(NCAP,BNDS,INCR),
```

```
     *       slpt,slpb,ZovL(35)

      COMMON MCAP,NCAP,PI,INCR,BNDS,PHIL

C     COMPUTE THE TANGENT POINT AND ANGLE FROM THE LEADING
C     EDGE TO THE ELLIPSE


      DO 10 I = 1,NCAP

C       DETERMINE KEY GEOMETRY LOCATIONS ON THE WAVERIDER
C       SURFACE

     Xctr = (X(I,1,INCR)-X(I,1,1))/2. + X(I,1,1)

     Yle = Y(I,1,MCAP+1)

     SIGZ = Rin(I*(MCAP+1))

        chgyt = Y(I,1,MCAP+1)-Y(I,1,MCAP)
        chgyb = Y(I,1,MCAP+1)-Y(I,1,MCAP+2)

        chgxt = X(I,1,MCAP+1)-X(I,1,MCAP)
        chgxb = X(I,1,MCAP+1)-X(I,1,MCAP+2)

        slpt = chgyt/chgxt
        slpb = chgyb/chgxb

      IF(ZovL(I).GT..25) THEN
        SLOPE = (slpt+slpb)/2.d0
      ELSEIF (ZovL(I).LT..10) THEN
        SLOPE = 3.0*slpt
      ELSE
        SLOPE = 2.0*slpt
      END IF
C       SLOPE = slpb

        Yint = Y(I,1,MCAP+1) - SLOPE*X(I,1,MCAP+1)


C       DETERMINE THE MAJOR AND MINOR AXES OF THE OUTER
C       BOUNDARY ELLIPSE BASED ON SURFACE LENGTHS

     A(I) = 1.50*(SIGZ-Xctr)
     B = 1.50*Yle

C       ESTABLISH AND SOLVE QUADRATIC EQUATION FOR THE
C       INTERSECTION OF THE OUTER BOUNDARY AND BODY LE VALUE

     R = B**2 + SLOPE**2*A(I)**2
```

```
      S = -(2.*B**2*Xctr) + 2.*A(I)**2*SLOPE*Yint
      T = B**2*(Xctr**2-A(I)**2) + A(I)**2*Yint**2


      X(I,BNDS,MCAP+1) = (-S+(S**2-4.*R*T)**0.5)/(2.*R)

      Y(I,BNDS,MCAP+1) = SLOPE*X(I,BNDS,MCAP+1) + Yint

      THETAtan = ASIN(Y(I,BNDS,MCAP+1)/B)

C       MAP THE POINTS ON THE OUTER BOUNDARY WITH MIDPOINT AS
C       REFERENCE.  GENERATE COARSE SPACING AT AND NEAR MAJOR
C       AXES LOCATION

         THETA(1) = PI

        DO 20 K = 2,MCAP-10

         THETA(K) = THETA(K-1) - ((pi-thetatan)/real(MCAP+5))

   20  CONTINUE
         DO K = MCAP-9,MCAP
         THETA(K) = THETA(K-1) - ((pi-thetatan)/real(MCAP-5))
         END DO

          THETA(MCAP+1) = THETAtan

        DO 25 K = MCAP + 2,INCR-15

         THETA(K) = THETA(K-1) - THETAtan/real(MCAP-5)

   25  CONTINUE

         DO K = INCR-14,INCR
         THETA(K) = THETA(K-1) - THETAtan/real(MCAP+5)
         END DO
         THETA(INCR) = 0.0

       DO 30 L = 1,INCR

        Xo(I,BNDS,L) = Xctr + A(I)*COS(THETA(L))

        Yo(I,BNDS,L) = B*SIN(THETA(L))


   30  CONTINUE

   10  CONTINUE
       RETURN
       END
```

```
      SUBROUTINE GRIDLINE(Xo,Yo,A,X,Y,Z,A2)

C     GRIDLINE COMPUTES A LINEAR GEOMETRIC PROGRESSION
C     FROM RAYS IMMENATING FROM THE BODY TO THE ELLIPTIC
C     OUTER BOUNDARY FOR A GIVEN X-Y PLANE

      IMPLICIT REAL*8 (A-H,O-Z)
      INTEGER I,K,J,BNDS
      REAL*8 MINWALL,CAPDX,CAPDY,LEN,STEPJ(35),smdx,smdy,
     *       X(NCAP,BNDS,INCR),Y(NCAP,BNDS,INCR),
     *       Z(NCAP,BNDS,INCR),A(NCAP),
     *       Xo(NCAP,BNDS,INCR),Yo(NCAP,BNDS,INCR)

      COMMON MCAP,NCAP,PI,INCR,BNDS,PHIL

      DO 10 I = 1,NCAP

       DO 20 K = 1,INCR

C     COMPUTE LENGTH OF EACH RAY FROM BODY TO OUTER ELLIPSE.
C     COMPUTE GEOMETRIC PROGRESSION FROM THE BODY TO OUTER
C     BOUNDARY IN TERMS OF X,Y, AND Z.

         CAPDX = Xo(I,BNDS,K) - X(I,1,K)

         CAPDY = Yo(I,BNDS,K) - Y(I,1,K)

         LEN = (CAPDX**2 + CAPDY**2)**0.5

C     DETERMINE WALL SPACING FOR EACH PLANAR CUT

         MINWALL = A2*LEN
         CALL GEOM(LEN,MINWALL,MCAP-6,STEPJ)

        DO 30 J = 2,BNDS

          smdx = CAPDX*STEPJ(J-1)/LEN
          smdy = CAPDY*STEPJ(J-1)/LEN

          X(I,J,K)  = X(I,J-1,K)  + smdx
          Y(I,J,K)  = Y(I,J-1,K)  + smdy
          Z(I,J,K)  = Z(I,1,K)

   30   CONTINUE

C     ENFORCE THE VALUE OF THE OUTER ELLIPSE

         X(I,BNDS,K) = Xo(I,BNDS,K)
         Y(I,BNDS,K) = Yo(I,BNDS,K)
```

```
   20    CONTINUE
   10   CONTINUE

        RETURN
        END


        SUBROUTINE OUTDAT(Rin,Rcb,lw,l,MACH,D,ZovL,
       *                  X,Y,Z,OUTPUT)
C       OUTPUT SENDS RESULTS TO AN OUTPUT FILE

        IMPLICIT REAL*8 (A-H,O-Z)
        INTEGER I,J,K,INCR,BNDS
        REAL*8 X(NCAP,BNDS,INCR),Y(NCAP,BNDS,INCR),
       *       Z(NCAP,BNDS,INCR),lw,l,MACH,D,
       *       Rin(950),Rcb(950),ZovL(35)
        CHARACTER OUTPUT*15
        COMMON MCAP,NCAP,PI,INCR,BNDS,PHIL

C       SET OUTPUT FILE SUFFIX
        OUTPUT(INDEX(OUTPUT,' '):) = '.dat'

C       OPEN OUTPUT FILE
        OPEN( UNIT=1, FILE = OUTPUT )

C       WRITE HEADER AND DATA TO DEFAULT

        WRITE(1,*) 'WAVERIDER CROSSPLANES   ',OUTPUT
        WRITE(1,*)
        WRITE(1,*) 'GEOMETRY:  ', NCAP,' CROSSPLANES, WITH'
       *           ,MCAP,' RADIAL INCREMENTS'
        WRITE(1,*) 'WAVERIDER LENGTH:  ', lw
        WRITE(1,*) 'DERIVED FROM A CONE OF LENGTH:  ',  l
        WRITE(1,*) 'ON DESIGN MACH #:  ', MACH
        WRITE(1,*) 'CONE HALF ANGLE:  ', D*180./PI,'  DEGREES'

        WRITE(1,*) 'SCALE FACTOR:  ', l*D
        WRITE(1,*) 'BASE DESIGN ANGLE:  ',  PHIL*180./PI,'
       *            DEGREES'
        WRITE(1,*)
        WRITE(1,*) 'SCALED CROSSPLANE LEADING EDGE VALUES'
        WRITE(1,*)
        WRITE(1,*)'XPLANE    Rin      Rc       Zw/Lw
        WRITE(1,*)
        DO 5 K = 1,NCAP
        N = K*(MCAP+1)
    5   WRITE(1,*) K,     Rin(N),      Rcb(N),      ZovL(K)

C       CLOSE OUTPUT FILE
```

```
       CLOSE(1)

C   inserted by datta 8-10-91
      close(10)
      OPEN(UNIT=10,file='grid1.bin',FORM='UNFORMATTED')
      write(10) NCAP,BNDS,INCR
      alphaa=0
      rmach=0
      rel=1.0
      time=0.0
7554 format(5E15.8)

      write(10) (((x(i,j,k),i=1,ncap),j=1,bnds),k=1,incr),
      $    (((y(i,j,k),i=1,ncap),j=1,bnds),k=1,incr),
      $    (((z(i,j,k),i=1,ncap),j=1,bnds),k=1,incr)
c   end

C      SET PLOT FILE SUFFIX
       OUTPUT(INDEX(OUTPUT,'.'):) = '.plt'

C      OPEN PLOT FILE
       OPEN(UNIT=2, FILE=OUTPUT)

       WRITE(2,*) 'TITLE=' ,OUTPUT
       WRITE(2,*) 'VARIABLES=X,Y'
       WRITE(2,*) 'ZONE T=GRID2D ,Z=0.,I=',INCR,' ,J=' ,BNDS

        I = NCAP
        DO 30 J = 1,BNDS
         DO 40 K = 1,INCR

         WRITE(2,21) X(I,J,K), Y(I,J,K)
  21     FORMAT(4E12.4)
  40     CONTINUE
  30    CONTINUE
       CLOSE(2)

C      OUTPUT(INDEX(OUTPUT2,'.'):) = '.plt'
C      OPEN PLOT FILE
C      OPEN(UNIT=3, FILE=OUTPUT2)

C      WRITE(3,*) 'TITLE=' ,OUTPUT2
C      WRITE(3,*) 'VARIABLES=X,Y'
C      WRITE(3,*) 'ZONE T=SURF3D ,Z=0.,I=',INCR,' ,J=' ,BNDS

C       DO I = 1,NCAP
C        J = 1
C        DO K = MCAP+1,INCR

C        WRITE(3,22) X(I,J,K), Y(I,J,K)
```

```
C 22      FORMAT(4E12.4)
C         END DO
C        END DO
C       CLOSE(3)

        RETURN
          END


        SUBROUTINE GEOM (sum,asize,num,astep)

        IMPLICIT REAL*8 (a-h,o-z)
        REAL*8 astep(num),xsum,feval,jac,dr,rinit,
       *                  rdif,fstop,rmax

        rinit = 1.0d0
        fstop = 0.00010d0
        icount = 0
        imax = 10
        rmax = 1.5d0
        rdif = 0.01d0
        xsum = sum/asize

1       rinit = rinit + rdif
        dr = rinit
        icount = 0
        IF (rinit.gt.rmax) THEN
         WRITE (*,*) ' rinit exceeded rmax'
         GO TO 99
         END IF

10      CONTINUE

        feval = 1.0d0
        DO 20 i=1,num-1
20         feval = feval + dr**i
        feval = feval - xsum
        IF (ABS(feval).lt.fstop) GO TO 89

        jac = 1.0d0
        DO 30 i=1,num-2
30         jac = jac + (i+1)*dr**i

        dr = dr - feval/jac
        icount = icount + 1
        IF (icount.eq.imax) THEN
           GO TO 1
           ELSE
         GO TO 10
         END IF
```

```
89    astep(1) = asize
      r = dr
      DO 40 i=2,num
40      astep(i) = asize*r**(i-1)
99    RETURN
      END

      SUBROUTINE INDAT(INPUT,MACH,d,l,A0,A1,A2)

C      INDAT READS IN VARIABLE INFORMATION ON CONFIGURATION
C      AND GRID REFINEMENT

      IMPLICIT REAL*8 (a-h,o-z)
      INTEGER BNDS
      REAL*8 MACH,d,l,A0,A1,A2
      CHARACTER INPUT*15
      COMMON MCAP,NCAP,PI,INCR,BNDS,PHIL

      OPEN(UNIT=9,FILE='inp.dat',STATUS='UNKNOWN')
      READ(9,*) INPUT
      READ(9,*) MACH
      READ(9,*) d
      READ(9,*) PHIL
      READ(9,*) l
      READ(9,*) MCAP
      READ(9,*) NCAP
      READ(9,*) BNDS
      READ(9,*) A0
      READ(9,*) A1
      READ(9,*) A2
      CLOSE(9)

      RETURN
      END
```

Case1.dat provides basic geometric information for the baseline configuration and the cusped configuration for a 21 x 21 x 52 system.

WAVERIDER CROSSPLANES   Case1.dat

GEOMETRY: 20 CROSSPLANES, WITH 25 RADIAL INCREMENTS
WAVERIDER LENGTH: 7.0693219900713
DERIVED FROM A CONE OF LENGTH: 10.4174144600000
ON DESIGN MACH #:   10.0000000000000
CONE HALF ANGLE: 5.5000000000000 DEGREES
SCALE FACTOR: 1.0000000002953
BASE DESIGN ANGLE: 50.000000000000 DEGREES

SCALED CROSSPLANE LEADING EDGE VALUES

X-Section	$r_s(\phi)$	z_w/l_w
1	0.49080435397511	4.8297462397621D-03
2	0.51455169899301	2.7978772941810D-02
3	0.55067226693039	6.3189277149572D-02
4	0.59471899012943	0.10612623581606
5	0.64400318030222	0.15416870260294
6	0.69666705750720	0.20550570464392
7	0.75132336655366	0.25878493887404
8	0.80689983153598	0.31296114555785
9	0.86256541418099	0.36722422456999
10	0.91769158502656	0.42096148235287
11	0.97182997824085	0.47373584972654
12	1.0246995494026	0.52527336323077
13	1.0761822125388	0.57545891208830
14	1.1263303749232	0.62434358316288
15	1.1753962792602	0.67217326386202
16	1.2239083010238	0.71946301715148
17	1.2728660163409	0.76718723467112
18	1.3243115940048	0.81733663243099
19	1.3836695727349	0.87519907699343
20	1.5116961290871	0.99999998291933

Case41.dat provides basic geometric information for the intermediately refined 26 x 26 x 56 system.

WAVERIDER CROSSPLANES   Case41.dat

GEOMETRY: 25 CROSSPLANES, WITH 27 RADIAL INCREMENTS
WAVERIDER LENGTH: 7.0693219900713
DERIVED FROM A CONE OF LENGTH: 10.4174144600000
ON DESIGN MACH #:   10.0000000000000
CONE HALF ANGLE: 5.5000000000000 DEGREES
SCALE FACTOR: 1.0000000002953
BASE DESIGN ANGLE: 50.000000000000 DEGREES

SCALED CROSSPLANE LEADING EDGE VALUES

X-Section	$r_s(\phi)$	z_w/l_w
1	0.49080435397511	4.8297462397621D-03
2	0.50854670453363	2.2125075318727D-02
3	0.53488616539412	4.7800909072678D-02
4	0.56717229765334	7.9273586848291D-02
5	0.60371161605371	0.11489229103132
6	0.64330603813099	0.15348912504491
7	0.68504525784039	0.19417671815679
8	0.72820588449587	0.23624990562984
9	0.77219936981079	0.27913496774957
10	0.81654351356092	0.32236185340679
11	0.86084583285821	0.36554796838524
12	0.90479314437913	0.40838802006742
13	0.94814463300996	0.45064726071652
14	0.99072719337429	0.49215694637497
15	1.0324327062042	0.53281168185780
16	1.0732175512370	0.57256894592212
17	1.1131053477006	0.61145176270545
18	1.1521950003542	0.64955654504518
19	1.1906783006056	0.68707025213250
20	1.2288763559609	0.72430590111638
21	1.2673174037572	0.76177842030628
22	1.3069200300291	0.80038325180837
23	1.3495108626819	0.84190100133358
24	1.3999109892383	0.89103128830091
25	1.5116961290871	0.99999998291933

Case42.dat provides the geometric information for the refined 31 x 31 x 62 system.

WAVERIDER CROSSPLANES   Case42.dat

GEOMETRY: 30 CROSSPLANES, WITH 30 RADIAL INCREMENTS
WAVERIDER LENGTH: 7.0693219900713
DERIVED FROM A CONE OF LENGTH: 10.4174144600000
ON DESIGN MACH #:   10.0000000000000
CONE HALF ANGLE: 5.5000000000000 DEGREES
SCALE FACTOR: 1.0000000002953
BASE DESIGN ANGLE: 50.000000000000 DEGREES

SCALED CROSSPLANE LEADING EDGE VALUES

X-Section	$r_s(\phi)$	z_w/l_w
1	0.49080435397511	4.8297462397621D-03
2	0.50569029398797	1.9340632512861D-02
3	0.52739466244908	4.0498155792988D-02
4	0.55399941007504	6.6432592368133D-02
5	0.58423441805863	9.5905824286114D-02
6	0.61718467635717	0.12802589533480
7	0.65214767234646	0.16210799281263
8	0.68855928512003	0.19760220893342
9	0.72595327932595	0.23405405522263
10	0.76393814463434	0.27108188551839
11	0.80218321525552	0.30836336521072
12	0.84040988260167	0.34562690530160
13	0.87838566511969	0.38264588164942
14	0.91591992859129	0.41923446309678
15	0.95286061571449	0.45524442345077
16	0.98909166836696	0.49056262869281
17	1.0245310255388	0.52510908535384
18	1.0591292205036	0.55883557302972
19	1.0928687268234	0.59172500686423
20	1.1257643552358	0.62379182443593
21	1.1578652382694	0.65508392037102
22	1.1892593589197	0.68568706091889
23	1.2200824051018	0.71573351531489
24	1.2505344985099	0.74541836315400
25	1.2809125031340	0.77503098888830
26	1.3116766368658	0.80502001514301
27	1.3436044810946	0.83614343201490
28	1.3782221081230	0.86988886216040
29	1.4195327494587	0.91015867500213
30	1.5116961290871	0.99999998291933

Appendix B. Euler Input Files

Table B.1 contains the input parameters for the starting solution input file 100K1DAT.

Table B.1. Input Parameters for 100K1DAT On-Design Grid Refinement

VARIABLE	CASE 1 Baseline	CASE 2 Cusped	CASE 3 interm	CASE 4 refine
INS	0	0	0	0
ICASE	8	8	8	8
ILCTST	1	1	1	1
ICFL	5	5	5	5
CFLMAX	0.9	0.9	0.9	0.9
IMPLT	0.01	0.01	0.01	0.01
ISWVL	0	0	0	0
ILMTR	2	2	2	2
ALPHA	0	0	0	0
PHI	0	0	0	0
RM	10.	10.	10.	10.
REL	1.E7	1.E7	1.E7	1.E7
TINF	408.57	408.57	408.57	408.57
PINF	23.271	23.271	23.271	23.271
IADBWL	1	1	1	1
TWALL	530.00	530.00	530.00	530.00
IL	21	21	26	31
JL	21	21	26	31
KL	52	52	56	62
IMETRC	0	0	0	0
RL	6.4273	6.4273	6.4273	6.4273
NEND	100	100	100	100
IREAD	0	0	0	0
IGRID	2	2	2	2
IP3DOP	2	2	2	2
MODPR	10	10	10	10

Table B.2 contains the input parameters for input file 100K1dat for the off-design Mach number investigations.

Table B.2. Input Parameters for 100K1DAT Off-Design Mach Number

VARIABLE	MACH 8.00	MACH 9.00	MACH 11.0	MACH 15.0	MACH 20.0
INS	0	0	0	0	0
ICASE	8	8	8	8	8
ILCTST	1	1	1	1	1
ICFL	5	5	5	5	5
CFLMAX	0.9	0.9	0.9	0.9	0.9
IMPLT	0.01	0.01	0.01	0.01	0.01
ISWVL	0	0	0	0	0
ILMTR	2	2	2	2	2
ALPHA	0	0	0	0	0
PHI	0	0	0	0	0
RM	8.0	9.0	11.0	15.0	20.0
REL	1.E7	1.E7	1.E7	1.E7	1.E7
TINF	408.57	408.57	408.57	408.57	408.57
PINF	23.271	23.271	23.271	23.271	23.271
IADBWL	1	1	1	1	1
TWALL	530.00	530.00	530.00	530.00	530.00
IL	31	21	21	21	21
JL	31	21	21	21	21
KL	62	52	52	52	52
IMETRC	0	0	0	0	0
RL	6.4273	6.4273	6.4273	6.4273	6.4273
NEND	100	100	100	100	100
IREAD	0	0	0	0	0
IGRID	2	2	2	2	2
IP3DOP	2	2	2	2	2
MODPR	10	10	10	10	10

Table B.3 contains the input parameters for input file 100K1dat for the off-design angle of attack investigations.

Table B.3. Input Parameters for 100K1DAT
Off-Design Angle of Attack

VARIABLE	5°	2°	1°	-2°	-5°
INS	0	0	0	0	0
ICASE	8	8	8	8	8
ILCTST	1	1	1	1	1
ICFL	5	5	5	5	5
CFLMAX	0.9	0.9	0.9	0.9	0.9
IMPLT	0.01	0.01	0.01	0.01	0.01
ISWVL	0	0	0	0	0
ILMTR	2	2	2	2	2
ALPHA	-.0873	-.0349	-.0175	.0349	.0873
PHI	0	0	0	0	0
RM	10.0	10.0	10.0	10.0	10.0
REL	1.E7	1.E7	1E.7	1.E7	1.E7
TINF	408.57	408.57	408.57	408.57	408.57
PINF	23.271	23.271	23.271	23.271	23.271
IADBWL	1	1	1	1	1
TWALL	530.00	530.00	530.00	530.00	530.00
IL	31	31	31	31	31
JL	31	31	31	31	31
KL	62	62	62	62	62
IMETRC	0	0	0	0	0
RL	6.4273	6.4273	6.4273	6.4273	6.4273
NEND	100	100	100	100	100
IREAD	0	0	0	0	0
IGRID	2	2	2	2	2
IP3DOP	2	2	2	2	2
MODPR	10	10	10	10	10

Table B.4 lists input file 100K1DAT in the actual format read by the program EULER.F.

Table B.4. Formatted Input File 100k1dat

```
100   NEND
0    INS
21 21 52  IL,JL,KL
1 5 10 0.9 0.01    ILCTST,ICFL,CFLEXP,CFLMAX,CFL
0 1 1 1 1 1        IREST,CFCRHO,CFCEI,CFLPEN,
CEXPPEN,INOFRZ
0 1 2 2 1.0        IMPLT,IIMORD,NSWPS,IPC,COEF
4 1 0               ISWVL,IVEPC,ITURB
2 1.0 1.E-6 0.05 2 1 1 1
ILMTR,OMEGA,DELTEP,DELTIL,IENTH,IISO,JISO,KISO
1     IAVE NEXT LINE
IADBWL,ICASE,ALPHA,PHI,TWALL,RM,REL,RL,TINF then..
1 8 0.0 0.0 530.0  10.00 1.E7 6.42731323  408.57 23.27212
0 PINF,IGRID,IMETRC
0 2 0 10 100000000 0
IREAD,IP3DOP,IDGBUG,MODPR,IP3DMD,NRST
1 1 1             READ(IUNDAT,*) IFMRTI,IFMRTO,IINT


parameters for icase=6
0 6 20. 0. 530.0 16.34 295230.6655 0.25 93.93 1.73232 1 0
```

Appendix C Euler Convergence Files

On-Design Evaluations

Table C.1 contains the convergence history of the baseline waverider model.

Table C.1 Baseline Convergence History

CHARACTERISTIC TIME = 6.487443200971E-4
CHARACTERISTIC LENGTH = 6.42731323
UsubINF = 9907.313298771
FIRST RESIDUAL = 638.1174320464

ITER	T/Tc	RESIDUAL	DT	CFL
1	0.108168E-05	0.100000E+01	0.7017E-09	0.1072E-01
10	0.150513E-04	0.987106E+00	0.1306E-08	0.2000E-01
20	0.450472E-04	0.959233E+00	0.2602E-08	0.4000E-01
30	0.104758E-03	0.902101E+00	0.5179E-08	0.8000E-01
40	0.223817E-03	0.778990E+00	0.1035E-07	0.1600E+00
50	0.463114E-03	0.535982E+00	0.2088E-07	0.3200E+00
60	0.946381E-03	0.343765E+00	0.4204E-07	0.6400E+00
70	0.180237E-02	0.310749E+00	0.5918E-07	0.9000E+00
80	0.271435E-02	0.194889E+00	0.5913E-07	0.9000E+00
90	0.362526E-02	0.147503E+00	0.5908E-07	0.9000E+00
100	0.453610E-02	0.107464E+00	0.5909E-07	0.9000E+00
110	0.544687E-02	0.834836E-01	0.5908E-07	0.9000E+00
120	0.635763E-02	0.719000E-01	0.5908E-07	0.9000E+00
130	0.726836E-02	0.525866E-01	0.5908E-07	0.9000E+00
140	0.817909E-02	0.421235E-01	0.5908E-07	0.9000E+00
150	0.908981E-02	0.337710E-01	0.5908E-07	0.9000E+00
160	0.100005E-01	0.277869E-01	0.5908E-07	0.9000E+00
170	0.109113E-01	0.210991E-01	0.5908E-07	0.9000E+00
180	0.118220E-01	0.156831E-01	0.5908E-07	0.9000E+00
190	0.127327E-01	0.144885E-01	0.5908E-07	0.9000E+00
200	0.136434E-01	0.102390E-01	0.5908E-07	0.9000E+00
210	0.145542E-01	0.724318E-02	0.5908E-07	0.9000E+00
220	0.154649E-01	0.584044E-02	0.5908E-07	0.9000E+00
230	0.163756E-01	0.384976E-02	0.5908E-07	0.9000E+00
240	0.172864E-01	0.337824E-02	0.5908E-07	0.9000E+00
250	0.181971E-01	0.274156E-02	0.5908E-07	0.9000E+00
260	0.191078E-01	0.193191E-02	0.5908E-07	0.9000E+00
270	0.200185E-01	0.171719E-02	0.5908E-07	0.9000E+00
280	0.209293E-01	0.127424E-02	0.5908E-07	0.9000E+00

ITER	T/Tc	RESIDUAL	DT	CFL
290	0.218400E-01	0.106228E-02	0.5908E-07	0.9000E+00
300	0.227507E-01	0.991979E-03	0.5908E-07	0.9000E+00
310	0.236614E-01	0.813735E-03	0.5908E-07	0.9000E+00
320	0.245721E-01	0.636332E-03	0.5908E-07	0.9000E+00
330	0.254828E-01	0.533785E-03	0.5908E-07	0.9000E+00
340	0.263935E-01	0.440807E-03	0.5908E-07	0.9000E+00
350	0.273043E-01	0.346782E-03	0.5908E-07	0.9000E+00
360	0.282150E-01	0.262590E-03	0.5908E-07	0.9000E+00
370	0.291257E-01	0.219325E-03	0.5908E-07	0.9000E+00
380	0.300364E-01	0.197003E-03	0.5908E-07	0.9000E+00
390	0.309471E-01	0.138566E-03	0.5908E-07	0.9000E+00
400	0.318578E-01	0.100968E-03	0.5908E-07	0.9000E+00
410	0.327685E-01	0.758903E-04	0.5908E-07	0.9000E+00
420	0.336793E-01	0.728357E-04	0.5908E-07	0.9000E+00
430	0.345900E-01	0.635563E-04	0.5908E-07	0.9000E+00
440	0.355007E-01	0.482796E-04	0.5908E-07	0.9000E+00
450	0.364114E-01	0.333208E-04	0.5908E-07	0.9000E+00
460	0.373221E-01	0.266812E-04	0.5908E-07	0.9000E+00
470	0.382328E-01	0.280016E-04	0.5908E-07	0.9000E+00
480	0.391435E-01	0.272372E-04	0.5908E-07	0.9000E+00
490	0.400542E-01	0.225657E-04	0.5908E-07	0.9000E+00
500	0.409650E-01	0.167634E-04	0.5908E-07	0.9000E+00
510	0.418757E-01	0.144619E-04	0.5908E-07	0.9000E+00
520	0.427864E-01	0.127861E-04	0.5908E-07	0.9000E+00
530	0.436971E-01	0.107754E-04	0.5908E-07	0.9000E+00
540	0.446078E-01	0.768828E-05	0.5908E-07	0.9000E+00
550	0.455185E-01	0.629197E-05	0.5908E-07	0.9000E+00
560	0.464292E-01	0.568532E-05	0.5908E-07	0.9000E+00
570	0.473400E-01	0.500296E-05	0.5908E-07	0.9000E+00
580	0.482507E-01	0.404661E-05	0.5908E-07	0.9000E+00
590	0.491614E-01	0.314502E-05	0.5908E-07	0.9000E+00
600	0.500721E-01	0.274597E-05	0.5908E-07	0.9000E+00
610	0.509828E-01	0.244522E-05	0.5908E-07	0.9000E+00
620	0.518935E-01	0.212623E-05	0.5908E-07	0.9000E+00
630	0.528042E-01	0.173760E-05	0.5908E-07	0.9000E+00
640	0.537149E-01	0.148956E-05	0.5908E-07	0.9000E+00
650	0.546257E-01	0.138128E-05	0.5908E-07	0.9000E+00
660	0.555364E-01	0.118310E-05	0.5908E-07	0.9000E+00
670	0.564471E-01	0.985164E-06	0.5908E-07	0.9000E+00
680	0.573578E-01	0.838512E-06	0.5908E-07	0.9000E+00
690	0.582685E-01	0.717336E-06	0.5908E-07	0.9000E+00
700	0.591792E-01	0.644798E-06	0.5908E-07	0.9000E+00
710	0.600899E-01	0.534282E-06	0.5908E-07	0.9000E+00
720	0.610007E-01	0.449444E-06	0.5908E-07	0.9000E+00
730	0.619114E-01	0.387277E-06	0.5908E-07	0.9000E+00
740	0.628221E-01	0.318180E-06	0.5908E-07	0.9000E+00
750	0.637328E-01	0.283101E-06	0.5908E-07	0.9000E+00
760	0.646435E-01	0.224084E-06	0.5908E-07	0.9000E+00

ITER	T/Tc	RESIDUAL	DT	CFL
770	0.655542E-01	0.192567E-06	0.5908E-07	0.9000E+00
780	0.664649E-01	0.162064E-06	0.5908E-07	0.9000E+00
790	0.673756E-01	0.133386E-06	0.5908E-07	0.9000E+00
800	0.682864E-01	0.115788E-06	0.5908E-07	0.9000E+00

Table C.2 contains the convergence history for the on-design cusped waverider model.

Table C.2 Cusped Convergence File

CHARACTERISTIC TIME = 6.487443200971E-4
CHARACTERISTIC LENGTH = 6.42731323
UsubINF = 9907.313298771
FIRST RESIDUAL = 636.0423389967

ITER	T/Tc	Presidual	RESIDUAL	QRESID	DT	CFL
1	0.109615E-05	0.324858E-01	0.100000E+01	0.000000E+00	0.7111E-09	0.1072E-01
10	0.152527E-04	0.330266E-01	0.987250E+00	0.000000E+00	0.1324E-08	0.2000E-01
20	0.456502E-04	0.342193E-01	0.959657E+00	0.000000E+00	0.2637E-08	0.4000E-01
30	0.106162E-03	0.367029E-01	0.902774E+00	0.000000E+00	0.5248E-08	0.8000E-01
40	0.226826E-03	0.419313E-01	0.779700E+00	0.000000E+00	0.1049E-07	0.1600E+00
50	0.469318E-03	0.521351E-01	0.536583E+00	0.000000E+00	0.2116E-07	0.3200E+00
60	0.958624E-03	0.642547E-01	0.344884E+00	0.000000E+00	0.4253E-07	0.6400E+00
70	0.182397E-02	0.568961E-01	0.311605E+00	0.000000E+00	0.5982E-07	0.9000E+00
80	0.274577E-02	0.573833E-01	0.195501E+00	0.000000E+00	0.5977E-07	0.9000E+00
90	0.366656E-02	0.572364E-01	0.147999E+00	0.000000E+00	0.5972E-07	0.9000E+00
100	0.458724E-02	0.574626E-01	0.107822E+00	0.000000E+00	0.5973E-07	0.9000E+00
110	0.550785E-02	0.576035E-01	0.837229E-01	0.000000E+00	0.5972E-07	0.9000E+00
120	0.642843E-02	0.576147E-01	0.721253E-01	0.000000E+00	0.5972E-07	0.9000E+00
130	0.734899E-02	0.577187E-01	0.527320E-01	0.000000E+00	0.5972E-07	0.9000E+00
140	0.826954E-02	0.578439E-01	0.422529E-01	0.000000E+00	0.5972E-07	0.9000E+00
150	0.919009E-02	0.578478E-01	0.338507E-01	0.000000E+00	0.5972E-07	0.9000E+00
160	0.101106E-01	0.578911E-01	0.278707E-01	0.000000E+00	0.5972E-07	0.9000E+00
170	0.110312E-01	0.579814E-01	0.211541E-01	0.000000E+00	0.5972E-07	0.9000E+00
180	0.119517E-01	0.579800E-01	0.157340E-01	0.000000E+00	0.5972E-07	0.9000E+00
190	0.128723E-01	0.579877E-01	0.145231E-01	0.000000E+00	0.5972E-07	0.9000E+00
200	0.137928E-01	0.580284E-01	0.102592E-01	0.000000E+00	0.5972E-07	0.9000E+00
210	0.147134E-01	0.580491E-01	0.726066E-02	0.000000E+00	0.5972E-07	0.9000E+00
220	0.156340E-01	0.580545E-01	0.584763E-02	0.000000E+00	0.5972E-07	0.9000E+00
230	0.165545E-01	0.580755E-01	0.386004E-02	0.000000E+00	0.5972E-07	0.9000E+00
240	0.174751E-01	0.580751E-01	0.338961E-02	0.000000E+00	0.5972E-07	0.9000E+00
250	0.183956E-01	0.580816E-01	0.274520E-02	0.000000E+00	0.5972E-07	0.9000E+00
260	0.193162E-01	0.580902E-01	0.193688E-02	0.000000E+00	0.5972E-07	0.9000E+00
270	0.202367E-01	0.580930E-01	0.171949E-02	0.000000E+00	0.5972E-07	0.9000E+00
280	0.211573E-01	0.580954E-01	0.127726E-02	0.000000E+00	0.5972E-07	0.9000E+00
290	0.220778E-01	0.580984E-01	0.106489E-02	0.000000E+00	0.5972E-07	0.9000E+00
300	0.229983E-01	0.581022E-01	0.993775E-03	0.000000E+00	0.5972E-07	0.9000E+00
310	0.239189E-01	0.581047E-01	0.813750E-03	0.000000E+00	0.5972E-07	0.9000E+00
320	0.248394E-01	0.581069E-01	0.637912E-03	0.000000E+00	0.5972E-07	0.9000E+00
330	0.257600E-01	0.581086E-01	0.535008E-03	0.000000E+00	0.5972E-07	0.9000E+00
340	0.266805E-01	0.581097E-01	0.441782E-03	0.000000E+00	0.5972E-07	0.9000E+00
350	0.276010E-01	0.581109E-01	0.346655E-03	0.000000E+00	0.5972E-07	0.9000E+00
360	0.285216E-01	0.581116E-01	0.262799E-03	0.000000E+00	0.5972E-07	0.9000E+00
370	0.294421E-01	0.581122E-01	0.219752E-03	0.000000E+00	0.5972E-07	0.9000E+00
380	0.303627E-01	0.581126E-01	0.196067E-03	0.000000E+00	0.5972E-07	0.9000E+00
390	0.312832E-01	0.581130E-01	0.136675E-03	0.000000E+00	0.5972E-07	0.9000E+00
400	0.322037E-01	0.581132E-01	0.987898E-04	0.000000E+00	0.5972E-07	0.9000E+00
410	0.331243E-01	0.581134E-01	0.748948E-04	0.000000E+00	0.5972E-07	0.9000E+00
420	0.340448E-01	0.581135E-01	0.716040E-04	0.000000E+00	0.5972E-07	0.9000E+00
430	0.349654E-01	0.581136E-01	0.623405E-04	0.000000E+00	0.5972E-07	0.9000E+00
440	0.358859E-01	0.581137E-01	0.468163E-04	0.000000E+00	0.5972E-07	0.9000E+00
450	0.368064E-01	0.581138E-01	0.325645E-04	0.000000E+00	0.5972E-07	0.9000E+00
460	0.377270E-01	0.581138E-01	0.261094E-04	0.000000E+00	0.5972E-07	0.9000E+00
470	0.386475E-01	0.581138E-01	0.273996E-04	0.000000E+00	0.5972E-07	0.9000E+00
480	0.395681E-01	0.581139E-01	0.263828E-04	0.000000E+00	0.5972E-07	0.9000E+00

ITER	T/Tc	Presidual	RESIDUAL	QRESID	DT	CFL
490	0.404886E-01	0.581139E-01	0.222199E-04	0.000000E+00	0.5972E-07	0.9000E+00
500	0.414091E-01	0.581139E-01	0.170245E-04	0.000000E+00	0.5972E-07	0.9000E+00
510	0.423297E-01	0.581139E-01	0.147246E-04	0.000000E+00	0.5972E-07	0.9000E+00
520	0.432502E-01	0.581139E-01	0.128405E-04	0.000000E+00	0.5972E-07	0.9000E+00
530	0.441707E-01	0.581139E-01	0.106350E-04	0.000000E+00	0.5972E-07	0.9000E+00
540	0.450913E-01	0.581139E-01	0.778079E-05	0.000000E+00	0.5972E-07	0.9000E+00
550	0.460118E-01	0.581139E-01	0.652920E-05	0.000000E+00	0.5972E-07	0.9000E+00
560	0.469324E-01	0.581139E-01	0.599519E-05	0.000000E+00	0.5972E-07	0.9000E+00
570	0.478529E-01	0.581139E-01	0.521461E-05	0.000000E+00	0.5972E-07	0.9000E+00
580	0.487734E-01	0.581139E-01	0.423987E-05	0.000000E+00	0.5972E-07	0.9000E+00
590	0.496940E-01	0.581139E-01	0.333830E-05	0.000000E+00	0.5972E-07	0.9000E+00
600	0.506145E-01	0.581139E-01	0.294374E-05	0.000000E+00	0.5972E-07	0.9000E+00
610	0.515351E-01	0.581139E-01	0.263739E-05	0.000000E+00	0.5972E-07	0.9000E+00
620	0.524556E-01	0.581139E-01	0.227185E-05	0.000000E+00	0.5972E-07	0.9000E+00
630	0.533761E-01	0.581139E-01	0.186033E-05	0.000000E+00	0.5972E-07	0.9000E+00
640	0.542967E-01	0.581139E-01	0.159236E-05	0.000000E+00	0.5972E-07	0.9000E+00
650	0.552172E-01	0.581139E-01	0.147742E-05	0.000000E+00	0.5972E-07	0.9000E+00
660	0.561378E-01	0.581139E-01	0.126708E-05	0.000000E+00	0.5972E-07	0.9000E+00
670	0.570583E-01	0.581139E-01	0.104728E-05	0.000000E+00	0.5972E-07	0.9000E+00
680	0.579788E-01	0.581139E-01	0.882238E-06	0.000000E+00	0.5972E-07	0.9000E+00
690	0.588994E-01	0.581139E-01	0.753236E-06	0.000000E+00	0.5972E-07	0.9000E+00
700	0.598199E-01	0.581139E-01	0.673477E-06	0.000000E+00	0.5972E-07	0.9000E+00
710	0.607405E-01	0.581139E-01	0.556102E-06	0.000000E+00	0.5972E-07	0.9000E+00
720	0.616610E-01	0.581139E-01	0.463405E-06	0.000000E+00	0.5972E-07	0.9000E+00
730	0.625815E-01	0.581139E-01	0.396265E-06	0.000000E+00	0.5972E-07	0.9000E+00
740	0.635021E-01	0.581139E-01	0.327442E-06	0.000000E+00	0.5972E-07	0.9000E+00
750	0.644226E-01	0.581139E-01	0.288019E-06	0.000000E+00	0.5972E-07	0.9000E+00
760	0.653431E-01	0.581139E-01	0.227862E-06	0.000000E+00	0.5972E-07	0.9000E+00
770	0.662637E-01	0.581139E-01	0.194386E-06	0.000000E+00	0.5972E-07	0.9000E+00
780	0.671842E-01	0.581139E-01	0.163320E-06	0.000000E+00	0.5972E-07	0.9000E+00
790	0.681048E-01	0.581139E-01	0.134675E-06	0.000000E+00	0.5972E-07	0.9000E+00
800	0.690253E-01	0.581139E-01	0.115791E-06	0.000000E+00	0.5972E-07	0.9000E+00

Table C.3 contains the convergence history of the intermediately refined 26x26x56 system for on-design flight conditions.

Table C.3 Case 1r Convergence File

CHARACTERISTIC TIME = 6.487443200971E-4
CHARACTERISTIC LENGTH = 6.42731323
UsubINF = 9907.313298771
FIRST RESIDUAL = 546.7869235886

ITER	T/Tc	Presidual	RESIDUAL	QRESID	DT	CFL
1	0.783880E-06	0.278141E-01	0.100000E+01	0.000000E+00	0.5085E-09	0.1072E-01
10	0.109069E-04	0.282878E-01	0.987944E+00	0.000000E+00	0.9465E-09	0.2000E-01
20	0.326406E-04	0.293333E-01	0.961685E+00	0.000000E+00	0.1885E-08	0.4000E-01
30	0.759051E-04	0.315134E-01	0.907244E+00	0.000000E+00	0.3753E-08	0.8000E-01
40	0.162245E-03	0.361116E-01	0.788221E+00	0.000000E+00	0.7509E-08	0.1600E+00
50	0.336441E-03	0.450973E-01	0.552706E+00	0.000000E+00	0.1524E-07	0.3200E+00
60	0.691576E-03	0.556959E-01	0.369305E+00	0.000000E+00	0.3104E-07	0.6400E+00
70	0.132690E-02	0.487472E-01	0.340011E+00	0.000000E+00	0.4400E-07	0.9000E+00
80	0.200375E-02	0.494401E-01	0.237808E+00	0.000000E+00	0.4381E-07	0.9000E+00
90	0.267884E-02	0.492355E-01	0.186676E+00	0.000000E+00	0.4381E-07	0.9000E+00
100	0.335407E-02	0.493452E-01	0.150360E+00	0.000000E+00	0.4380E-07	0.9000E+00
110	0.402918E-02	0.494321E-01	0.120465E+00	0.000000E+00	0.4380E-07	0.9000E+00
120	0.470427E-02	0.495391E-01	0.923763E-01	0.000000E+00	0.4380E-07	0.9000E+00
130	0.537934E-02	0.495940E-01	0.784690E-01	0.000000E+00	0.4379E-07	0.9000E+00
140	0.605439E-02	0.495671E-01	0.635379E-01	0.000000E+00	0.4379E-07	0.9000E+00
150	0.672944E-02	0.497315E-01	0.539730E-01	0.000000E+00	0.4379E-07	0.9000E+00
160	0.740448E-02	0.496631E-01	0.455820E-01	0.000000E+00	0.4379E-07	0.9000E+00
170	0.807953E-02	0.497944E-01	0.347126E-01	0.000000E+00	0.4379E-07	0.9000E+00
180	0.875457E-02	0.497594E-01	0.301625E-01	0.000000E+00	0.4379E-07	0.9000E+00
190	0.942961E-02	0.498049E-01	0.251175E-01	0.000000E+00	0.4379E-07	0.9000E+00
200	0.101047E-01	0.498393E-01	0.209883E-01	0.000000E+00	0.4379E-07	0.9000E+00
210	0.107797E-01	0.498387E-01	0.174267E-01	0.000000E+00	0.4379E-07	0.9000E+00
220	0.114548E-01	0.498429E-01	0.133169E-01	0.000000E+00	0.4379E-07	0.9000E+00
230	0.121298E-01	0.498670E-01	0.108797E-01	0.000000E+00	0.4379E-07	0.9000E+00
240	0.128049E-01	0.498876E-01	0.100482E-01	0.000000E+00	0.4379E-07	0.9000E+00
250	0.134799E-01	0.498912E-01	0.797508E-02	0.000000E+00	0.4379E-07	0.9000E+00
260	0.141550E-01	0.498910E-01	0.683174E-02	0.000000E+00	0.4379E-07	0.9000E+00
270	0.148300E-01	0.498998E-01	0.588968E-02	0.000000E+00	0.4379E-07	0.9000E+00
280	0.155051E-01	0.499073E-01	0.470948E-02	0.000000E+00	0.4379E-07	0.9000E+00
290	0.161801E-01	0.499072E-01	0.355826E-02	0.000000E+00	0.4379E-07	0.9000E+00
300	0.168552E-01	0.499135E-01	0.267886E-02	0.000000E+00	0.4379E-07	0.9000E+00
310	0.175302E-01	0.499169E-01	0.219767E-02	0.000000E+00	0.4379E-07	0.9000E+00
320	0.182053E-01	0.499207E-01	0.166735E-02	0.000000E+00	0.4379E-07	0.9000E+00
330	0.188803E-01	0.499219E-01	0.130626E-02	0.000000E+00	0.4379E-07	0.9000E+00
340	0.195553E-01	0.499237E-01	0.100324E-02	0.000000E+00	0.4379E-07	0.9000E+00
350	0.202304E-01	0.499256E-01	0.829711E-03	0.000000E+00	0.4379E-07	0.9000E+00
360	0.209054E-01	0.499277E-01	0.651907E-03	0.000000E+00	0.4379E-07	0.9000E+00
370	0.215805E-01	0.499290E-01	0.569703E-03	0.000000E+00	0.4379E-07	0.9000E+00
380	0.222555E-01	0.499304E-01	0.453480E-03	0.000000E+00	0.4379E-07	0.9000E+00
390	0.229305E-01	0.499310E-01	0.353516E-03	0.000000E+00	0.4379E-07	0.9000E+00
400	0.236056E-01	0.499319E-01	0.245836E-03	0.000000E+00	0.4379E-07	0.9000E+00
410	0.242806E-01	0.499327E-01	0.221224E-03	0.000000E+00	0.4379E-07	0.9000E+00
420	0.249557E-01	0.499333E-01	0.174276E-03	0.000000E+00	0.4379E-07	0.9000E+00
430	0.256307E-01	0.499337E-01	0.139919E-03	0.000000E+00	0.4379E-07	0.9000E+00
440	0.263057E-01	0.499340E-01	0.122024E-03	0.000000E+00	0.4379E-07	0.9000E+00
450	0.269808E-01	0.499343E-01	0.101159E-03	0.000000E+00	0.4379E-07	0.9000E+00

ITER	T/Tc	Presidual	RESIDUAL	QRESID	DT	CFL
460	0.276558E-01	0.499345E-01	0.870630E-04	0.000000E+00	0.4379E-07	0.9000E+00
470	0.283309E-01	0.499347E-01	0.750340E-04	0.000000E+00	0.4379E-07	0.9000E+00
480	0.290059E-01	0.499348E-01	0.572747E-04	0.000000E+00	0.4379E-07	0.9000E+00
490	0.296809E-01	0.499349E-01	0.582633E-04	0.000000E+00	0.4379E-07	0.9000E+00
500	0.303560E-01	0.499349E-01	0.423039E-04	0.000000E+00	0.4379E-07	0.9000E+00
510	0.310310E-01	0.499350E-01	0.403352E-04	0.000000E+00	0.4379E-07	0.9000E+00
520	0.317061E-01	0.499351E-01	0.310507E-04	0.000000E+00	0.4379E-07	0.9000E+00
530	0.323811E-01	0.499351E-01	0.285549E-04	0.000000E+00	0.4379E-07	0.9000E+00
540	0.330561E-01	0.499351E-01	0.211957E-04	0.000000E+00	0.4379E-07	0.9000E+00
550	0.337312E-01	0.499351E-01	0.218655E-04	0.000000E+00	0.4379E-07	0.9000E+00
560	0.344062E-01	0.499351E-01	0.170249E-04	0.000000E+00	0.4379E-07	0.9000E+00
570	0.350813E-01	0.499352E-01	0.155616E-04	0.000000E+00	0.4379E-07	0.9000E+00
580	0.357563E-01	0.499352E-01	0.127774E-04	0.000000E+00	0.4379E-07	0.9000E+00
590	0.364313E-01	0.499352E-01	0.112513E-04	0.000000E+00	0.4379E-07	0.9000E+00
600	0.371064E-01	0.499352E-01	0.891414E-05	0.000000E+00	0.4379E-07	0.9000E+00
610	0.377814E-01	0.499352E-01	0.791268E-05	0.000000E+00	0.4379E-07	0.9000E+00
620	0.384564E-01	0.499352E-01	0.614271E-05	0.000000E+00	0.4379E-07	0.9000E+00
630	0.391315E-01	0.499352E-01	0.534662E-05	0.000000E+00	0.4379E-07	0.9000E+00
640	0.398065E-01	0.499352E-01	0.426959E-05	0.000000E+00	0.4379E-07	0.9000E+00
650	0.404816E-01	0.499352E-01	0.358298E-05	0.000000E+00	0.4379E-07	0.9000E+00
660	0.411566E-01	0.499352E-01	0.300728E-05	0.000000E+00	0.4379E-07	0.9000E+00
670	0.418316E-01	0.499352E-01	0.244467E-05	0.000000E+00	0.4379E-07	0.9000E+00
680	0.425067E-01	0.499352E-01	0.204716E-05	0.000000E+00	0.4379E-07	0.9000E+00
690	0.431817E-01	0.499352E-01	0.170242E-05	0.000000E+00	0.4379E-07	0.9000E+00
700	0.438568E-01	0.499352E-01	0.140371E-05	0.000000E+00	0.4379E-07	0.9000E+00
710	0.445318E-01	0.499352E-01	0.116680E-05	0.000000E+00	0.4379E-07	0.9000E+00
720	0.452068E-01	0.499352E-01	0.983533E-06	0.000000E+00	0.4379E-07	0.9000E+00
730	0.458819E-01	0.499352E-01	0.810160E-06	0.000000E+00	0.4379E-07	0.9000E+00
740	0.465569E-01	0.499352E-01	0.691519E-06	0.000000E+00	0.4379E-07	0.9000E+00
750	0.472320E-01	0.499352E-01	0.561728E-06	0.000000E+00	0.4379E-07	0.9000E+00
760	0.479070E-01	0.499352E-01	0.494014E-06	0.000000E+00	0.4379E-07	0.9000E+00
770	0.485820E-01	0.499352E-01	0.395673E-06	0.000000E+00	0.4379E-07	0.9000E+00
780	0.492571E-01	0.499352E-01	0.343662E-06	0.000000E+00	0.4379E-07	0.9000E+00
790	0.499321E-01	0.499352E-01	0.285305E-06	0.000000E+00	0.4379E-07	0.9000E+00
800	0.506072E-01	0.499352E-01	0.239048E-06	0.000000E+00	0.4379E-07	0.9000E+00
810	0.512822E-01	0.499352E-01	0.203376E-06	0.000000E+00	0.4379E-07	0.9000E+00
820	0.519572E-01	0.499352E-01	0.167556E-06	0.000000E+00	0.4379E-07	0.9000E+00
830	0.526323E-01	0.499352E-01	0.138640E-06	0.000000E+00	0.4379E-07	0.9000E+00
840	0.533073E-01	0.499352E-01	0.118352E-06	0.000000E+00	0.4379E-07	0.9000E+00
850	0.539824E-01	0.499352E-01	0.954414E-07	0.000000E+00	0.4379E-07	0.9000E+00
860	0.546574E-01	0.499352E-01	0.820074E-07	0.000000E+00	0.4379E-07	0.9000E+00
870	0.553324E-01	0.499352E-01	0.696991E-07	0.000000E+00	0.4379E-07	0.9000E+00
880	0.560075E-01	0.499352E-01	0.581178E-07	0.000000E+00	0.4379E-07	0.9000E+00
890	0.566825E-01	0.499352E-01	0.522797E-07	0.000000E+00	0.4379E-07	0.9000E+00
900	0.573575E-01	0.499352E-01	0.443853E-07	0.000000E+00	0.4379E-07	0.9000E+00

Table C.4 contains the convergence history of the refined 31x31x62 system for on-design flight conditions.

Table C.4 Case 2r Convergence File

CHARACTERISTIC TIME = 6.487443200971E-4
CHARACTERISTIC LENGTH = 6.42731323
UsubINF = 9907.313298771
FIRST RESIDUAL = 492.5331529885

ITER	T/Tc	Presidual	RESIDUAL	QRESID	DT	CFL
1	0.572159E-06	0.240053E-01	0.100000E+01	0.000000E+00	0.3712E-09	0.1072E-01
10	0.796067E-05	0.244243E-01	0.988822E+00	0.000000E+00	0.6908E-09	0.2000E-01
20	0.238225E-04	0.253505E-01	0.964320E+00	0.000000E+00	0.1376E-08	0.4000E-01
30	0.554016E-04	0.272868E-01	0.912937E+00	0.000000E+00	0.2740E-08	0.8000E-01
40	0.118489E-03	0.313885E-01	0.798969E+00	0.000000E+00	0.5492E-08	0.1600E+00
50	0.246363E-03	0.394554E-01	0.573839E+00	0.000000E+00	0.1123E-07	0.3200E+00
60	0.510350E-03	0.489282E-01	0.403409E+00	0.000000E+00	0.2323E-07	0.6400E+00
70	0.989443E-03	0.421881E-01	0.355430E+00	0.000000E+00	0.3324E-07	0.9000E+00
80	0.149856E-02	0.430788E-01	0.265826E+00	0.000000E+00	0.3288E-07	0.9000E+00
90	0.200552E-02	0.428801E-01	0.199378E+00	0.000000E+00	0.3291E-07	0.9000E+00
100	0.251275E-02	0.429026E-01	0.165408E+00	0.000000E+00	0.3290E-07	0.9000E+00
110	0.301990E-02	0.429417E-01	0.137444E+00	0.000000E+00	0.3291E-07	0.9000E+00
120	0.352714E-02	0.429519E-01	0.115679E+00	0.000000E+00	0.3291E-07	0.9000E+00
130	0.403441E-02	0.429816E-01	0.100965E+00	0.000000E+00	0.3291E-07	0.9000E+00
140	0.454171E-02	0.430688E-01	0.831576E-01	0.000000E+00	0.3291E-07	0.9000E+00
150	0.504903E-02	0.430953E-01	0.717100E-01	0.000000E+00	0.3291E-07	0.9000E+00
160	0.555635E-02	0.430641E-01	0.583696E-01	0.000000E+00	0.3291E-07	0.9000E+00
170	0.606366E-02	0.431832E-01	0.524882E-01	0.000000E+00	0.3291E-07	0.9000E+00
180	0.657098E-02	0.431184E-01	0.447625E-01	0.000000E+00	0.3291E-07	0.9000E+00
190	0.707829E-02	0.432193E-01	0.350441E-01	0.000000E+00	0.3291E-07	0.9000E+00
200	0.758560E-02	0.431759E-01	0.324985E-01	0.000000E+00	0.3291E-07	0.9000E+00
210	0.809291E-02	0.432311E-01	0.279836E-01	0.000000E+00	0.3291E-07	0.9000E+00
220	0.860022E-02	0.432393E-01	0.215484E-01	0.000000E+00	0.3291E-07	0.9000E+00
230	0.910753E-02	0.432276E-01	0.199151E-01	0.000000E+00	0.3291E-07	0.9000E+00
240	0.961484E-02	0.432494E-01	0.157657E-01	0.000000E+00	0.3291E-07	0.9000E+00
250	0.101221E-01	0.432796E-01	0.135052E-01	0.000000E+00	0.3291E-07	0.9000E+00
260	0.106295E-01	0.432683E-01	0.125515E-01	0.000000E+00	0.3291E-07	0.9000E+00
270	0.111368E-01	0.432694E-01	0.105106E-01	0.000000E+00	0.3291E-07	0.9000E+00
280	0.116441E-01	0.432816E-01	0.841642E-02	0.000000E+00	0.3291E-07	0.9000E+00
290	0.121514E-01	0.432868E-01	0.658968E-02	0.000000E+00	0.3291E-07	0.9000E+00
300	0.126587E-01	0.432914E-01	0.559069E-02	0.000000E+00	0.3291E-07	0.9000E+00
310	0.131660E-01	0.433003E-01	0.471685E-02	0.000000E+00	0.3291E-07	0.9000E+00
320	0.136733E-01	0.433009E-01	0.382269E-02	0.000000E+00	0.3291E-07	0.9000E+00
330	0.141806E-01	0.433041E-01	0.322324E-02	0.000000E+00	0.3291E-07	0.9000E+00
340	0.146879E-01	0.433055E-01	0.292076E-02	0.000000E+00	0.3291E-07	0.9000E+00
350	0.151952E-01	0.433063E-01	0.247748E-02	0.000000E+00	0.3291E-07	0.9000E+00
360	0.157025E-01	0.433110E-01	0.222027E-02	0.000000E+00	0.3291E-07	0.9000E+00
370	0.162099E-01	0.433182E-01	0.180821E-02	0.000000E+00	0.3291E-07	0.9000E+00
380	0.167172E-01	0.433178E-01	0.160823E-02	0.000000E+00	0.3291E-07	0.9000E+00
390	0.172245E-01	0.433167E-01	0.123866E-02	0.000000E+00	0.3291E-07	0.9000E+00
400	0.177318E-01	0.433185E-01	0.111482E-02	0.000000E+00	0.3291E-07	0.9000E+00
410	0.182391E-01	0.433203E-01	0.967419E-03	0.000000E+00	0.3291E-07	0.9000E+00
420	0.187464E-01	0.433221E-01	0.921841E-03	0.000000E+00	0.3291E-07	0.9000E+00
430	0.192537E-01	0.433235E-01	0.750498E-03	0.000000E+00	0.3291E-07	0.9000E+00
440	0.197610E-01	0.433248E-01	0.661085E-03	0.000000E+00	0.3291E-07	0.9000E+00
450	0.202684E-01	0.433257E-01	0.574543E-03	0.000000E+00	0.3291E-07	0.9000E+00
460	0.207757E-01	0.433264E-01	0.505761E-03	0.000000E+00	0.3291E-07	0.9000E+00
470	0.212830E-01	0.433270E-01	0.449736E-03	0.000000E+00	0.3291E-07	0.9000E+00

ITER	T/Tc	Presidual	RESIDUAL	QRESID	DT	CFL
480	0.217903E-01	0.433274E-01	0.355484E-03	0.000000E+00	0.3291E-07	0.9000E+00
490	0.222976E-01	0.433278E-01	0.318034E-03	0.000000E+00	0.3291E-07	0.9000E+00
500	0.228049E-01	0.433283E-01	0.287888E-03	0.000000E+00	0.3291E-07	0.9000E+00
510	0.233122E-01	0.433286E-01	0.237023E-03	0.000000E+00	0.3291E-07	0.9000E+00
520	0.238195E-01	0.433288E-01	0.229638E-03	0.000000E+00	0.3291E-07	0.9000E+00
530	0.243269E-01	0.433290E-01	0.167264E-03	0.000000E+00	0.3291E-07	0.9000E+00
540	0.248342E-01	0.433292E-01	0.173549E-03	0.000000E+00	0.3291E-07	0.9000E+00
550	0.253415E-01	0.433293E-01	0.137788E-03	0.000000E+00	0.3291E-07	0.9000E+00
560	0.258488E-01	0.433294E-01	0.143502E-03	0.000000E+00	0.3291E-07	0.9000E+00
570	0.263561E-01	0.433296E-01	0.853066E-04	0.000000E+00	0.3291E-07	0.9000E+00
580	0.268634E-01	0.433296E-01	0.121294E-03	0.000000E+00	0.3291E-07	0.9000E+00
590	0.273707E-01	0.433297E-01	0.763257E-04	0.000000E+00	0.3291E-07	0.9000E+00
600	0.278781E-01	0.433298E-01	0.822120E-04	0.000000E+00	0.3291E-07	0.9000E+00
610	0.283854E-01	0.433298E-01	0.607511E-04	0.000000E+00	0.3291E-07	0.9000E+00
620	0.288927E-01	0.433299E-01	0.521945E-04	0.000000E+00	0.3291E-07	0.9000E+00
630	0.294000E-01	0.433299E-01	0.562938E-04	0.000000E+00	0.3291E-07	0.9000E+00
640	0.299073E-01	0.433299E-01	0.395881E-04	0.000000E+00	0.3291E-07	0.9000E+00
650	0.304146E-01	0.433299E-01	0.439624E-04	0.000000E+00	0.3291E-07	0.9000E+00
660	0.309219E-01	0.433300E-01	0.283659E-04	0.000000E+00	0.3291E-07	0.9000E+00
670	0.314293E-01	0.433300E-01	0.355063E-04	0.000000E+00	0.3291E-07	0.9000E+00
680	0.319366E-01	0.433300E-01	0.203483E-04	0.000000E+00	0.3291E-07	0.9000E+00
690	0.324439E-01	0.433300E-01	0.279576E-04	0.000000E+00	0.3291E-07	0.9000E+00
700	0.329512E-01	0.433300E-01	0.175444E-04	0.000000E+00	0.3291E-07	0.9000E+00
710	0.334585E-01	0.433300E-01	0.194111E-04	0.000000E+00	0.3291E-07	0.9000E+00
720	0.339658E-01	0.433300E-01	0.169975E-04	0.000000E+00	0.3291E-07	0.9000E+00
730	0.344731E-01	0.433300E-01	0.126403E-04	0.000000E+00	0.3291E-07	0.9000E+00
740	0.349805E-01	0.433300E-01	0.148617E-04	0.000000E+00	0.3291E-07	0.9000E+00
750	0.354878E-01	0.433300E-01	0.955440E-05	0.000000E+00	0.3291E-07	0.9000E+00
760	0.359951E-01	0.433300E-01	0.109872E-04	0.000000E+00	0.3291E-07	0.9000E+00
770	0.365024E-01	0.433301E-01	0.856819E-05	0.000000E+00	0.3291E-07	0.9000E+00
780	0.370097E-01	0.433301E-01	0.844754E-05	0.000000E+00	0.3291E-07	0.9000E+00
790	0.375170E-01	0.433301E-01	0.653365E-05	0.000000E+00	0.3291E-07	0.9000E+00
800	0.380243E-01	0.433301E-01	0.665461E-05	0.000000E+00	0.3291E-07	0.9000E+00
810	0.385317E-01	0.433301E-01	0.554451E-05	0.000000E+00	0.3291E-07	0.9000E+00
820	0.390390E-01	0.433301E-01	0.462920E-05	0.000000E+00	0.3291E-07	0.9000E+00
830	0.395463E-01	0.433301E-01	0.522365E-05	0.000000E+00	0.3291E-07	0.9000E+00
840	0.400536E-01	0.433301E-01	0.348037E-05	0.000000E+00	0.3291E-07	0.9000E+00
850	0.405609E-01	0.433301E-01	0.411088E-05	0.000000E+00	0.3291E-07	0.9000E+00
860	0.410682E-01	0.433301E-01	0.345474E-05	0.000000E+00	0.3291E-07	0.9000E+00
870	0.415755E-01	0.433301E-01	0.288192E-05	0.000000E+00	0.3291E-07	0.9000E+00
880	0.420829E-01	0.433301E-01	0.311056E-05	0.000000E+00	0.3291E-07	0.9000E+00
890	0.425902E-01	0.433301E-01	0.234940E-05	0.000000E+00	0.3291E-07	0.9000E+00
900	0.430975E-01	0.433301E-01	0.244763E-05	0.000000E+00	0.3291E-07	0.9000E+00
910	0.436048E-01	0.433301E-01	0.208467E-05	0.000000E+00	0.3291E-07	0.9000E+00
920	0.441121E-01	0.433301E-01	0.191467E-05	0.000000E+00	0.3291E-07	0.9000E+00
930	0.446194E-01	0.433301E-01	0.169042E-05	0.000000E+00	0.3291E-07	0.9000E+00
940	0.451267E-01	0.433301E-01	0.156017E-05	0.000000E+00	0.3291E-07	0.9000E+00
950	0.456341E-01	0.433301E-01	0.137462E-05	0.000000E+00	0.3291E-07	0.9000E+00
960	0.461414E-01	0.433301E-01	0.115708E-05	0.000000E+00	0.3291E-07	0.9000E+00
970	0.466487E-01	0.433301E-01	0.124497E-05	0.000000E+00	0.3291E-07	0.9000E+00
980	0.471560E-01	0.433301E-01	0.745061E-06	0.000000E+00	0.3291E-07	0.9000E+00
990	0.476633E-01	0.433301E-01	0.105214E-05	0.000000E+00	0.3291E-07	0.9000E+00
1000	0.481706E-01	0.433301E-01	0.609086E-06	0.000000E+00	0.3291E-07	0.9000E+00

Table C.5 contains the lift and drag histories for the on-design cases for each grid refinement evaluation.

Table C.5 Lift and Drag Histories

Baseline Investigation

(21 x 21 x 52)

ITER	Lift	Drag	L/D
100	-166.3704232514	20.85372228225	-7.977972517309
200	-162.3068898737	20.14124980963	-8.058431895129
300	-162.1416481401	20.07909078298	-8.075148914491
400	-162.1481040367	20.07413590913	-8.077463696108
500	-162.1487898099	20.07376718471	-8.077646229426
600	-162.1488370521	20.07375284872	-8.077654351636
700	-162.1488387425	20.07375225207	-8.077654675932
800	-162.1488387981	20.07375220915	-8.077654695977

Case 1r
(26 x 26 x 56)

ITER	Lift	Drag	L/D
100	-166.8766559794	20.93976522039	-7.969366142507
200	-163.5212164481	20.26532815257	-8.069013993603
300	-162.6999228369	20.12418160395	-8.084796988962
400	-162.623433449	20.104372658	-8.088958368184
500	-162.6048354742	20.10072642149	-8.089500452102
600	-162.6023474758	20.10030916731	-8.089544599654
700	-162.6021008537	20.10027156804	-8.089547462248

800	-162.6020880645	20.10026977768	-8.089547546522
900	-162.6020885772	20.10026986034	-8.089547538764

Case 2r
(31 x 31 x 62)

ITER	Lift	Drag	L/D
100	-168.270028032	21.11123819116	-7.97063755846
200	-163.8460240257	20.31969521364	-8.063409529671
300	-163.3672475182	20.17898094356	-8.095911680334
400	-163.2486495877	20.14249216645	-8.104689739419
500	-163.2632403926	20.13726415168	-8.107518437602
600	-163.2614095739	20.13583921604	-8.108001252008
700	-163.2615183507	20.13567526675	-8.10807267141
800	-163.2615315122	20.13564826215	-8.108084199055
900	-163.2615212665	20.13564250993	-8.108086006492
1000	-163.2615230378	20.13564235705	-8.108086156023

REPORT DOCUMENTATION PAGE

	December 1991	Master's Thesis

A COMPARATIVE STUDY OF NUMERICAL
VERSUS ANALYTICAL WAVERIDER SOLUTIONS

GREGORY OWEN STECKLEIN, Captain, USAF

Air Force Institute of Technology, WPAFB OH 45433-6583 AFIT/GAE/ENY/91D-26

Dr. Joseph Shang
WL/FIMM
Wright-Patterson AFB OH 45433

11. SUPPLEMENTARY NOTES

12a. DISTRIBUTION / AVAILABILITY STATEMENT

Approved for public release; distribution unlimited

The WL/FIMM explicit, Roe flux-splitting Euler algorithm is applied to the inviscid hypersonic flow over a parabolic-top waverider configuration, optimized for Mach 10 at zero degrees angle of attack. An on-design grid refinement study is conducted to determine the asymptotic nature of the optimized flight parameter L/D. A parametric study of off-design conditions is conducted to determine flow perturbation effects on HSDT waverider theory. A validation of the Euler code is conducted through comparison of the numerical data to analytical results derived by Rasmussen.

The grid refinement study shows little effect on the inviscid calculation of the optimized parameter L/D. Good agreement with HSDT waverider theory was attained for the on and off-design evaluations. Approximations involved in the numerical modeling of the waverider design produced large losses of lift as compared to the analytical results. Matching of the analytical results was possible only through a theoretical modeling process.

14. SUBJECT TERMS	15. NUMBER OF PAGES
Conical Bodies, Computational Fluid Dynamics, Hypersonic Aircraft, Inviscid Flow, Waveriders	129
	16. PRICE CODE

17. SECURITY CLASSIFICATION OF REPORT	18. SECURITY CLASSIFICATION OF THIS PAGE	19. SECURITY CLASSIFICATION OF ABSTRACT	20. LIMITATION OF ABSTRACT
Unclassified	Unclassified	Unclassified	UL

NSN 7540-01-280-5500